Summer 8-2022

Role of Structural Hierarchy in Multiscale Material Systems

Siavash Sattar
Old Dominion University, ssatt003@odu.edu

ROLE OF STRUCTURAL HIERARCHY IN MULTISCALE MATERIAL SYSTEMS

by

Siavash Sattar

A Thesis Submitted to the Faculty of
Old Dominion University in Partial Fulfillment of the
Requirements for the Degree of:

DOCTOR OF PHILOSOPHY

MECHANICAL ENGINEERING

OLD DOMINION UNIVERSITY
August 2022

Approved by:

Oleksandr G. Kravchenko (Director)

Miltos Kotinis (Member)

Gene Hou (Member)

Vukica Jovanovic (Member)

Diego Pedrazzoli (Member)

ABSTRACT

ROLE OF STRUCTURAL HIERARCHY IN MULTISCALE MATERIAL SYSTEMS

Siavash Sattar
Old Dominion University, 2022
Director: Dr. Oleksandr G. Kravchenko

Multiscale material systems derive their effective mechanical properties through a hierarchical organization of their structural elements and components. The hierarchy of a material is related to its effective properties, material processing, and composition. The hierarchy can be defined as an identifiable structural component with a specific size scale, such as the individual fibers collimated into platelets arranged randomly and producing a complex composite system or the lamellar structure in freeze-casted ceramic with the variation of in-plane orientation. In this study, the role of the structural hierarchy on the effective mechanical response and failure behavior of three complex material systems was studied, (i) long discontinuous glass fiber reinforced Nylon composite, (ii) prepreg platelet molded composite (PPMC), and (iii) freeze-casted porous alumina ceramic. Progressive failure analysis (PFA) was used to study the damage propagation up to ultimate failure. The developed computational models provided an understanding of how the material's morphology defines the variability of effective mechanical properties (modulus and strength) and the failure behavior.

To:

My father, Mohammadjavad

In loving memory

ACKNOWLEDGMENTS

I would like to thank my academic advisor, Dr. Oleksandr G. Kravchenko, for the opportunity to work on several research projects, for his guidance and support in all stages of my career at Old Dominion University, and for his vision and attitude that shaped my critical thinking and guided me to become a better researcher. I am thankful to my committee members, Dr. Gene Hou, Dr. Miltos Kotinis, Dr. Vukica Jovanovic, and Dr. Diego Pedrazzoli, for being on my panel, their support, and their helpful comments on my research. A special thanks to Dr. Sergey Kravchenko for the knowledge and expertise he shared with me, insightful discussions, and valuable comments on my work. My sincere thanks to our industrial partner, Johns Manville Co., specifically their R&D team that supported a part of the present research work. I wanted to thank all staff, colleagues, and friends, specifically in the Mechanical and Aerospace Engineering Department at Old Dominion University, that supported and helped me during my academic career. Finally, my deepest gratitude to my mother, Badry, and my brother, Siamak, for their constant support during my life and work.

TABLE OF CONTENTS

Page

Page

Page

Page

LIST OF TABLES

LIST OF FIGURES

Page

Page

Page

Page

Page

1 INTRODUCTION

Hierarchy, as a Greek word, means the rule of a high priest and describes the ranking of items-and organizational principles in nature. The word “hierarchy” was not related to the material system historically, but many materials system derives their functions using the hierarchy of the structural elements [1], [2]. Advanced material such as composites has a complex system with a network of components organized in a regular or random orientation, permitting the development of emergent behavior at macroscopic scales. The material properties depend on the material structure, which in turn depends on the manufacturing process. Material scientists are looking to understand how the processing history of the material affects the structure and, as a result, the material response. Understanding the manufacturing structure-property relationship is essential to predict the effective mechanical response and failure behavior of the material. The constituent material elements, their orientation, the interaction between different structural levels, and the processing history are the major determinants of the material structure and its effective properties. A structural level can be defined as the identifiable structural components with a specific size scale. e.g., the platelets constituted of the collimated fibers can be stacked in a regular or stochastic orientation and form long discontinuous fiber reinforced composites (LDFCs) [3]. Freeze-casted ceramic contains highly aligned lamellar walls with varying in-plane orientations[4], [5]. In this chapter, two types of multiscale material systems are introduced: (i) LDFCs and (ii) freeze-casted porous ceramic. The processing of the material and the internal structure on micro and mesoscale were presented. Finally, the scope of the work on understanding the processing structure-property relationships of the considered materials is explained.

1.1 Long discontinuous fiber reinforced composites

Discontinuous fiber reinforced composites are becoming common among the aerospace and automotive industry, particularly for complex geometries, produced by compression molding, due to improved formability of the material [6]. High production rates with low cost are significant advantages of short and long discontinuous fiber reinforced composites when compared with continuous fiber composites. The mechanical properties of discontinuous fiber composites strongly depend on the material mesostructure such as fiber length, arrangement and orientation [7]. Short discontinuous fiber composites typically do not provide sufficient reinforcement for structural applications. The use of short fiber systems (fiber length below 100-200 μm) results in relatively low level of stiffness and strength in composites due to the limited fiber-volume fraction, in the range of 10–30%, and flow induced anisotropic properties [8]. Therefore, long fiber thermoset and thermoplastic composites (fiber length in the range of 5-30 mm) can be used to provide the required mechanical properties for structural applications, while allowing for increased formability. Compression molding is a high-volume manufacturing process, suitable for long discontinuous fibers dispersed in a matrix. The matrix can be either a thermoset or thermoplastic resin in the form of prepreg platelet molding compound (PPMC), sheet molding compound (SMC) or bulk molding compound (BMC) [9]. The present study considered two LDFC materials: (i) a novel long discontinuous glass fiber reinforced nylon composite called organosheet (ii) Prepreg platelet molding compound (PPMC). The organosheet was produced in a continuous process through the impregnation of glass fiber reinforcement consisting of 1” long fibers with low viscosity caprolactam monomer, followed by the in situ anionic polymerization of caprolactam to form the thermoplastic PA-6 matrix [10]. The organosheet can allow pseudo-random 2D or preferred orientation of long discontinuous fibers, while preserving a uniform fiber length (1”). This material system and manufacturing process allow for high fiber loading providing structural

grade mechanical properties, while offering ease of production of complex geometries [10]. The low viscosity of caprolactam leads to a thorough resin impregnation of long discontinuous fibers bundles. This manufacturing process produces high fiber loading with weight fraction higher than 50% and low void content. The in-situ polymerization results in a high molecular weight of PA6 matrix which allows for good mechanical properties. The meso-scale morphology of the glass fiber is preserved during the impregnation process resulting in regions with high fiber collimation, and PA6 pockets surrounding them. As a result, the formation of bundles during the manufacturing stage produces a complex morphological arrangement in the meso- and micro-structure of the material. The resulting organosheet composites with the thickness of 1.5mm (Figure 1-a) were viewed as a system, consisting of bundles, which are represented by impregnated fibers with high fiber volume fraction, and PA6 matrix pockets (Figure 1-c). Neat PA6 polymer processed by anionic polymerization of caprolactam was used for mechanical characterization to determine the matrix constituent properties in the organosheet.

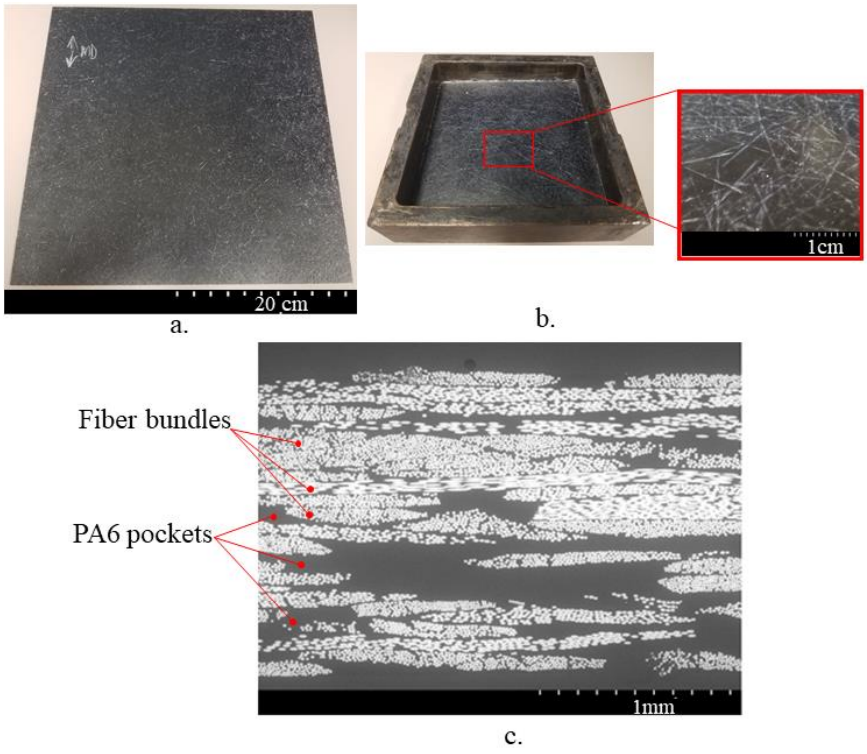

Figure 1 Organosheet before (a) and after (b) compression molding process; cross-section micrograph of an organosheet

PPMC is a material system processed by compression molding of unidirectional prepreg platelets to achieve a discontinuous composite system with a heterogeneous mesoscale morphology, controlled fiber length, and 50–60% fiber volume fraction (FVF) [11]–[13]. PPMC are fabricated by cutting the prepreg into platelets with a prescribed length then compression molding the platelets into a required geometry (Figure 2) [8]. The collimated fibers of the same length within a platelet and the compression molding of the platelets results in enhanced mechanical properties and sufficient formability of PPMCs compared to the composites processed with sheet molding compound (SMC) or bulk molding compound (BMC) with 10-30% FVF [14], [15]. PPMCs are suitable for the automotive industry due to its high manufacturability in terms of production rates and molding of components with complex geometry, which along with the

structural grade mechanical properties meet the design requirements [11]. In hierarchical composite systems, the internal structure can be presented on different scales, where the larger structural length scale of the material defines the effective mechanical response [17], [18]. PPMC as a hierarchical composite system can be presented in two levels of length scale: (i) a micro-scale where individual fibers are distinguishable in a platelet, and (ii) a meso-scale, which includes the stochastic platelets distribution [19]. The stress transfer between the interacting platelets at the mesoscale defines the mechanical response of PPMCs. The interactions between platelets determine the progressive damage and macroscopic properties of PPMC components. The mesoscale morphology of PPMCs is characterized by the dimension of platelets, platelet orientation and overlapping between the platelets, all of which are affected by the number of platelets within the component [13]. The orientation state of PPMC describes how the platelets are oriented and is an important morphology descriptor in the PPMC mechanical variability [20]. The orientation distribution of the platelets can be stochastic with irregular or deterministic with regular arrangement [19]. A stochastic distribution of PPMC is achieved when the orientation of the platelets results from the uncontrolled arrangement of PPMC in the mold.

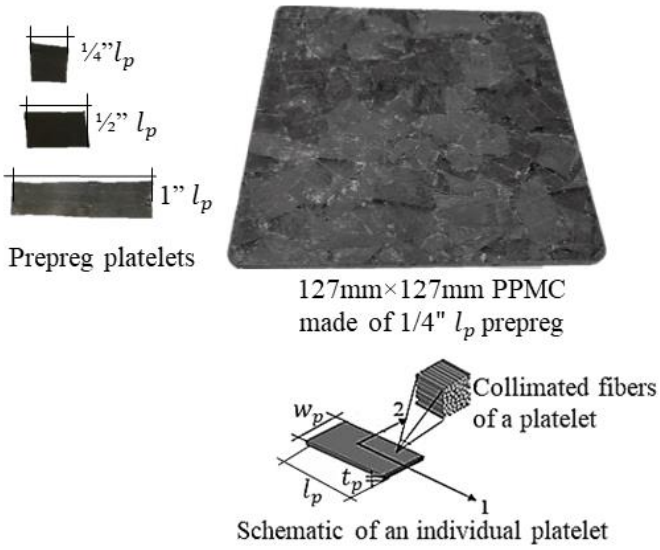

Figure 2 Prepreg platelet molded composite (PPMC) system

The morphology of the organosheet resembles the platelets in PPMC material systems, however, the organosheet morphology presents significant differences. The bundles are separated by the PA6 rich pockets, which are formed throughout the in-situ polymerization process. The effective mechanical properties of organosheet composite systems depend on the material hierarchical mesostructure, which depends on the local properties of each constituent phase and its volume fraction, and the corresponding fiber orientation [21]. The organosheet similar to the PPMC composite presents two levels of hierarchical structural length scale: (*i*) the micro-scale, which is defined by the individual fibers dispersed in the polymeric matrix, and (*ii*) the meso-scale, which includes bundles with defined global orientation distribution.

Understanding the internal structure-property relationships in LDFCs requires connecting the fiber volume fraction, geometry of the bundle/platelet and its orientation with the effective mechanical properties under various loading conditions [22]. The local fiber arrangement and its orientation vary throughout the volume of LDFCs, as a result LDFCs typically show a mixed

failure mode including the fiber splitting, matrix failure, debonding, and shear crippling [20], [23]. The aspect of the damage propagation, the failure mode, depends on the constituent mechanical properties, fiber length and its distribution. Damage in the LDFC occurs where local meso-scale stress concentrations yield the possible failure sites. Therefore, the local structural orientations and dimensions of fibers have a major role in the failure mechanisms[24]. Various authors studied the effect of the sample size and the platelet geometry on the failure mode in tension in PPMCs [3], [25]. The failure mechanism in PPMCs depends on: (*i*) the platelet effective properties, including platelet-to-platelet interfacial properties, (*ii*) ratio between platelet length to its thickness, defined as aspect ratio, (*iii*) platelets orientation distribution, and (*iv*) overlap lengths of platelets. Higher platelet ratio promotes fiber failure and results in increased mechanical properties [3], [26], [27].

The mechanical behavior of organosheet, similarly to PPMC, is determined by the bundle aspect ratio, effective properties of the bundles, and surrounding PA6 pockets. The PA6 matrix of organosheet is distinctively ductile material compared to brittle epoxy based and some engineering thermoplastics in PPMC. The ductile behavior of the matrix phase in the bundle and the surrounding matrix pockets underscore the need for the additional analysis into the role of PA6 mechanical behavior on the resulting properties of organosheet. The dominant failure mode in organosheet was found to be failure in PA6 pockets, which behave as a ductile material owing to the large plasticity in the semi-crystalline nylon [22], [28]. Therefore, the mesostructure of organosheet with the bundle geometry surrounded by PA6 pockets governs the stress transfer and failure mechanism within the material.

Computational analysis of the structure-property relationship in LDFCs allows one to virtually study the control parameters in the mesoscale and address the effects of material variables on the effective properties and failure behavior [29]. Selezneva et al. [30] developed a model to

predict strength of PPMCs considering local mesostructure effects, strand failure and disbonding. Feraboli et al. [31] proposed a stochastic laminate analogy for the discontinuous carbon/epoxy composite based on the experimental observation and Classical Laminated Plate Theory (CLPT), to account for modulus variability. An evident limitation of that modeling is that it cannot account for the 3D stress transfer between the platelets and was not capable to capture platelet length or thickness effects on the strength. Harper et al. [32] developed a PPMC model of using an embedded element approach with explicitly modeled platelets, wherein the complex mesoscale features such as orientation distributions and platelet overlap were incorporated into a computational model. Kravchenko et al. [33] performed a parametric FEA analysis for randomly oriented PPMC to study the effect of the orientation and the aspect ratio of the platelets on the effective tensile stiffness and strength by employing a Continuum damage mechanics (CDM) and a cohesive interfacial behavior to simulate the propagation of the damage in platelets. The results showed the high dependency of the effective mechanical properties and failure mechanism on the platelet aspect ratio and orientation distribution of platelets.

1.2 Freeze-casted alumina ceramic

Freeze-casted cellular materials are lightweight, exhibit high heat resistance and strength as a result of their anisotropic morphology stemming from the manufacturing process [4]. Ice-templated ceramic typically contains highly aligned lamellar walls with varying in-plane orientations (Figure 3). Therefore, ice-templated materials can be potentially used in ceramic filters, insulations, as well as in bone scaffolds and tooth fillers. [4], [5]. The freeze-casting is a net-shape, versatile processing technique that is used to produce porous ceramics and can be applied to various material systems [34], [35]. Freeze-casting consists of three general steps: freezing a liquid suspension followed by the sublimation and sintering to densify the ice-templated

scaffolds [36]. The density and porosity of the processed material depends on the powder loading, composition and stability of the slurry [34]. Ice-templating process allows, to a great extent, control the morphology to control the processing steps and, as a result, produce engineering material with targeted moduli and strength. In the last decade multiple researchers studied the mechanical properties of templated ceramics. Deville [37] evaluated the effect of particle size on the solidification behavior of the suspension during the directional freezing by X-ray radiography and tomography experiments. The results indicate that the smaller particle sizes show more nucleation of ice crystals with larger surface area during freeze casting. Furthermore, nucleation and growth of ice crystals can be processed at a higher temperature for smaller particles. Ghosh et al. [38] processed ice-templated alumina scaffolds with different particle sizes and evaluated the effects of the particle size on the properties of the alumina scaffolds with respect to the solids loading and freezing front velocity. Deville et al. [36] investigated the effect of freezing rate of ceramic slurry, sublimation and sintering condition in processing ice-templated material on the structural properties of the material. In their study, the control of the lamellar wall distribution was obtained through the freezing rate of the ceramic slurry. Weaver et al. [39] applied two different freezing rates, using water-based polymer solutions and various volume fractions of solid loading to study structure-processing correlations in freeze-cast metal-based scaffolds. Sajgalik [40] processed Si_3N_4 sintered ceramics, containing Y_2O_3 and Al_2O_3 as sintering additive, to study the effect of the Si_3N_4 grains size with the same amount and ratio of additives on the microstructure of the material and the fracture toughness. The results showed that fracture toughness and microstructure was governed by the volume fraction of β-Si_3N_4 grains and higher volume fraction displayed the higher fracture toughness. The existing experimental and material characterization knowledgebase

for processing ice-templated ceramic provides insight on how the solids loading, the composition of slurry, and freezing condition affect the porous microstructure and porosity.

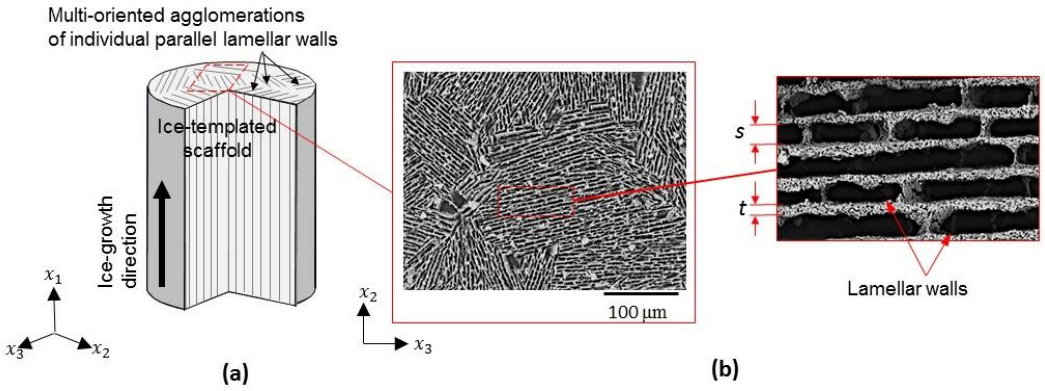

Figure 3 (a) Schematic of ice-template ceramic foam, showing principal composite directions (b) Micrographs showing agglomerations of parallel lamellar walls; s and t represent wall thickness and wall spacing, respectively

The mechanical properties of freeze-casted material are governed by their porous anisotropic micro-structure. However, currently the understanding of the fundamental mechanics describing the microstructure-property relationships is missing in the field. Andrews et al. [41] explained the general deformation mechanics of the cellular solids using dominant deformation mode of the structural elements comprising the cellular solid, e.g. uniaxial deformation or bending of the cellular struts. Furthermore, Gibson et al. [42] developed analytical models to describe the failure modes for cellular solids under multiaxial loads by considering the plastic deformation and brittle fracture of cellular material. More recently, Seuba et al. [43] suggested that the compressive behavior of ice-templated material is better described by the honeycomb analytical model proposed by Gibson et al. and Ashby et al. [42], [44], in comparison with the open cell and close cell models. Other research groups pointed out this similarity in the microstructure of the ice-

templated foams and honeycomb structures[45], [46]. Such an analogy is based on the microstructure of ice-templated materials that exhibit variation of lamellar wall in-plane orientation, which is typical to honeycomb structure.

Novel fabrication methods for processing porous templated ceramics with controlled microstructural orientation have been proposed in recent years. Nelson et al. [47] fabricated porous Fe_3O_4 scaffolds by a freeze casting: the fabricated porous scaffolds aligned uniformly under the magnetic field direction. Ferrand et al. [48] presented a method to fabricate the dense alumina ceramic with the deliberate periodic grain orientation by combining magnetic stirring assisted slip casting (MASC) and templated grain growth (TGG). They processed alumina ceramics with highly aligned grains by TGG and to control the orientation of the anisotropic local particles by MASC. Minas et al. [49] combined 3D-printing, the direct ink writing method, and particle-stabilized foam templating to process alumina scaffold with homogeneous porous structure. Overall, the microstructure of ice-templated foams has a significant effect on the resulting mechanical properties. Zhang et al. [50] extracted the 3-D structure and the composition of the cordierite–mullite–alumina ceramic foam by conducting X-ray CT scan and SEM, which informed finite-element modeling and found that the induced damages in ceramic foam with fewer cells generate more quickly once the stress exceeded the flexural strength compared with a foam with more cells and similar relative density. Seuba et al. [51] used Weibull analysis to measure the mechanical behavior of ice-templated material under compression. Depending on the pore volume fraction they observed catastrophic or progressive brittle failure. Furthermore, their results show high dependency of the type of failure on lamellar wall thickness.

However, in order to establish a quantitative model to explicitly describe the processing-structure-property relationships in ice-templated cellular solids requires the computational micro-

mechanical models that can incorporate complex morphology observed, while providing a valuable tool for understanding the general trends in processing-structure-property relationships. Lamellar ceramic walls have micron size thickness, resulting in significantly different mechanical properties than bulk ceramic. Feilden et al. [51] applied the micro 3-point bending test to measure the flexural strength and elastic modulus of microscopic alumina platelets. The 3-point bending load-displacement response measured by Fielden et al. was used to calculate stiffness of a single lamellar wall and was used for developing the present micromechanical model. Another important morphological attribute of the anisotropic ice-templated foams is the misalignment of the lamellar walls that develops during the ice crystal growth [36], [52]–[54]. Furthermore, the loading conditions applied to ice-templated foams or composites are not expected to coincide with the unidirectional lamellar structure, therefore, it is important to characterize the off-axis compressive behavior of these materials. Different research groups investigated the effect of off-axis loading in various composite materials [55], however, a few studies exist for the freeze-casted ceramics [56].

1.3 Scope of work

This dissertation focuses on computational models that quantify the structure-property relationships in three hierarchical material systems:

1. A novel long discontinuous glass fiber nylon composite (organosheet)
2. Prepreg platelet molded composites
3. Freeze-casted alumina ceramic

The statistical microscopy characterization and the material's micro and meso-orientation were used to establish the computational model. The heterogeneity of the hierarchical material system affects the complex path of damage propagation and the material's mechanical properties. The progressive failure analysis (PFA) was used to simulate the damage behavior and how the

material morphology affected the failure modes. This dissertation is implemented to study the effect of morphological features on the mechanical response of the hierarchical materials under static loading.

1.3.1 Analysis of processing structure-property relationships in organosheet

A computational model was developed to simulate and explain the variability of the effective tensile and flexural properties (modulus and strength) in LDFC made of 1” glass fiber reinforced PA6, processed by in-situ polymerization. The statistical microscopy characterization of fiber and bundle orientation distribution within the organosheet was presented and used for establishing computational model. A sequential adsorption probabilistic approach was used to generate the complex geometrical arrangement and distribution of the bundles within the PA6 pockets [57]. A continuum damage mechanism was used for simulating the orthotropic bundle damage behavior, while PA6 pockets were modeled as an isotropic material with elastoplastic behavior and the ductile damage mechanism. The analysis of the degree of crystallinity, using differential scanning calorimetry (DSC), was used on organosheet and neat PA6 to ensure correspondence between the tested neat PA6 and PA6 phase in organosheet. Standard tensile test was conducted on the pure PA6 to measure the mechanical properties, which were then used in progressive failure analysis (PFA) simulation of organosheet. The tensile and flexural properties of long fiber thermoplastic organosheet were tested to validate the simulations and analyze the size effect on the flexural mechanical responses. The failure behavior was explained through the combination of the different failure modes based on the span length effect under flexural loading and the effect of bundle orientation in both flexural and tensile loading conditions.

The effect of geometric discontinuity in open hole tension (OHT) for LDFC has been shown to be on the same order as the length scale of internal mesostructure [54]. Therefore, OHT

LDFC coupons may fail either in the vicinity or away from the notches depending on the dominant stress concentrations, which can reside either in the local morphology or in the geometrical discontinuity. To simulate the variability of the OHT strength and failure behavior in LDFC made of 25.4mm (1") glass fiber reinforced organosheet a computational model was presented. The computational framework was used to study the notch sensitivity and stochastic variation in OHT strength. The modeling results were validated with experimental OHT testing. The point stress criterion (PSC) and modified point stress criterion (MPSC) analytical models were calibrated through the simulation and experimental results to predict the notch sensitivity of the organosheet and showed close correlation with each other.

The mesostructure of the organosheet develops during processing when the orientation and arrangement of bundles result from the anisotropic flow of the molding compound. The orientation distribution of bundles has a crucial role in affecting the mechanical properties. The orientation state depends on the processing conditions, such as flow arising during the molding. To study the effect of the molding process condition on the mechanical properties, the full and partial mold coverage was compression molded. Tensile specimens were cut from both full and partial coverage molded panels in the flow direction and tested to compare the effective properties of the composite.

1.3.2 Analysis of structure-property relationships in PPMCs

Increasing platelet aspect ratio in PPMC under uniform tensile loading is known to result in changes in failure mode: from platelet debonding to fiber failure, resulting in an increase of both modulus and strength [3]. The main objective of this work was to simulate and explain the variability of effective flexural modulus and strength of a stochastic PPMC and study the effect of the prepreg platelet length on flexural mechanical properties and failure modes. The PFA of PPMC included the continuum damage mechanism, and a cohesive interfacial behavior was used to

simulate and explain the variability of effective flexural modulus and strength of a stochastic PPMC and study the effect of the prepreg platelet length on flexural mechanical properties and failure modes. To study the effect of the platelet length and the number of platelets (platelet count) on the flexural behavior of PPMC, various platelet lengths, namely ¼", ½" and 1" of the prepreg, were considered with the sample thickness of 2.5mm. Experimental studies showed competing contributions of the platelet aspect ratio and platelet count on the mechanical flexural behavior. PFA of virtual PPMC samples allowed to study the changes in the failure modes interactions under flexural loading and determine the dominant failure modes, including platelet debonding and transverse matrix failure. To study the non-uniformity in platelet local orientation, two modeling approaches to generate the stochastic PPMC morphology in the virtual samples based on the assigned global fiber orientation distribution (FOD) were used, namely, (i) generating individual coupons and (ii) generating a virtual plaque that was then used to create various coupons. The proposed methodology for PFA is supported by the experimental observations and can be used to investigate the structure-property relationship in PPMCs.

1.3.3 Multiscale modeling of freeze-casted ceramic from micromechanical to homogenization

The computational modeling of the compressive behavior in freeze-casted ceramic was studied to predict the effective structural properties of ice-templated ceramic under off-axis loading. The microstructural modeling of the freeze-casted ceramic was developed using two methods: (i) A novel representative volume element (RVE) model was developed based on the microstructure of ice-templated materials (ii) A macroscale computational model was developed using the homogenized approach. The proposed RVE model incorporates a smaller number of required input parameters and allows for trade-off material analysis and parametric studies of how material properties and local microstructure affects mechanical behavior. Honeycomb structural

analogy was used in formulation of the computational micro-mechanical RVE model due to the similar morphology exhibited in ice-templated porous ceramic. A periodic geometry with idealized lamellar wall orientation was proposed for the RVE model. The periodic boundary conditions were applied to RVE to model bulk mechanical behavior. The smeared cracking model was used to determine the material's stiffness and compressive strength response. Micromechanical analysis of RVE was used to predict all material constants and as the input parameter of homogenized modeling. In the second method (homogenized modeling on the macroscale), the transversely isotropic stress-stress relationship is used based on the material planes of symmetry. A normal distribution defines a spatially varying field over elements calculated through the measured distribution of the material's local orientation of the lamellar structure. To evaluate the progressive damage of the material, continuum damage mechanics were used for the model with two damage variables: (i) in the direction of the lamellar structure and (ii) transverse direction to the lamellar structure.

Furthermore, off-axis compression testing of ice-templated alumina was done to obtain the effective properties of the material using digital image correlation (DIC). The effective misalignment angle is quantified by DIC and used for better correlation with the modeling prediction. The RVE analysis was proposed as a micromechanical framework to determine the effective properties of ice-templated ceramic, which can be modeled with the orthotropic homogenized constitutive model. The results show that proposed computational micromechanics-based tool can predict the experimentally measured behavior of the ice-templated alumina under off-axis compression. However, local effects such as the distribution of local orientation in lamellar structure should be reflected in the homogenized model. The proposed RVE is effective for homogenization purposes to determine effective properties for structural analysis. The

combination of microscale RVE and macroscale homogenized modeling allows parametric studies to determine morphological parameters' role in compressive behavior.

2 COMPUTATIONAL MODELING

A complex mesostructure of hierarchical material provides an internal redundancy resulting in the redistribution of the load path to undamaged regions and damage progression with alternative paths during loading [58]. The degradation of the properties in the hierarchical material system is attributed to the alternative damage progression paths during loading. The heterogeneous material system typically shows the local damage before reaching the ultimate failure in which the material system cannot support the increase in stress components. PFA is a tool to study the failure behavior of a complex material that works based on computational damage mechanics. The local damage in PFA does not have to be correlated with ultimate failure. Therefore, the degradation of material properties is the primary concern in computational damage modeling. The stress-strain relationships can be established through the constitutive model that should represent the mechanical behavior of the material [59]. There are several approaches deriving the constitutive model of a complex material system, such as micromechanics, homogenization, and multiscale modeling. This chapter describes the computational modeling of three considered hierarchal material systems to predict the variability of the material properties and the failure behavior.

2.1 Modeling procedure for progressive failure analysis of organosheet

Computational mesoscale models of LDFCs allow characterizing the mechanical response of the material and the failure behavior in relation to the structural properties. This section describes the computational modeling of stochastic mesostructure of organosheet coupon using the continuum damage mechanics to predict the variability of tensile and flexural modulus and strength of the organosheet as well as the failure modes.

2.1.1 Mesostructure generation for organosheet virtual specimen

The mesostructure of the model including bundles with transversely isotropic elastic behavior and isotropic matrix pockets was generated using Digimat-FE (e-Xstream Engineering). The bundles were generated and oriented sequentially, requiring bundle volume fraction, dimensions, global orientation, and the specimen sizes as inputs (bundle orientation is defined by the bundle fiber direction). Then, the matrix pockets within the voxel mesh were generated in between the dispersed bundles in the requested volume of the morphology. The bundle volume fraction in the model was measured through a microscopy analysis discussed in Section 3-2. A virtual specimen of organosheet is modeled as a continuum in (x_1, x_2, x_3) space with sub-domains assigned local coordinate systems (1,2,3) to represent individual bundles, which creates the defined boundaries and local stiffness discontinuities between bundles that control the local mesoscale composite mechanics. The numerical reconstruction of stochastic features of organosheet mesostructure is implemented via the sequential adsorption algorithm and is based on sampling from the probability space, which is achieved by considering the uncertainty in bundles locations and orientations. The stochastic structural arrangement and orientation of individual bundles are approximated by generating their center points and bundle direction angles according to the uniform probability distribution function. Figure 4-a shows the generated organosheet, where the white and black region represents the distribution of bundle and matrix pockets, respectively. Bundles are created on a voxel mesh by grouping voxels into bundle-shaped sets and prescribing the local material coordinate systems to these sets. The orientation state and overlapping of a few bundles are shown in Figure 4-b and the subdomains occupied by individual bundles are shown in different colors. The corresponding local material coordinate systems for two overlapping bundles are shown in Figure 4-b as $(1_k, 2_k)$ and $(1_m, 2_m)$ where 1 and 2 directions

are the local bundle fiber direction and transverse direction, respectively. The bundles are built up in the x_3-direction for a globally uniform planar orientation state, so the bundle normal vector (3-direction) is oriented along the global x_3-axis. The oriented individual bundles developed local stiffness discontinuities within the organosheet. The bundles were oriented according to the global orientation distribution function (ODF) [60]. The bundle width and thickness in the model were measured through the ellipse-fitting on the bundle cross-section within the micrograph of the organosheet (section 3.2). The resulting voxelized morphology of the organosheet generated by Digimat FE is imported into ABAQUS/Standard (Implicit), where each voxel becomes an eight-node brick C3D8 finite element, and material model and loading conditions are applied. Figure 4-c represents a schematic for the idealized stress components on a voxel. The voxel element in-plane dimensions were 1×0.5 mm and thickness of 0.04 mm. The length, width, and thickness of the generated organosheet sample was $80 \times 25 \times 2.4\ mm$ for three-point bending. The tensile modeling was performed in a periodic RVE which allows for simulation of the bulk material behavior using periodic displacement boundary conditions to conduct progressive failure, non-linear analysis due to local material softening. Figure 4-d and 5e show the configuration of the three-point bending model for the span of 70mm and the RVE tensile test, respectively, and $60 \times 25 \times 1\ mm$ for tensile modeling with the total element number of 75000 for tensile and 240000 for three-point bending simulations. Based on the constructed organosheet, a three-point bending test was implemented in ABAQUS with different span lengths of 30, 50, and 70mm.

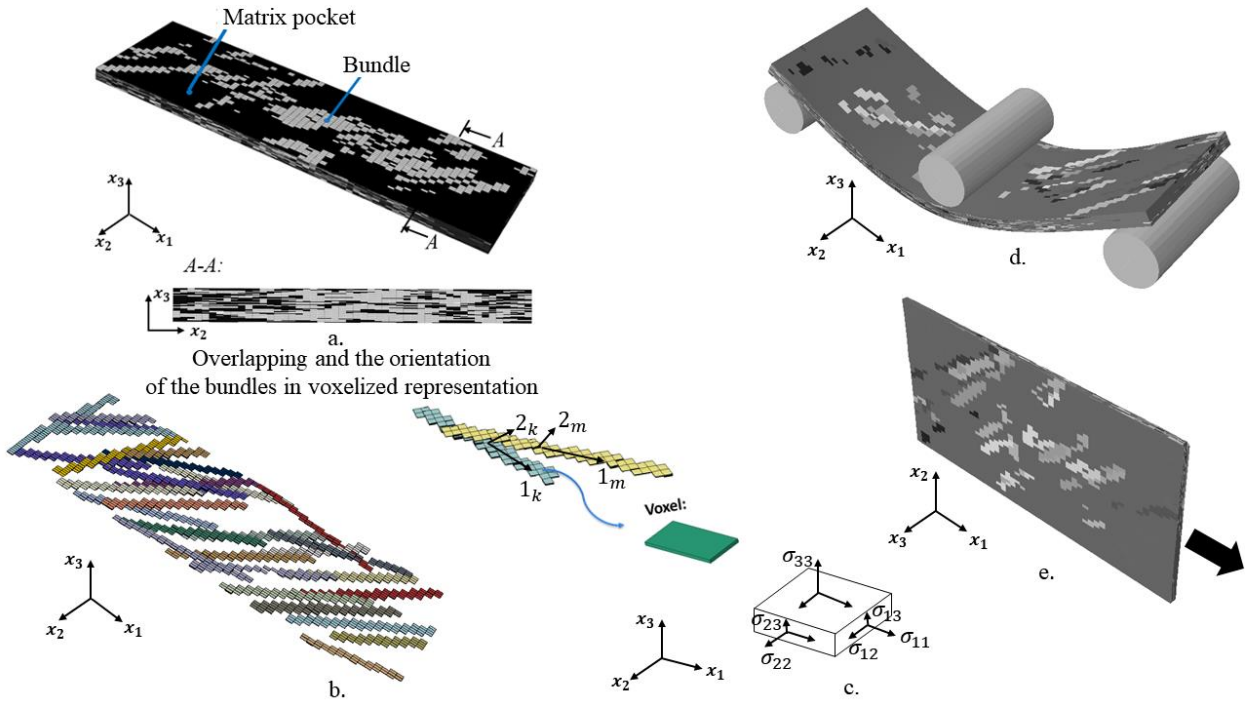

Figure 4 (a) Generated organosheet morphology (b) Overlapping and orientation a few bundles in voxelized representation (c) Stress components on a voxel (d) Deformed state for 3-point bending analysis (e) RVE of organosheet for tensile virtual testing

To develop the OHT morphology, a finite element mesh representing a domain with a circular center notch with a prescribed radius was generated (Figure 5). Three sizes of the radius, 1mm, 2mm, and 3 mm, were considered for the finite element model of virtual OH organosheet coupons, and three coupons were generated for each size of the circular hole to predict the variability of the strength within the organosheet. Based on the constructed organosheet, a tensile test was implemented in ABAQUS/Standard (Implicit) with an eight-node solid brick C3D8 finite element. The length, width, and thickness of the generated sample was 127×25×2.4 mm. The tensile modeling was performed in a full-size coupon with progressive failure scheme.

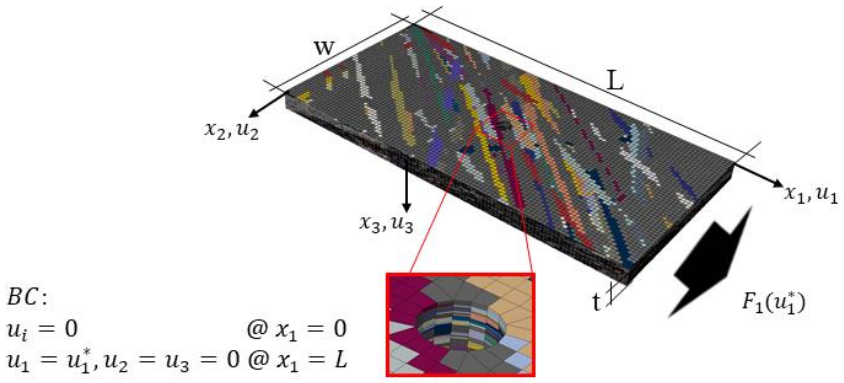

Figure 5 Generated organosheet morphology with 2mm hole diameter

2.1.2 Constitutive behavior and damage model for PA6 –glass fiber bundles

The individual bundles a in meso-scaled computational model considered as a transversely isotropic homogenized material. The homogenized constitutive stiffness properties of the bundle were calculated by analytical micromechanics using a self-consistent field model based on the average fiber volume fraction in the bundles and the parent E-glass and pure PA6 material properties [58]. Anisotropic strengths of bundles in principal directions were calculated using an analytical micromechanical bridging model developed by Huang [59] [35], [36. The nonlinear response of composite is caused by plastic deformation of the matrix material. The bridging model takes into account the effect of matrix plasticity on the failure mode of composites and is used to predict the inelastic and failure behavior of polymer composite materials [61]. In this method, strengths of the fibrous composites are calculated based on the constituent properties and fiber volume fraction. The fibers are supposed to be elastic until rupture and the matrix is assumed as a bilinear elastic–plastic material. The principal strength of the PA6/glass fiber bundles were calculated based on the relationships included in Appendix A following [62], [63].

A user material (UMAT) FORTRAN subroutine [13] for Abaqus standard implicit was employed to simulate the damage initiation and propagation in fiber direction, transverse to the fiber direction and in the through thickness direction. The bundle in-plane damage implies the stiffness degradation in the orthotropic homogenized material due to the in-plane stresses. Out of plane damage index shows the degradation of the material stiffness through the thickness direction and attributed to the delamination damage that develops between the individual bundles. The bundles assumed as an orthotropic homogenized material following constitutive relationship in (Equation 1).

$$\begin{Bmatrix} \boldsymbol{\sigma_{11}} \\ \boldsymbol{\sigma_{22}} \\ \boldsymbol{\sigma_{33}} \\ \boldsymbol{\sigma_{12}} \\ \boldsymbol{\sigma_{13}} \\ \boldsymbol{\sigma_{23}} \end{Bmatrix} = \begin{bmatrix} \boldsymbol{C_{11}} & \boldsymbol{C_{12}} & \boldsymbol{C_{13}} & \boldsymbol{0} & \boldsymbol{0} & \boldsymbol{0} \\ \boldsymbol{C_{12}} & \boldsymbol{C_{22}} & \boldsymbol{C_{23}} & \boldsymbol{0} & \boldsymbol{0} & \boldsymbol{0} \\ \boldsymbol{C_{13}} & \boldsymbol{C_{23}} & \boldsymbol{C_{33}} & \boldsymbol{0} & \boldsymbol{0} & \boldsymbol{0} \\ \boldsymbol{0} & \boldsymbol{0} & \boldsymbol{0} & \boldsymbol{C_{44}} & \boldsymbol{0} & \boldsymbol{0} \\ \boldsymbol{0} & \boldsymbol{0} & \boldsymbol{0} & \boldsymbol{0} & \boldsymbol{C_{55}} & \boldsymbol{0} \\ \boldsymbol{0} & \boldsymbol{0} & \boldsymbol{0} & \boldsymbol{0} & \boldsymbol{0} & \boldsymbol{C_{66}} \end{bmatrix} \times \begin{Bmatrix} \boldsymbol{\varepsilon_{11}} \\ \boldsymbol{\varepsilon_{22}} \\ \boldsymbol{\varepsilon_{33}} \\ \boldsymbol{\gamma_{12}} \\ \boldsymbol{\gamma_{13}} \\ \boldsymbol{\gamma_{23}} \end{Bmatrix} \quad \text{(Equation 1)}$$

C_{ij} is the damaged stiffness matrix depending on the undamaged stiffness components (C_{ij}^{0}) and damage variables in principle directions (d_{i}). The damage stiffness components were defined by (Equation 2).

$$\boldsymbol{C_{11} = (1 - d_1)C_{11}^{0}}\,,\ \boldsymbol{C_{12} = (1 - d_1)(1 - d_2)C_{12}^{0}}\,,\ \boldsymbol{C_{13} = (1 - d_1)C_{13}^{0}}\,, \quad \text{(Equation 2)}$$

$$\boldsymbol{C_{22} = (1 - d_2)C_{22}^{0}}\,,\ \boldsymbol{C_{23} = (1 - d_2)(1 - d_3)C_{23}^{0}}\,,\ \boldsymbol{C_{33} = (1 - d_3)C_{33}^{0}}\,,$$

$$\boldsymbol{C_{44} = (1 - d_1)(1 - d_2)C_{44}^{0}}\,,\ \boldsymbol{C_{55} = (1 - d_3)C_{55}^{0}}\,,\ \boldsymbol{C_{66} = (1 - d_3)C_{66}^{0}}$$

(Equation 3-5) show the damage initiation criteria to predict the failure initiation, when the corresponding criterion reaches one.

$$\boldsymbol{f_1} = \sqrt{\frac{\boldsymbol{\varepsilon_{11}^2}}{\boldsymbol{\varepsilon_{11}^{f,t}\varepsilon_{11}^{f,c}}} + \boldsymbol{\varepsilon_{11}} \times \left(\frac{\boldsymbol{1}}{\boldsymbol{\varepsilon_{11}^{f,t}}} - \frac{\boldsymbol{1}}{\boldsymbol{\varepsilon_{11}^{f,c}}}\right)} \quad \text{(Equation 3)}$$

$$\boldsymbol{f_2 = \sqrt{\frac{\varepsilon_{22}^2}{\varepsilon_{22}^{f,t}\varepsilon_{22}^{f,c}} + \varepsilon_{22} \times \left(\frac{1}{\varepsilon_{22}^{f,t}} - \frac{1}{\varepsilon_{22}^{f,c}}\right) + \left(\frac{\varepsilon_{12}}{\varepsilon_{12}^{f}}\right)^2}}$$ (Equation 4)

$$\boldsymbol{f_3 = \sqrt{\left(\frac{\sigma_{33}}{F_{3z}}\right)^2 + \left(\frac{\sigma_{13}}{F_{sz}}\right)^2 + \left(\frac{\sigma_{23}}{F_{sz}}\right)^2}}$$ (Equation 5)

where $\varepsilon_{ii}^{f,t}$ and $\varepsilon_{ii}^{f,c}$, (i=1, 2), are the failure strains in the in-plane principal directions in tension and compression, respectively; ε_{12}^{f}, is the in-plane failure strain in shear; F_{3z}, is the peel (through thickness tensile) strength and; F_{sz}, is out of plane shear strength.

The failure strains were calculated by (Equation 6-7).

$$\boldsymbol{\varepsilon_{ii}^{f,t} = \frac{F_{ii}^{t}}{C_{ii}^{0}}}, i = 1, 2$$ (Equation 6)

$$\boldsymbol{\varepsilon_{ii}^{f,c} = \frac{F_{ii}^{c}}{C_{ii}^{0}}}$$ (Equation 7)

where, $F_{ii}^{t,c}$ is the corresponding strength in principal directions.

The in-plane damage variables (d_1 and d_2), evolves from 0 to 1, where 0 represents the undamaged material and 1 corresponds the failure state (Equation 8).

$$\boldsymbol{d_i = 1 - \frac{\varepsilon_{ii}^{f,t}}{f_i}\exp\left(\frac{C_{ii}\varepsilon_{ii}^{f,t}\left(\varepsilon_{ii}^{f,t} - f_i\right)l^*}{G_f^f}\right), i = 1, 2}$$ (Equation 8)

$$\boldsymbol{d_3 = \begin{cases} 0, f_3 < 1 \\ 0.95, f_3 \geq 1 \end{cases}}$$ (Equation 9)

where, l^* is the characteristic element length associated to the material, and G_f^f is the fracture energy in the fiber direction. Through thickness damage variable (d_3) is considered by a limiting factor of 0.95 when the damage initiation criterion through the thickness is equal or greater than one (Equation 9) [64].

2.1.3 Constitutive damage model for matrix pockets

Ductile damage approach was applied to predict the damage evolution in PA6 pockets. The model assumed that the equivalent plastic strain, ε^{pl}, at the onset of damage in PA6 pockets is a function of stress triaxiality, and strain rate. The stress triaxiality is defined by (Equation 10) [65].

$$\boldsymbol{\eta = -p/q} \quad \text{(Equation 10)}$$

where p is the pressure stress, and q is the Mises equivalent stress. The stiffness degradation of the material is defined through the dissipation of the fracture energy, adopted by the (Equation 11 [65], [66].

$$\boldsymbol{G_f^m = \int_{\bar{\varepsilon}_0^{pl}}^{\bar{\varepsilon}_f^{pl}} l^* \bar{\sigma} d\bar{\varepsilon}^{pl} = \int_0^{\bar{u}_f^{pl}} \bar{\sigma} d\bar{u}^{pl}} \quad \text{(Equation 11)}$$

where, $\bar{\varepsilon}_0^{pl}$ and $\bar{\varepsilon}_f^{pl}$ are the equivalent plastic strain at the onset of the damage and failure, respectively, and $\bar{u}^{pl}$ is the equivalent plastic displacement. The evolution of the damage variable is calculated in a linear and exponential form. (Equation 12) defines the damage evolution in the linear form where the damage index and equivalent plastic displacement has the linear relation. The exponential damage variable is computed by (Equation 13).

$$\boldsymbol{d_l = \frac{\int_0^{\bar{u}^{pl}} \bar{\sigma} d\bar{u}^{pl}}{G_f}} \quad \text{(Equation 12)}$$

$$\boldsymbol{d_{exp} = 1 - \exp\left(-\int_0^{\bar{u}^{pl}} \frac{\bar{\sigma} d\bar{u}^{pl}}{G_f^m}\right)} \quad \text{(Equation 13)}$$

where $\bar{\sigma}_y$, is the effective stress and $\bar{u}^{pl}$, is the equivalent plastic displacement, calculated by (Equation 14). The damage index evolves from 0 to 1, where 0 represents the undamaged material and 1 corresponds to the failure state.

$$\bar{\boldsymbol{u}}_{\boldsymbol{f}}^{\boldsymbol{pl}} = \boldsymbol{l}^{*}(\bar{\boldsymbol{\varepsilon}}_{\boldsymbol{f}}^{\boldsymbol{pl}} - \bar{\boldsymbol{\varepsilon}}_{\mathbf{0}}^{\boldsymbol{pl}}) \quad \text{(Equation 14)}$$

To generate the complex geometrical arrangement and distribution of the bundles/platelets within the PPMC and organosheet, a sequential adsorption probabilistic approach was used [57].

2.2 Modeling procedure for progressive failure analysis of PPMC

A 3D finite element computational model with the damage mechanism approach was used to simulate the three-point bending test using Abaqus implicit and predict the flexural modulus and strength of the PPMCs as well as the associated failure modes. The mesostructure of virtual PPMC is generated in DIGIMAT FE including 100% of platelet volume fraction using Monte-Carlo simulations [57]. The probabilistic simulation results (strength and modulus), as well as, experimentally measured mechanical properties, were assumed to follow normal distribution. Both distributions were compared for statistical significance using analysis of variance by the two-sample *t*-test. The following sections outlined the mesostructure generation of the virtual specimens and the damage mechanism used in the model.

2.2.1 Mesostructure generation for PPMC virtual specimen

The stochastic structural arrangement of platelets is calculated through the sequential adsorption algorithm and in a random placement the center of the platelets sequentially. The orientation probability distribution of platelets was extracted from the requested 2nd order orientation tensor (OT). PPMC coupon in Figure 6-a was shown as a misaligned individual platelet (shown in different colors) with 1" prepreg platelet mesostructure and the total element number of 24000. The platelets were generated within the voxel mesh by generating voxels into a platelet and assigning the local orientation vector (Figure 6-b-c). p^k in Figure 6-c indicated the vector of k-th platelet fiber direction. Virtual stochastic PPMC was modeled in the global coordinate system of (x_1, x_2, x_3) space with assigned local coordinate system of every platelet $(1_i, 2_i, 3_i)$ to represent

stacked misaligned platelets. Platelets were sequentially placed within the voxel mesh and the voxels within a platelet boundary were identified with orientation of belonging platelet. Figure 6-b shows two platelets along with their local material coordinate systems where "1" is the local platelet fiber direction and "2" is the local transverse direction. Figure 6-d shows a schematic of a platelet orientation vector in the global coordinate system. The platelet fiber orientation vector and global x_1x_2-plane are coplanar in the 2D random platelet distribution (φ=90°) and θ defines the misaligned angle of platelet with respect to global $x_1$direction. The discrete form of OT for N platelets with the 2D random orientation is given by (Equation 15).

$$\boldsymbol{A_{ij}} = \frac{\mathbf{1}}{\boldsymbol{N}} \sum_{\boldsymbol{k=1}}^{\boldsymbol{N}} \begin{bmatrix} (\boldsymbol{p_1 p_1})_k & (\boldsymbol{p_1 p_2})_k \\ (\boldsymbol{p_1 p_2})_k & (\boldsymbol{p_2 p_2})_k \end{bmatrix} \quad \textbf{(}\text{Equation 15}\textbf{)}$$

The first component of the OT ($a_{11} = {}^{1}/_{K} \sum_{k=1}^{K} \cos^2\theta_k$) is representative of the platelet degree of alignment in the global x_1 direction. The scattered distribution of the platelets within a PPMC coupon results in the non-uniform orientation of local platelet orientation within the volume of PPMC specimen. The 2D-random OT is attributed to $a_{11} = 0.5$ to sampling random numbers from the orientation distribution function.

Platelets were modeled as 3D elements (C3D8). Figure 6-b-c shows overlapping platelets including a cohesive interface and the schematic for the idealized stress components. The cohesive elements were placed at the platelet interface to define the normal and shear interactions between the neighboring platelets. The FVF of the platelets is equal to that of the prepreg tape and was included in the model by using characterized material properties[67]. Two approaches were used to generate the virtual morphology of the specimens, namely, (i) individual virtual coupons generated with the 2D random platelet orientation in a full-size flexural test specimen ($127 \times 25 \times 2.4mm$), and (ii) virtually cut coupons from a generated 5"×5" plaque with the

random platelet orientation (Figure 7). The latter option allowed us to consider the actual molded plaque geometry, which was used to prepare physical PPMC samples. The two approaches for generating PPMC samples were considered to study the effect of the sample size and the finite number of platelets in the volume of specimen on the predicted flexural mechanical properties. After generation of the virtual specimens, the model is imported into Abaqus to apply three-point bending with boundary conditions and constitutive models for the platelets and their interfaces [68]. Figure 7-e shows a deformed state of the 3-point bending model of a PPMC sample with 1" prepreg platelet length.

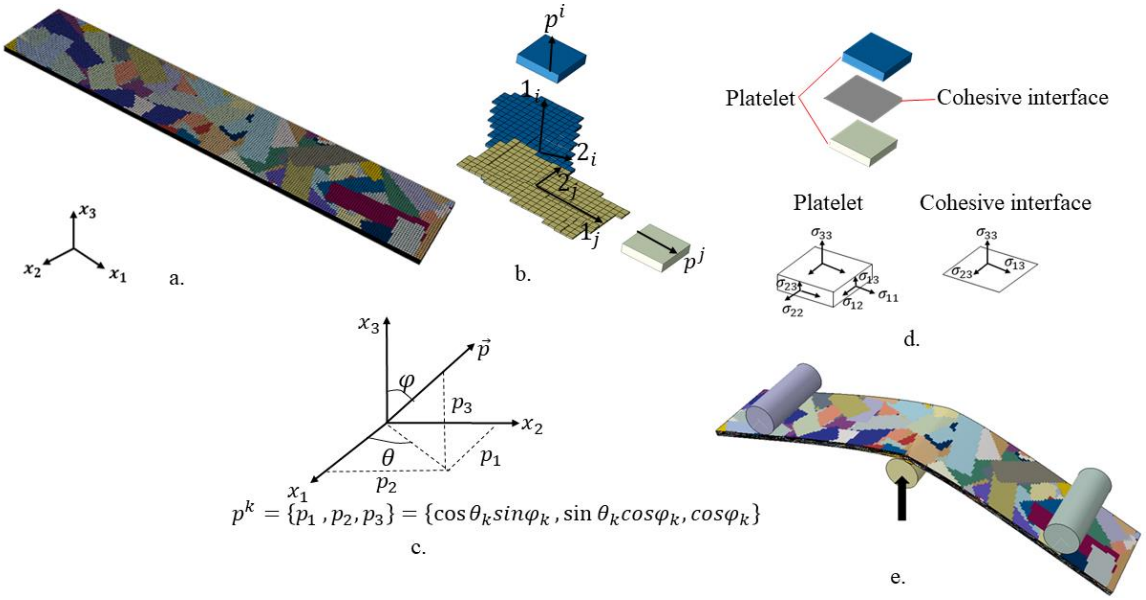

Figure 6 (a) A virtual coupon with prepreg platelet mesostructure (b) Schematic of the overlapping of the platelets with cohesive element (c) fiber direction vectors in the global coordinate system (d) stress components on a platelet and cohesive element (e) Deformed state of 3-point bending model

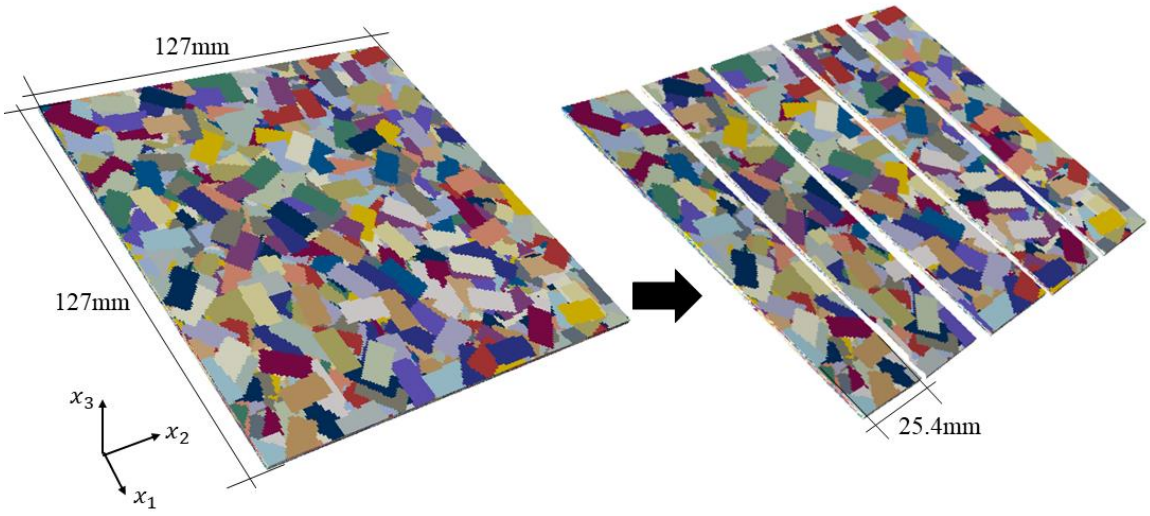

Figure 7 Virtual PPMC specimens cut from a plaque

2.2.2 Constitutive damage model for PPMCs

A stiffness reduction scheme is used to describe the damaged response of the platelets using user subroutine UMAT [69]. The individual platelets in meso-scaled computational model considered as a homogeneous orthotropic material with the properties of the parent unidirectional prepreg in which in-plane and out-of-plane damage is the result of the triaxial state of stress (Equation **1**). The damaged stiffness matrix (C_{ij}) depends on the virgin (undamaged) stiffness components (C_{ij}^0) and the state of the damage variables in the fiber direction (d_1) and transverse to the fiber direction (d_2) (Equation **2**). The failure initiation criterion is predicted by applying the damage initiation functions f_1 and f_2 for damage variable d_1 and d_2, respectively (Equation **3**). The damage variable d_1 and d_2 are computed by (Equation **8**), where the damage variable evolves from 0 to 1.

The CDM with orthotropic damage for platelets combined with a cohesive zone modeling (CZM) at the interfaces between platelets to capture debonding using a traction separation law.

(Equation 16) shows the constitutive equation law of traction separation where interlaminar σ_{ij} stress, δ_j is the relative separations between the elements, d is the damage variable, and $k_i^0 = 1 \times 10^6\ {}^{MPa}/_{mm}$ is the initial stiffness [70].

$$\begin{Bmatrix} \boldsymbol{\sigma_{13}} \\ \boldsymbol{\sigma_{23}} \\ \boldsymbol{\sigma_{33}} \end{Bmatrix} = \begin{bmatrix} \boldsymbol{(1-d)k_1^0} & \boldsymbol{0} & \boldsymbol{0} \\ \boldsymbol{0} & \boldsymbol{(1-d)k_2^0} & \boldsymbol{0} \\ \boldsymbol{0} & \boldsymbol{0} & \boldsymbol{(1-d)k_3^0} \end{bmatrix} \begin{Bmatrix} \boldsymbol{\delta_1} \\ \boldsymbol{\delta_2} \\ \boldsymbol{\delta_3} \end{Bmatrix} \quad \textbf{(}\text{Equation 16}\textbf{)}$$

The failure initiation criterion of the disbanding between the platelets are given by (Equation 17) where $N_{max} = 50MPa$ and $S_{max} = T_{max} = 80MPa$ are the cohesive strength.

$$\left(\frac{\boldsymbol{\sigma_{33}}}{\boldsymbol{N_{max}}}\right)^2 + \left(\frac{\boldsymbol{\sigma_{13}}}{\boldsymbol{S_{max}}}\right)^2 + \left(\frac{\boldsymbol{\sigma_{23}}}{\boldsymbol{T_{max}}}\right)^2 = \boldsymbol{1} \quad \textbf{(}\text{Equation 17}\textbf{)}$$

The propagation of the debonding is defined by a linear fracture mechanism of power law through (Equation 18) [71].

$$\frac{\boldsymbol{G_I}}{\boldsymbol{G_{IC}}} + \frac{\boldsymbol{G_{II}}}{\boldsymbol{G_{IIC}}} + \frac{\boldsymbol{G_{III}}}{\boldsymbol{G_{IIIC}}} = \boldsymbol{1} \quad \textbf{(}\text{Equation 18}\textbf{)}$$

where G_I, G_{II}, G_{III} are the work done by the tractions and their corresponding displacements in the normal and shear directions, and $G_{IC}, G_{IIC}, G_{IIIC}$ are the critical strain energy release rates corresponding to the fracture mode. The moduli and strength properties of the orthotropic platelets of IM7/8552 prepreg tape included in Appendix B following Ref. [72], [73].

2.2.3 Local coupling stiffness analysis

Classical lamination theory (CLT) was applied to study the variation of the local coupling stiffness within a PPMC coupon. CLT makes it possible to analyze coupling effects and predict strains, displacements, and curvatures that develop in a composite laminate as it is mechanically and thermally loaded based on the layer thickness and orientation [74]. Figure 8 represents the

cross-section view of 12 considered layers through the thickness of the virtual PPMC specimen with the thickness of a voxel (t_v) and 50 voxels in width for each layer. The stiffness matrix in the material coordinate system was calculated through (Equation 19).

$$\boldsymbol{Q} = \begin{bmatrix} \boldsymbol{Q_{11}} & \boldsymbol{Q_{12}} & \boldsymbol{0} \\ \boldsymbol{Q_{12}} & \boldsymbol{Q_{22}} & \boldsymbol{0} \\ \boldsymbol{0} & \boldsymbol{0} & \boldsymbol{Q_{33}} \end{bmatrix} \quad \text{(Equation 19)}$$

$$\boldsymbol{Q_{11} = \frac{E_1}{1-\nu_{12}\nu_{21}}, Q_{12} = \frac{\nu_{21}E_2}{1-\nu_{12}\nu_{21}}, Q_{22} = \frac{E_2}{1-\nu_{12}\nu_{21}}, Q_{33} = G_{12}}$$

where E_1 and E_2 are the elastic moduli of the unidirectional prepreg IM7/8552 in the fiber and transverse directions, respectively, G_{12} is the in-plane shear modulus, and ν_{12} and ν_{21} are the in-plane major Poisson's ratio. The transformed stiffness matrix ($\bar{Q}$), in the global coordinate system, is calculated through (Equation 20).

$$\bar{\boldsymbol{Q}} = \boldsymbol{T^{-1}Q}\begin{bmatrix} \boldsymbol{1} & \boldsymbol{0} & \boldsymbol{0} \\ \boldsymbol{0} & \boldsymbol{1} & \boldsymbol{0} \\ \boldsymbol{0} & \boldsymbol{0} & \boldsymbol{2} \end{bmatrix}\boldsymbol{T}\begin{bmatrix} \boldsymbol{1} & \boldsymbol{0} & \boldsymbol{0} \\ \boldsymbol{0} & \boldsymbol{1} & \boldsymbol{0} \\ \boldsymbol{0} & \boldsymbol{0} & \boldsymbol{0.5} \end{bmatrix} \quad \text{(Equation 20)}$$

$$\boldsymbol{T} = \begin{bmatrix} \boldsymbol{c^2} & \boldsymbol{s^2} & \boldsymbol{2sc} \\ \boldsymbol{s^2} & \boldsymbol{c^2} & \boldsymbol{-2sc} \\ \boldsymbol{-sc} & \boldsymbol{cs} & \boldsymbol{c^2 - s^2} \end{bmatrix}$$

where c and s are the cosine and sine of the average angle (θ) of the voxels within a layer which is the angle between the fiber orientation vector of voxels with respect to the global x_1 direction. The formulation of laminate stiffness matrix is written as (Equation 21) where N is the directional forces and M is the moments applied to a layer, and the deformations are combined from the strains (ε) and curvatures (κ).

$$\begin{Bmatrix} \boldsymbol{N} \\ \boldsymbol{M} \end{Bmatrix} = \begin{bmatrix} \boldsymbol{A} & \boldsymbol{B} \\ \boldsymbol{B} & \boldsymbol{D} \end{bmatrix}\begin{Bmatrix} \boldsymbol{N} \\ \boldsymbol{M} \end{Bmatrix} \quad \text{(Equation 21)}$$

The laminate stiffness matrix consists of the three sub matrices A, B, and D with the size of 3×3. A represents the extensional stiffness matrix, B the coupling stiffness, and D corresponds

to the bending stiffness matrix. To study the variability of the flexural stiffness of PPMC in the span direction of the virtual coupon, the B_{11} was calculated along the length of the coupon (x_1 direction). B_{11} component represents coupling between the normal strain due to bending, $\boldsymbol{\varepsilon_{11}}$, and the bending moment itself. (Equation 22) was used to calculate B_{11} of every 12 considered platelet layers along the length of the specimen where z_k and z_{k-1} were the location of the top and bottom of each equivalent layer with reference to the mid-surface.

$$\boldsymbol{B_{11} = \frac{1}{2}\sum_{k=1}^{12} \bar{Q}_{11}^{k}(z_k^2 - z_{k-1}^2)} \qquad \text{(Equation 22)}$$

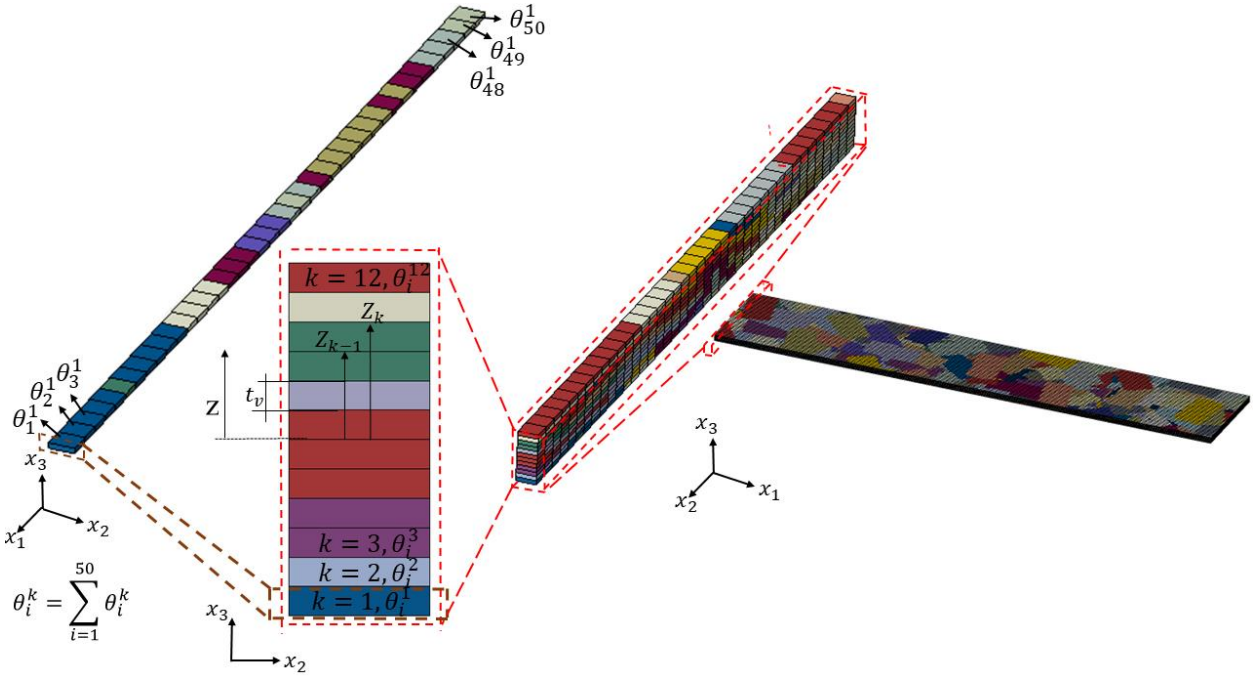

Figure 8 Considered layers within a virtual PPMC specimen

2.3 Multiscale modeling of freeze casted ceramic

For materials with a hierarchical microstructure, the multiscale homogenization procedure can be used for parametric studies to determine the role of morphological parameters on the effective properties [75]. Two approaches were used to develop the multiscale homogenization models for the compressive behavior of freeze-casted ceramic with the lamellar structure: (i) The RVE was developed based on the honeycomb analogy of lamellar walls considering the morphology of the material to predict the effective mechanical properties of the ice-templated ceramics under off-axis compressive loading (ii) A macroscale homogenized model was developed to predict the effective compressive properties (modulus as well as strength) and was used to understand the failure behavior of the freeze-casted ceramic. The continuum damage modeling was employed to describe failure modes in the longitudinal and transverse directions.

2.3.1 Micromechanical modeling of compressive behavior in freeze-casted ceramic

A novel computational micromechanical framework was proposed based on the developed representative volume element (RVE), which incorporates experimentally observed morphology of ice-templated alumina foam. The corresponding mechanical properties of the solid phase, required for the micromechanical analysis, were determined based on the following consideration. The elastic modulus of the alumina phase used was based on the load-displacement measurements of the single microscopic alumina platelet subjected to 3-point bending based on study by Feildin et al. [76], which measured modulus of 40GPa. The use of this material stiffness measured microscopically under bending in present work is attributed to lamellar walls undergoing bending under off-axis loading. Furthermore, the length scale of the lamellar wall thickness is similar to the single microscopic platelet. While single crystal shows some anisotropy in the elastic modulus, the mechanical properties of polycrystalline lamellar walls were assumed to be isotropic. The

strength of these polycrystalline walls is governed by the grain boundaries, rather than a single crystal, which are not easily extractable from a macroscopic sample. Therefore, three different values for material compressive strength were considered: 250MPa, 500MPa and 1GPa and were used for model calibration with the experimental results. These strength values are less than the typical values reported for single crystal of alumina oxide (2GPa [76], [77]), therefore, providing an appropriate range of strength for polycrystalline ice-templated lamellar walls.

To model the possible cracking under tensile conditions due to bending in the walls, the smeared cracking approach was used to describe the stress strain response of ice-templated alumina using the existing constitutive model in ABAQUS finite element software [78]. Smeared cracking approach provides a general capability for modeling brittle material subjected to the monotonic strain consisting of hardening yield surface in compression mode and a failure envelope for tensile mode. The failure envelope called crack detection surface characterized by the ultimate displacement calculated by (Equation 23), where u_0 is the ultimate displacement, G_f is the fracture energy per unit area and σ_u is the ultimate stress [68]. The material properties describing the elastic and smeared cracking behavior are shown in Table 1. Failure ratios Table 1 was specified to define the shape of the failure surface.

$$\boldsymbol{u_0 = 2G_f/\sigma_u} \qquad \text{(Equation 23)}$$

Table 1 Matrial properties

Property	Value
Young's modulus	40 GPa
Poisson ratio	0.21
Compressive strength	250; 500; 1000 MPa
Ultimate displacement for traction-separation behavior	0.98 µm
Ratio of the ultimate biaxial compressive stress to the ultimate uniaxial compressive stress **[68]**	1.16
Absolute value of the ratio between the uniaxial tensile stress at failure to the ultimate uniaxial compressive stress **[68]**	0.1
Ratio between the principal component of plastic strain at ultimate stress in biaxial compression to the plastic strain at ultimate stress in uniaxial compression **[68]**	1.28
Ratio between the tensile principal stress value at cracking in plane stress, when the other principal stresses reach its maximum value in compression, and the tensile cracking stress under uniaxial tension **[68]**	0.4

In the present study, the considered relative density for the model was equal to 21%, which matches the manufactured samples discussed in Section 2. Relative density in the RVE model depends on the lamellar wall thickness and wall spacing, which were selected based on the morphological observations of the equivalent alumina material composition from Ref. [38]. Specifically, lamellar wall thickness was 5.5 mm and the wall spacing was 23.3 mm. The hexagon cell size was chosen to be 130 mm, which allows for up to 9 lamellar walls in each hexagonal cell of the model making it more representative for the higher scale homogenization. During the unidirectional freeze casting of an aqueous ceramic suspension, ice crystals nucleate in the direction of the temperature gradient. Therefore, the freeze casted material develops parallel (lamellar) wall microstructure in the direction of freezing, x_1 (Figure 9). The lamellar walls exhibit various orientations of lamellar walls in $x_2 - x_3$ plane, which is perpendicular to the freezing

front direction. Based on this morphology, a honeycomb structural analogy was applied to develop the RVE of ice-templated ceramic (Figure 9-a) with the uniaxial direction of lamellar walls, x_1, and idealized in-plane wall orientation with 0^o, 45^o, 90^o and periodic geometry. Figure 9-b shows the off-axis RVE developed for ice-templated alumina with 12° off-axis angle. The proposed RVE was discretized using 3D solid finite elements.

In order to predict the bulk properties of the macroscale cellular solid, the periodic displacement boundary conditions were applied to the RVE model [79] to ensure that the opposite faces of the RVE have consistent deformation during the analysis. Periodic boundary conditions were enforced by pairing the nodes on the opposite faces of RVE and implemented using the displacement-based (Equation 24).

$$\boldsymbol{u_1(0, x_2, x_3) - u_1(L_1, x_2, x_3) = U_1} \quad \text{(Equation 24)}$$

$$\boldsymbol{u_2(x_1, 0, x_3) - u_2(x_1, L_2, x_3) = U_2} \quad \text{(Equation 25)}$$

$$\boldsymbol{u_3(x_1, x_2, 0) - u_3(x_1, x_2, L_3) = U_3} \quad \text{(Equation 26)}$$

where u_i is the corresponding nodal displacement on the face of RVE, U_1, U_2 and U_3 are the prescribed value for displacement in x_1, x_2 and x_3 direction, which are applied to RVE, L_1, L_2 and L_3 are the corresponding dimensions of the RVE, as shown in Figure 9.

The homogenized stress (σ_i) and strain (ε_i) obtained from the RVE analysis are calculated using the following equations:

$$\boldsymbol{\varepsilon_i = \frac{U_i}{L_i}} \quad \text{(Equation 27)}$$

$$\boldsymbol{\sigma_i = \frac{R_i}{A_i}} \quad \text{(Equation 28)}$$

where U_i is the corresponding displacement, L_i is the length of the RVE in a given coordinate direction, R_i is the reaction force acting on RVE as a result of applied displacement boundary condition, and A_i are the area of RVE faces.

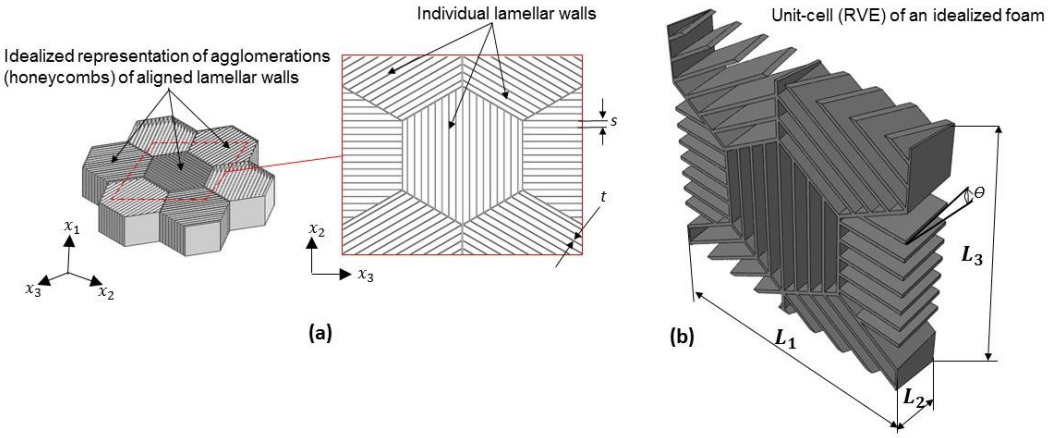

Figure 9 (a) Developed micromechanical model based on honeycomb structural analogy; s and t represent thickness of the walls and distance between them, respectively (b) Developed RVE for micromechanical analysis 12º off-axis angle

The developed RVE has three planes of symmetry, that is described by homogenized orthotropic constitutive stress-strain relationship. Therefore, the effective stress-strain behavior for homogenized orthotropic material can be used to describe ice-templated material system and is given by (Equation 29).

$$\begin{Bmatrix} \varepsilon_1 \\ \varepsilon_2 \\ \varepsilon_3 \\ \gamma_4 \\ \gamma_5 \\ \gamma_6 \end{Bmatrix} = \begin{bmatrix} \frac{1}{E_1} & -\frac{v_{21}}{E_2} & -\frac{v_{31}}{E_3} & 0 & 0 & 0 \\ -\frac{v_{12}}{E_1} & \frac{1}{E_2} & -\frac{v_{32}}{E_3} & 0 & 0 & 0 \\ -\frac{v_{13}}{E_1} & -\frac{v_{23}}{E_2} & \frac{1}{E_3} & 0 & 0 & 0 \\ 0 & 0 & 0 & \frac{1}{G_1} & 0 & 0 \\ 0 & 0 & 0 & 0 & \frac{1}{G_2} & 0 \\ 0 & 0 & 0 & 0 & 0 & \frac{1}{G_3} \end{bmatrix} \times \begin{Bmatrix} \sigma_1 \\ \sigma_2 \\ \sigma_3 \\ \tau_4 \\ \tau_5 \\ \tau_6 \end{Bmatrix} \quad \text{(Equation 29)}$$

2.3.2 Homogenized modeling of compressive behavior in freeze-casted ceramic

A macroscale homogenized model was developed to predict the effective compressive properties and was used to understand the failure behavior of the freeze-casted ceramic. The transversely isotropic stress-stress relationship is used based on the material planes of symmetry. Micromechanical analysis of RVE was used to predict material constants and as the input parameter of homogenized modeling. Normal distribution was defined as a spatially varying field over elements calculated through the measured distribution of the local orientation in the lamellar structure and implemented through the discrete field approach. Consecutive equations for coordinate transformations were used to define the discrete field orientation for the material. Freeze casted ceramic has the hierarchical structure with specific pore volume affecting the material's mechanical properties and failure behavior. A random distribution of elements with specific volume fraction was defined as the porous element. The volume fraction and material properties of the porous elements were defined through the model's calibration. The continuum damage modeling was employed to describe failure modes in the longitudinal and transverse directions.

A user material (UMAT) FORTRAN subroutine for Abaqus standard implicit was employed to simulate the damage initiation and propagation in the longitudinal and transverse directions. The longitudinal damage implies the stiffness degradation in the anisotropic homogenized material due to the in-plane stresses. The transverse damage index shows the degradation of the material stiffness transverse to the loading direction. The material was assumed as a transversely isotropic material following the constitutive relationship in (Equation 1).

(Equation 30) shows the damage initiation criteria to predict the failure initiation in the loading direction when the corresponding criterion reaches one. Hill yield criterion was used to define the damage initiation to predict the failure initiation in transverse to the direction (Equation 31).

$$\boldsymbol{f_1 = \sqrt{\frac{\sigma_{11}^2}{\sigma_{11}^{f,t}\sigma_{11}^{f,c}} + \sigma_{11} \times \left(\frac{1}{\sigma_{11}^{f,t}} - \frac{1}{\sigma_{11}^{f,c}}\right)}} \quad \text{(Equation 30)}$$

$$\boldsymbol{f_2 = \sqrt{\left(\frac{1}{\sigma_{22}^{f,c^2}} - \frac{1}{2\sigma_{11}^{f,c^2}}\right)(\sigma_{22} - \sigma_{33})^2 + \frac{1}{\sigma_{23}^{f\ 2}}\sigma_{23}^2}} \quad \text{(Equation 31)}$$

where $\sigma_{\mathrm{ii}}^{f,t}$ and $\sigma_{\mathrm{ii}}^{f,c}$ are the failure stresses in the principal directions in tension and compression, respectively. The damage variables (d_1 and d_2), evolves from 0 to 1, where 0 represents the undamaged material and 1 corresponds to the failure state (Equation 32).

$$\boldsymbol{d_i = 1 - \frac{\sigma_{\mathrm{ii}}^f}{C_{\mathrm{ii}} f_{\mathrm{i}}} \exp\left(\frac{\sigma_{\mathrm{ii}}^f\left(\sigma_{\mathrm{ii}}^f / C_{\mathrm{ii}} - f_{\mathrm{i}}\right) l^*}{G_f^f}\right), i = 1, 2} \quad \text{(Equation 32)}$$

where, l^* is the characteristic element length associated to the material, and G_f^f is the fracture energy in the lamellar direction.

3 EXPERIMENTAL PROCEDURE AND METHOD

3.1 Experimental characterization of organosheet

This section describes the experimental test procedures used to characterize the morphology and mechanical response of the organosheet. DSC was employed to quantify the degree of crystallinity in the organosheet and was used to compare it with pure PA6. Microscopic analysis was used to characterize the volume fractions of fibers, the distribution of bundle alignment, and bundle cross-sectional dimensions. The tensile and three-point bending tests were used to study the effective mechanical response of the organosheet material. Notch sensitivity analysis was performed using the notched tensile testing. The tensile properties of LDFC with the flow-induced orientation state were studied experimentally.

3.1.1 DSC characterization

DSC is a thermo-analytical technique used to measure the change of the difference in the heat flow rate to the sample, subjected to a controlled temperature program [80]. In DSC method, the test sample and reference pan are heated and cooled under the identical condition to measure the difference in the amount of heat absorbed or released between the sample and the reference as a function of temperature [81] [82], [83]. DSC analysis was conducted with a heating rate of 10^{o}C/min from isothermal up to 250^{o}C. Nitrogen atmosphere with a flow rate of 50mL/min was used. Degree of crystallinity of the organosheet material was measured using the corresponding endothermic peak during melting, which corresponds to the amount of crystalline phase in PA-6 matrix.

3.1.2 Microscopy analysis

Fiber orientation state, bundle orientation state and associated volume fractions were measured with high-resolution microscopy analysis. The global fiber volume fraction (FVF_{glob})

in the organosheet was computed based on binarization of a polished cross-sectional image (Figure 1-c). The original micrograph contained 8-bit grayscale images with 256 different intensity levels. Using ImageJ software, each micrograph was binarized with an adaptive threshold and 256 levels were reduced to 2 levels of black and white color scheme referred to the matrix and fiber region, respectively. In the adaptive binarization method, the brightness of the background and the saturation of the black areas along the line was adjusted to find optimal binarization parameters for each separate line fragment. The high-resolution micrographs with visible and recognizable fiber boundaries were used in this study for adaptive binarization and the threshold was selected to ensure accurate representation of the fiber boundaries while choosing the threshold intensity during FOD measurements. The known weight fraction of glass fiber was used to ensure the correct volume fraction was determined by image analysis.

The fiber volume fraction within a single bundle is an important variable governing the effective (homogenized) properties of the composite. Therefore, the fiber volume fraction in bundles was measured by identifying the individual bundles and computing the corresponding FVF in each bundle case. Bundle volume fraction can be calculated from (Equation 33).

$$\boldsymbol{FVF_{glob} = FVF_{bundle} \times BVF} \qquad \text{(Equation 33)}$$

where FVF_{glob}al is the FVF in the entire micrographs, FVF_{bundle} is the FVF in the bundles and BVF is the bundle volume fraction.

The planar fiber orientation was assumed, leading to the spatial orientation of fibers in each bundle to be defined as the 2nd order symmetric 2×2 tensor (Equation 34) calculated as the dyadic product of fiber orientation vectors p_i (Equation 35). The orientation vector was calculated based on angle ψ_i between the plane's normal and the cylinder's longitudinal axis of the fiber

shown in Figure 10-a. The angle of ψ_i was calculated by (Equation 37), where l_i and h_i, shown in Figure 10-b, are the major and minor diameter of the ellipse shape fiber, respectively. Figure 10-c shows the distribution of fiber diameters within the selected bundle in the range of 10-16μm, indicating that over two-thirds of fiber diameters were distributed in the range of 12 to 14 μm. (Equation 38) was used to calculate the individual selected bundle orientation by taking the average over the calculated fibers orientation in the bundle, where *n* is the number of the fibers within the bundle [84]–[86].

$$\boldsymbol{A_{ij\_fiber}} = \begin{bmatrix} \boldsymbol{a_{11}} & \boldsymbol{a_{12}} \\ \boldsymbol{a_{21}} & \boldsymbol{a_{22}} \end{bmatrix} \quad \text{(Equation 34)}$$

$$\boldsymbol{a_{ij}} = \boldsymbol{p_i p_j} \quad \text{(Equation 35)}$$

$$\boldsymbol{p_i} = \begin{bmatrix} \boldsymbol{cos\psi_i} \\ \boldsymbol{sin\psi_i} \end{bmatrix} \quad \text{(Equation 36)}$$

$$\boldsymbol{\psi_i} = \mathbf{acos}\ (\boldsymbol{h_i/l_i}) \quad \text{(Equation 37)}$$

$$\boldsymbol{A_{ij\_bundle}} = \frac{\sum_n \boldsymbol{A_{ij}}}{\boldsymbol{n}} \quad \text{(Equation 38)}$$

In order to calculate the global bundle orientation tensor in the organosheet, (Equation 39) was applied using the area weighting factor, where *k* is the number of the recognized bundles within the micrograph and w_k is the area weighing factor of the selected bundle, calculated by (Equation 40). Ellipse fitting on the recognized labeled bundle was performed by Ellipse Fit software [87] to measure the area of the bundles, and the major and minor diagonals, shown in Figure 10-d for a single bundle, where k'_i and h'_i is the measured major and minor diagonals, respectively. Measured major and minor diagonals values in the plane of cut were corrected using the average of fibers angle in the bundle.

$$A_{ij} = \frac{\sum_k w_k A'^{k}_{ij}}{\sum_k w_k} \quad \text{(Equation 39)}$$

$$w_i = A_i \times cos\,(\psi'_i) \quad \text{(Equation 40)}$$

where A_i is the elliptical cross-sectional bundle area in the plane of the cut, and ψ'_i is the average of fibers angle in the bundle.

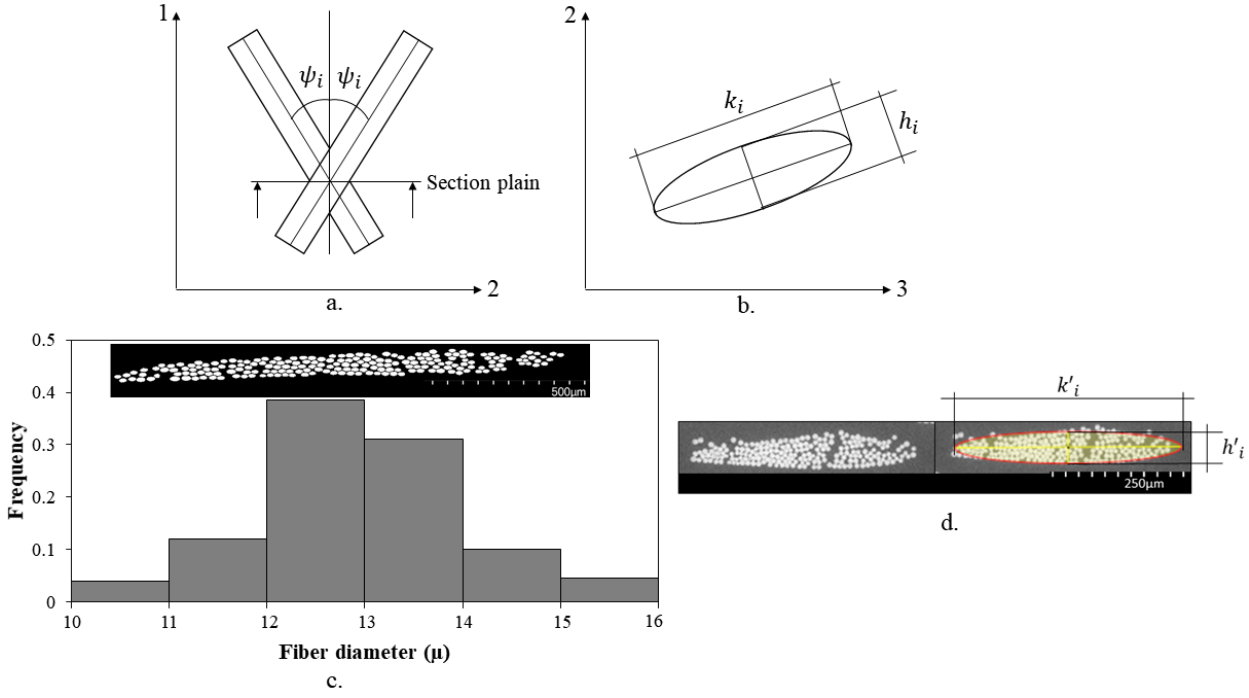

Figure 10 (a) Schematic of orientations for a fiber (b) elliptical cross-section of fiber (c) fiber diameter distribution within a selected bundle (d) An example of ellipse fitting on the identified bundle

3.1.3 Failure criteria of notched composite

Using composites in structural components necessitates drilling holes to join structural parts that leads to stress concentrations, resulting in reduced strength and localized failure of the material [88]. Since stress distribution scales with the hole size, the stress concentration around

the hole is believed to control the fracture behavior in composite laminates. Whitney and Nuismer [15-16] developed a criterion to account for OHT notch strength sensitivity by considering the stress gradients near geometrical notch discontinuities as a point stress criterion (PSC). They assumed that failure of the notched composite laminate occurs when the stress, σ_x, at a certain distance,d_0 , ahead of the notch with the specific radius, *R*, reaches the unnotched strength. PSC expressed in (Equation 41).

$$\boldsymbol{\sigma_x(R + d_0, 0) = \sigma_0} \quad \textbf{(}\text{Equation 41)}$$

The notch strength, σ_N, can be calculated by using PSC equation in relation with longitudinal stress at the crack tip (Equation 42)) [91], [92].

$$\frac{\boldsymbol{\sigma_N}}{\boldsymbol{\sigma_0}} = \frac{\boldsymbol{2}}{\boldsymbol{2 + \lambda^2 + 3\lambda^4 - (K_\infty - 3)(5\lambda^6 - 7\lambda^8)}} \quad \textbf{(}\text{Equation 42)}$$

$$\boldsymbol{\lambda = R/(R + d_0)} \quad \text{(Equation 43)}$$

where σ_0 is the unnotched strength; K_∞ is the stress concentration factor of an infinite plate with circular hole, which can be calculated with the effective engineering constants of material in principle directions (Equation 44) [29-30]. To calculate the K_∞ of organosheet material, the measured engineering constants were used (Table 2).

$$\boldsymbol{K_\infty = 1 + \sqrt{2(\sqrt{E_1/E_2} - \nu_{12} + \frac{E_1}{2G_{12}})}} \quad \textbf{(}\text{Equation 44)}$$

Table 2 Mechanical properties of organosheet

Material property	Numerical value
Longitudinal modulus, $\boldsymbol{E_1(GPa)}$	9
Transverse modulus, $\boldsymbol{E_2}$ $\boldsymbol{(GPa)}$	6.86
Shear modulus, $\boldsymbol{G_{12}}$ $\boldsymbol{(GPa)}$	1.97
Poisson's ratios,$\boldsymbol{\nu_{12}}$	0.34

To improve the accuracy of notched strength sensitivity model, Pipes et al. [18], [22-23] assumed that the characteristic distance is a power function of the hole radius (Equation 45). Modified point stress criterion, MPSC, model requires an exponential parameter to the PSC and as a result the parameter λ derives from (Equation 46).

$$\boldsymbol{d_0 = (R/R_0)^m/C} \quad \textbf{(}\text{Equation 45)}$$

$$\boldsymbol{\lambda = 1/(1 + R^{m-1}C^{-1})} \quad \text{(Equation 46)}$$

where R_0 is a reference radius and chosen as 1mm, m is an exponential parameter of characteristic length change, C is the notch sensitivity factor. The analytical strength model is restricted to a plate with an infinite width-to-hole diameter ratio. Therefore, the notch strength model in OHT sample requires a correction factor for the stress concentration factor, K, due to $\frac{K}{K_\infty} > 1$ to account for the finite width of the coupon (Equation 47).

$$\boldsymbol{\sigma_N(\infty) = \sigma_N(w)\frac{K}{K_\infty}} \quad \textbf{(}\text{Equation 47)}$$

$$\frac{\boldsymbol{K}}{\boldsymbol{K_{\infty}}} = \frac{\mathbf{2} + (\mathbf{1} - \boldsymbol{d/w})^{\mathbf{3}}}{\mathbf{3}(\mathbf{1} - \boldsymbol{d/w})} \quad \text{(Equation 48)}$$

where $\sigma_N(w)$ is the experimental strength of a plate with a specific width *(w)*, $\sigma_N(\infty)$ is the corresponding strength of an infinite plate, and *K* is the stress concentration factor with finite width derived from (Equation 48) [16], [27-28].

3.1.4 Tensile and three-point bend testing

The flexural and tensile tests were performed to analyze the impact of the variability of the mesostructure in organosheet on the flexural and tensile behavior. The tensile specimens were fabricated in accordance with ASTM D3039. Compression molding was performed using two layers of organosheets, cut by a high-performance waterjet cutter, in a stainless-steel mold. The depth of the mold was 25.4 mm with no cavity in between the top and bottom part parts. The surfaces of the mold were coated with high-temperature release wax before inserting the two layers of organosheet in the mold to prevent the damage of the molded sample during extraction of the sample from the mold. Hot press was used for melting and consolidation process. The temperature of the press was increased to 230ºC and 5-ton load was applied on the 10×10 inch panel for 15min. Then, the heating power was turned off and the mold remained under the pressure. The panel was cooled down at room temperature. The thickness of the fabricated samples was 2.5 mm. Specimens with dimensions of 127×25 mm were cut by a water jet machine. The end tabs were bonded on both ends of the tensile specimen. The specimens were tested under tension and three-point bending with 20, 30, 50, and 70mm loading span using the MTS test machine with a 10kN load cell. Digital image correlation (DIC) was used to measure the strain distribution around the hole and to measure the average strain using a virtual extensometer in the loading direction on the surface of the coupons during the experiment. DIC method is based on capturing images of the surface pattern on the sample during the test. White random, scattered white pattern was spray-

painted on the black surface of the samples to aid in computing and visualizing the strain deformation. ARAMIS GOM Correlate software was used to analyze strain components. The far field applied stress was calculated from the force measured with the load cell by dividing the applied force by the gross cross-sectional area of the coupons. The effective stress was calculated from the force cell in the MTS machine, force divided by cross section area for tensile stress and flexural stress was calculated by (Equation 49). The average tensile strain was measured by DIC in the loading direction on the front face of the specimen for tensile tests and the effective flexural strain was calculated with (Equation 50).

$$\boldsymbol{\sigma = \frac{3FL}{2bt^2}} \qquad \text{(Equation 49)}$$

$$\boldsymbol{\varepsilon = \frac{6tD}{L^2}} \qquad \text{(Equation 50)}$$

where, F is the applied load, L is the span length, b is the width of the specimen, t is the thickness and D is the deflection.

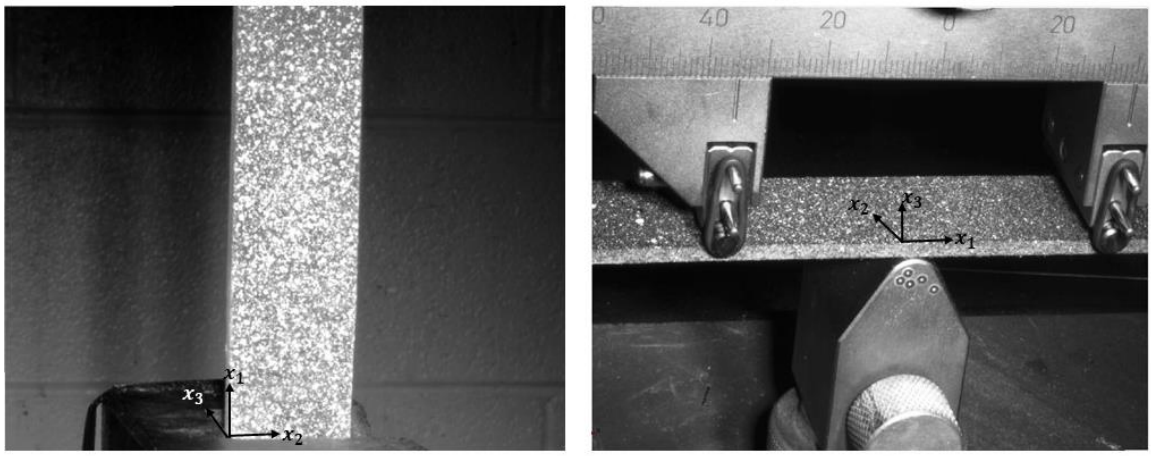

a. b.

Figure 11 DIC image for tensile test (a) and three-point bending with 70 mm span (b)

3.1.5 Notched tensile testing

Three sizes of the OH center-located notch of 2mm, 4mm, and 6mm in diameter was drilled in the coupons. PA6 matrix is a ductile polymer, thus allowing to avoid any damage around the circumference of the notch. Three panels were processed, and five coupons were fabricated for every batch of notched samples with prescribed notched size. The tensile strength of notched and unnotched coupons was measured using the MTS test machine with a 10kN load cell. Digital image correlation (DIC) was used to measure the strain distribution around the hole and to measure the average strain using a virtual extensometer in the loading direction on the surface of the coupons during the experiment. Figure 12 shows the tensile test set up for notched and unnotched coupons captured with DIC camera. The far field applied stress was calculated from the force measured with the load cell by dividing the applied force by the gross cross-sectional area of the coupons.

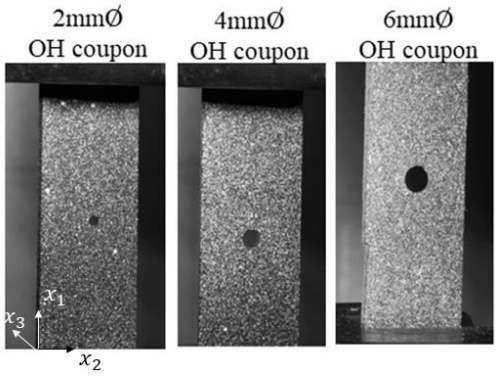

Figure 12 Notched tensile coupons on tensile test set-up

3.1.6 Tensile testing of organosheet processed by partial mold coverage

Four plaques were compression molded with 40%, 50%, 60%, and 80% center mold coverage. The compression direction was in x_3, and the mold cavity restricted flow in the x_2-

direction. The material flows in x_1-direction under compression molding resulting in the preferential fiber alignment in the flow direction (Figure 13). In order to have a consistent thickness of the molded organosheet, the number of the organosheet layers used for molding depends on the mold coverage. Two layers of orgabosheet were used for full coverage and four for 40%. Tensile specimens were cut from the molded organosheet in the x_1 direction. Five coupons were fabricated for every mold flow condition. The loading direction in tensile testing was along the x_1. DIC was used to measure the strain distribution during the experiment.

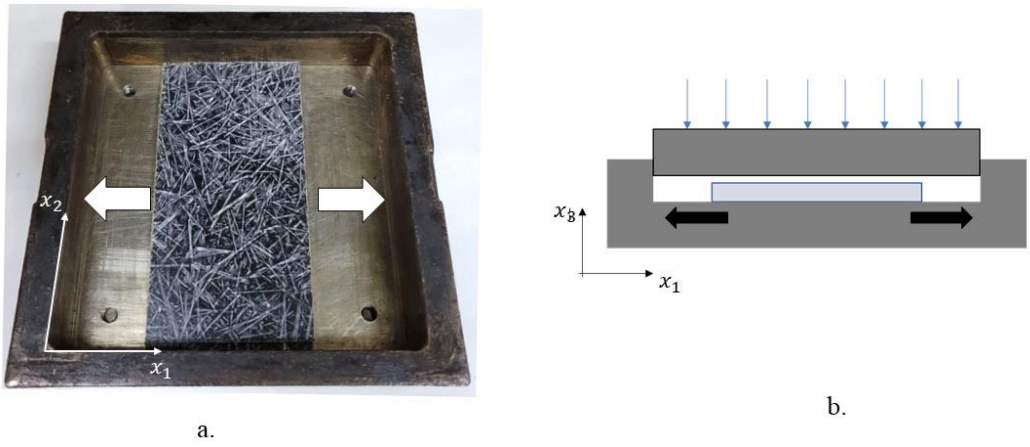

Figure 13 (a) Center charge of mold (b) Schematic of partial mold coverage

3.2 Experimental characterization and method for PPMC

The PPMC material system used for this study was a unidirectional Hexcel carbon fiber thermoset prepreg tape (IM7/8552). Three groups of coupons were fabricated with platelet length of 1/4", 1/2", and 1" to study the effect of the platelet length on the distribution of the effective flexural properties of stochastic PPMC. The platelet width (w_p) and thickness (l_p) were 6.35 and

0.13 mm, respectively. The thickness and width of the fabricated coupons were 25 and 2.4 mm, respectively. In the following sections, the microscopy analysis to calculate the platelet orientation state and the mechanical test procedure are described.

3.2.1 Fiber orientation measurement using microscopy analysis

The stochastic mesostructure of PPMCs is achieved by a random arrangement of the platelets in the mold following by an anisotropic flow of heterogeneous compound, results in a relocation and reorientation of the platelets [13]. A microscopy analysis was used to measure the platelet orientation state in PPMCs with specified platelet length. Since the planar fiber orientation was assumed, the spatial orientation of fibers in each platelet was defined as the 2nd order symmetric tensor calculated as the dyadic product of the fiber orientation vector p_i (Equation 31) based on the angle ψ_i between the plane's normal and the cylinder's longitudinal axis of the fiber. The angle of ψ_i is calculated by (Equation 37), where l_i and h_i are the major and minor diameter of the ellipse shape fiber, respectively. (Equation 38) was used to calculate the individual platelet orientation by taking the average over the calculated fibers orientation in the platelet, where n is the number of the fibers within the platelet. The global platelet orientation was measured by taking the average over the calculated individual platelet orientations (Equation 51) where n_p is the number of the platelets [84], [100].

$$\boldsymbol{A_{ij\_Global} = \frac{\sum_n A_{ij\_platelet}}{n_p}} \qquad \textbf{(Equation 51)}$$

3.2.2 Three-point bend testing of PPMC

The flexural tests were performed to analyze the impact of the platelet length within the PPMC on the flexural properties (strength and modulus). Compression molding was performed using scattered prepreg platelets with prescribed length in a $127mm \times 127mm$ stainless-steel

mold. Hot press was used for cure and consolidation process. The mold was preheated at 108 C for 35 minutes in the oven. Then, the load of 15 MPa was applied on the mold under the press for 30 minutes followed by raising the temperature to 180 °C and the mold was remained under pressure for 2 hours. Then, the heating power was turned off and the mold was cooled down to room temperature. Specimens with dimensions of 127 mm × 25 mm were cut by a water jet machine. 5 specimens were fabricated for every group of PPMC coupons with prescribed length of 1", ½", and ¼". The specimens were tested under three-point bending with using the MTS test machine with a 10kN load cell. Digital image correlation (DIC) was used to evaluate the strain distribution field on the surface of the specimens by capturing images of the surface pattern during the test. The black and white speckle pattern was spray-painted on the surface of the samples to aid in computing and visualizing the strain deformation. ARAMIS GOM Correlate software was used to analyze strain distribution. Figure 14 shows three-point bending setup with 90 mm span for a PPMC sample captured with DIC camera. The effective flexural modulus and strength of stochastic PPMC coupons were measured in a displacement-control three-point bend tests with the span of 90mm with crosshead rate of 2 mm. Flexural stress and strain stress were calculated through (Equation 49) and (Equation 50), respectively.

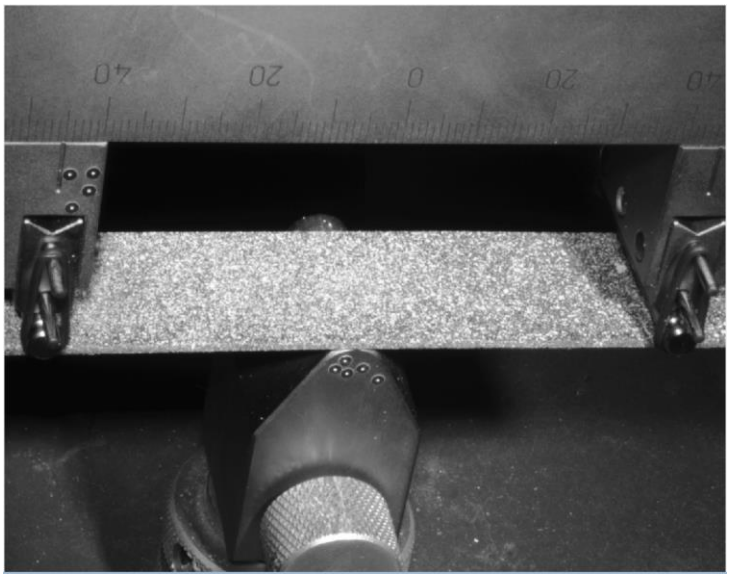

Figure 14 Three-point bending setup for a PPMC sample with 90 mm span

3.3 Processing and experimental procedure for freeze casted ceramic

Ice-templated porous alumina produced from Al_3O_3 powder with equiaxed morphology and the particle size of 0.3µm with the surface area of $8m^2/g$ (APA-0.5, Sasol, Tuscon, AZ). The samples were provided by Laboratory for Extreme and Energy Materials at Old Dominion University and followed the fabrication procedure described in detail in Ref. [38], [101]. Deionized water was used as the solvent and 0.5wt% of ammonium polymethacrylate anionic was added to the slurry. After preparing the slurry, zirconia balls (ZrO_2) in 5mm diameter used to stir the slurry magnetically for 24 hours in order to disperse alumina in the solvent. Then, 5 wt% of poly-(2-ethyl-2-oxazoline) was added to the slurry and stirred for an hour. After separation of the zirconium balls, the suspension was de-aired for 30 minutes. The ceramic suspension was prepared with 15 vol% of solid loading. The aqueous particulate suspension was solidified under a unidirectional temperature gradient applying a custom-made device for unidirectional freeze casting of AL_2O_3. The suspension placed inside an insulated Teflon cylinder on a steel plate with a thickness of 5mm,

filled with liquid nitrogen and a gap adjusted between the suspension and liquid nitrogen. A thermocouple measures the temperature gradient during the freezing process. During the freezing, the ceramic particles entrapped within the ice crystals or ejected resulting in microstructure with the anisotropic lamellar pore morphology [5], [38]. The rate of freezing front velocity was shown to be an important feature for controlling the morphology of the porous structure [38]. The estimated freezing front velocity is13.6 m/sc: calculated by dividing the frozen sample height with the time required to complete the solidification [38]. Afterward, samples were sublimated in a freeze-dryer (Freeze Dryer 2.5L, Labconco, Kansas City, MO) at the low pressure of 0.014 mbar and $-50°C$ for 96 hours. Finally, samples were sintered at the temperature of 450ºC for 4 hours and the rate of 3°C/min, and then were heated to 1550ºC and held for 4 hours and the rate of 5°C/min in a furnace (KSL-1700X, MTI Corporation, Richmond, CA). Finally, samples were cooled to the room temperature at a rate of 5 °C/min.

The samples for mechanical testing were extracted from the central part of the fabricated piece with dimensions $6 \times 6 \times 6\, mm^3$ in order to ensure the uniform relative density. Relative density, as the microstructural characterization, was calculated based on sintered density of samples and the bulk density of alumina powder using (Equation 52).

$$\boldsymbol{\rho_r = \frac{\rho}{\rho_b} = \frac{mV^{-1}}{\rho_b}} \qquad \text{(Equation 52)}$$

ρ_r is the relative density, ρ is the sintered density of the samples, ρ_b is the bulk density of ice-templated alumina, m is the mass of the sample, and $\boldsymbol{V}$ is the volume of the sample. In this study, samples are produced with 21% of relative density.

3.3.1 Sample fabrication and testing

Ice-templated alumina exhibits varying lamellar wall orientation in the plane transverse to ice growth direction shown in Figure 15. The ice-templated scaffolds can be subjected to off-axis compressive loading with respect to the ice-crystal growth direction. Figure 16-a shows a schematic for off-axis compressive loading of alumina with respect to the principal material coordinate system, *1-2*. The orientation of the off-axis loading is defined by angle □. In order to study the compressive behavior of the ice-templated alumina under different off-axis loading, samples were cut with different orientation relative to the ice growth. During the freeze casting, ice crystals nucleate and grow from the bottom to the top of the suspension in the direction of the temperature gradient. The processed sintered samples had diameter and height of 19 mm and 45 mm, respectively [38], [101]. The bottom of the samples had isotropic dense layers of the particles with no directional structure, because of the super cooling ahead of the freezing front [36]. Furthermore, decreasing the freezing front velocity from the bottom to the top of the slurry during the freeze casting can cause significant changes in the microstructure to an isotropic cellular structure and eventually a lamellar dendritic morphology [36], [102]. Therefore, the specimens were cut from the homogeneous lamellar section, located in the middle of the freeze cast samples at 19.5 mm and 25.5 mm from the bottom plane [38]. Diamond cutting system was used to cut the final sample cubes in $6 \times 6 \times 6\, mm^3$. The samples were cut in three different direction, longitudinal, perpendicular orientations and with 15° relative to the ice growth direction.

A compression test was carried out using the MTS test machine with a 10kN load cell and 1min/mm rate of crosshead. In all tests the load was recorded and used to calculate the homogenized stress carried by the cellular solid. Compressive strain is captured simultaneously by 3D DIC system and used for determining stress-strain profiles.

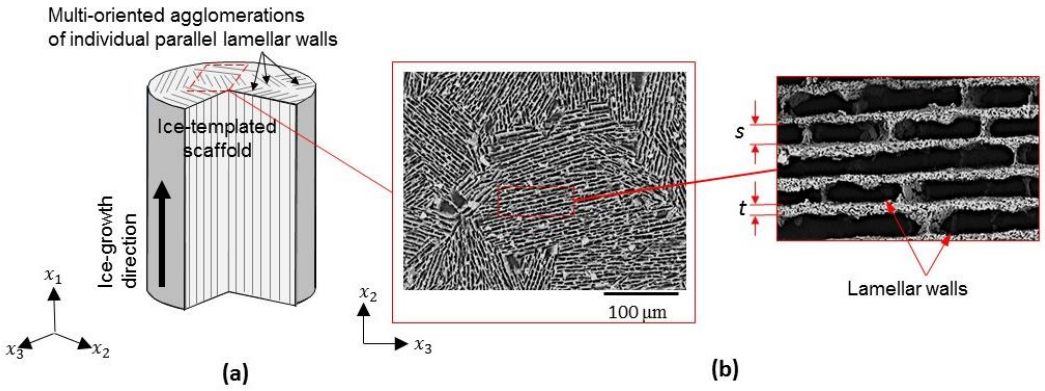

Figure 15 (a) Schematic of ice-template ceramic foam, showing principal composite directions (b) Micrographs showing agglomerations of parallel lamellar walls; s and t represent wall thickness and wall spacing, respectively

The 3D DIC strain measurement system was used for measuring strain on the surface of the sample. A black pattern was spray painted on the surface of the sample to create the random pattern in order to conduct the correlation of the undeformed and deformed patterns. The analysis of strain components was conducted by ARAMIS GOM correlate software. Figure 16-b shows the speckle pattern on the sample, providing a surface recognized by DIC to measure the surface deformation during the test.

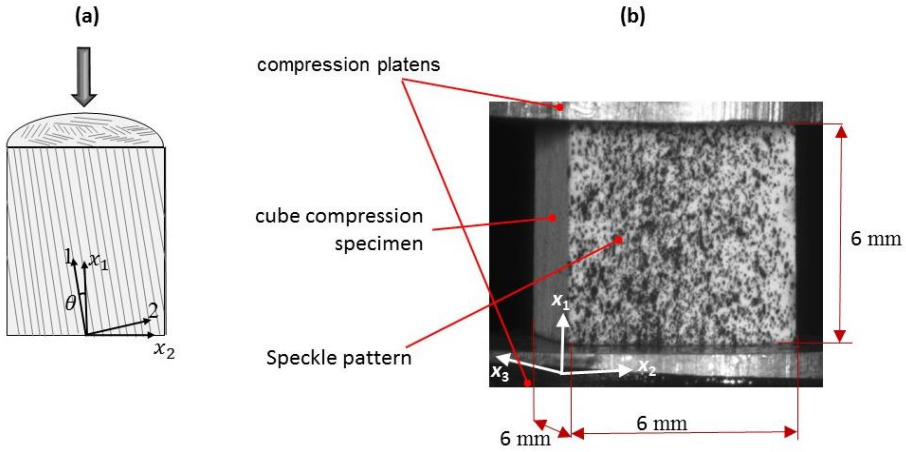

Figure 16 (a) Schematic of compression off-axis loading at an angle θ between the loading direction and the direction of crystal growth (the foam principal "1"-direction) (b) experimental set-up for compression test

4 MATERIAL CHARACTERIZATION OF ORGANOSHEET

This chapter discusses the calculation of the degree of crystallinity in the organosheet to evaluate the effect of in-situ polymerization on the crystallinity of the PA6 in the organosheet compared with that of the pure PA6. Then, the effective properties and the plasticity of the pure PA6 were measured through the standard tensile testing. An elastic-plastic finite element model was applied for PA-6 tensile test to calibrate the material constitutive model using the test data. Finally, the measured fiber bundle orientation and dimension using the microscopy analysis was explained and the calculated homogenized properties of the bundles was discussed. The characterization results were used to generate the morphologies of the virtual organosheet models and adopt the mechanical properties for the modeling.

4.1 DSC thermal analysis

The presence of the fiber reinforcements in the organosheet and the in-situ polymerization process may affect the nucleation and growth of crystalline phase in PA6. The degree of crystallinity was defined by (Equation 53) considering a baseline from the onset of melting to the crystalline phase and calculating the enthalpy of fusion from the area under this endotherm [103].

$$\chi = \frac{\Delta H_m}{(1 - W_f)\Delta H_{100}} \qquad \text{(Equation 53)}$$

where χ, is the degree of crystallinity, W_f =0.55 is the global weight fraction of the reinforcement in the organosheet, ΔH_m is the crystallization enthalpy of the organosheet, and ΔH_{100} (135 J/g) is the melting enthalpy of 100 % crystalline PA6 [104]. Cooling during crystallization process influences the degree of crystallinity and composition of crystal structure in nylon [105]. DSC profiles of pure nylon and organosheet were compared and showed similar peak melting temperatures, 219.67C for nylon and 219.14C for organosheet, Figure 17. Furthermore, the

endothermic behavior, which is indicative of crystalline phase composition due to processing, showed similar profile for nylon and organosheet.

The average measured crystallization enthalpy of the organosheet for two samples was 29.2 J/g, and for pure PA6 was 72 J/g. The results show the average degree of crystallinity of 0.48 in the organosheet which is close to that of the pure PA6 (0.53). Therefore, mechanical properties of pure PA6, which was tested in the subsequent section, were used to derive the effective properties of the glass fiber-PA6 bundles and to represent the mechanical behavior of PA6 rich pockets in the organosheet.

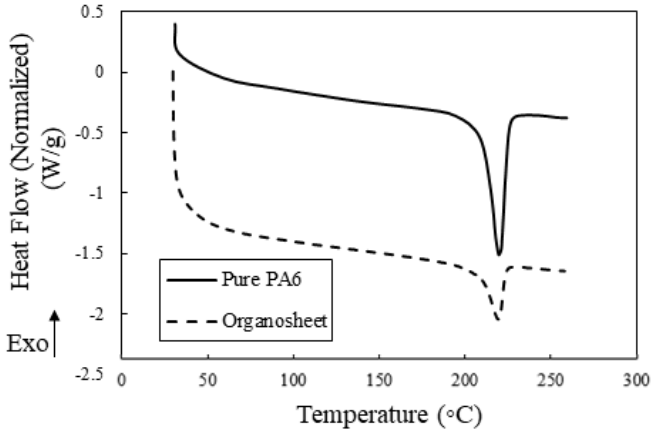

Figure 17 DSC melting behavior for pure PA6 and organosheet

4.2 Mechanical behavior of PA6

The standard tensile test method, ASTM D638-16 Type1, was used to measure the mechanical properties of the PA6 and define the elastic-plastic behavior of the material. The DIC system was used to measure the strain on the surface of the sample during the experiment. The

results show high ductile capability in pure PA6 material, and the plastic behavior of the material is described by its yield point and post-yield hardening [106].

An elastic-plastic finite element model was developed for PA6 tensile test with continuum ductile damage mechanism to calibrate the material model from the test data. The plasticity of the material was defined through the true yield stress as a function of true plastic strain, measured from tensile test. Figure 18-a shows the strain pattern on the sample at the maximum stress, where the strain distribution shows uniform strain distribution across the gauge length. Figure 18-b-c shows the pattern of the damage variable and equivalent plastic strain in the PA6 tensile model, respectively, at the maximum stress, where the higher damage variable and plastic strain occur in the middle of the specimen. Figure 18-d shows close correlation between the true stress-strain behavior from tensile testing compared with the modeling prediction. The mean and standard deviation for tensile modulus and true maximum stress from the test results were 1.85±0.06 GPa and 87±4.5 MPa, respectively. The correlation between the transverse and longitudinal tensile strain showed the Poisson's ratio of 0.43. The elasto-plastic and damage properties were obtained by calibration of the constitutive model described in 2.1.3 using experimental tensile testing of neat PA6 and are shown in Table 3. There properties were subsequently used for modeling the chanical behavior of PA6 rich pockets in the organosheet model. Furthermore, the neat PA6 properties were used as inputs in calculating engineering constants for the homogenized properties of bundles and the corresponding principal strengths, as shown in Appendix A.

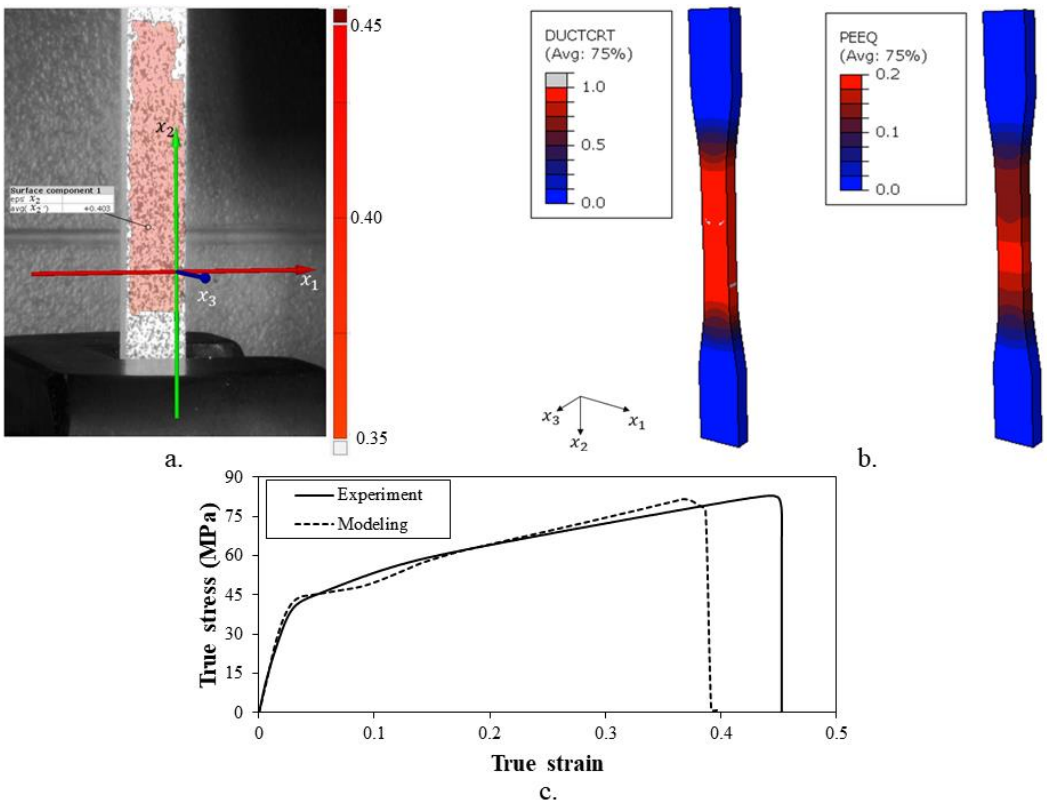

Figure 18 (a) DIC image for PA6 tensile testing at maximum stress (b) Equivalent plastic strain and (c) damage variable in PA6 tensile modeling at maximum stress (d) True stress strain curve of PA6 tensile test compared with modeling

Table 3 Material's constants used for finite element modeling of neat PA6 and matrix pockets in organosheet

Property	Value
Yield stress (MPa), σ_Y^m	30
Ultimate trues stress (MPa), σ_u^m	87
Young's modulus (GPa), E^m	1.85
Poisson ratio, ν_m	0.43
Fracture plastic strain, $\bar{\varepsilon}_f^{pl}$	0.48
Stress triaxiality, η	0.33
Displacement at failure (mm), $\bar{u}_f^{pl}$	0.14

4.3 Characterization of bundle mesostructure and effective mechanical properties

The fiber orientations within a bundle were calculated by using (Equation 34). Figure 19-a shows a selected bundle containing 191 individual fibers with the average fiber orientation distribution of 61° (Figure 19-b). The overall bundle orientation was calculated by taking the average over the calculated fibers orientation in the bundle using (Equation 38) (3.1.2). Figure 19-c shows that the bundle orientation distribution from organosheet micrograph varied between 20°-75°. Over half of all the bundles were oriented in the range of 25° - 45° and the overall average angle of the bundles was 41°. The global, bundle orientation components, fiber volume fraction, fiber volume fraction within the bundles, and the bundle volume fraction in organosheet were measured using the microscopy analysis, as discussed in Section 3.1.2, and results are presented in Table 4.

The orientation state of the organosheet on the meso-scale was generated based on the measured bundle orientation tensor, calculated by (Equation 39). The first component of the bundle orientation tensor (a_{11}) is representative the bundle degree of alignments in x_1 direction. The measurement of a_{11} in different regions of the organosheet shows the average and standard deviation of 0.54 ± 0.03. The average of the other components of bundle orientation tensor, a_{22} and a_{12}, are indicated in Table 4. The major and minor diagonal of the bundles were measured by the ellipse fitting on the cross-section of the bundles within the micrograph of an organosheet. The mean and standard deviation of major and minor diagonals were measured as 786±228µm (coefficient of variance: 29.08) and 76±12µm, respectively. Table 4 shows the characterized microstructural characteristics of the fiber volume content and bundle geometry within the organosheet measured by microstructural image processing on the 2-D cross-section micrograph.

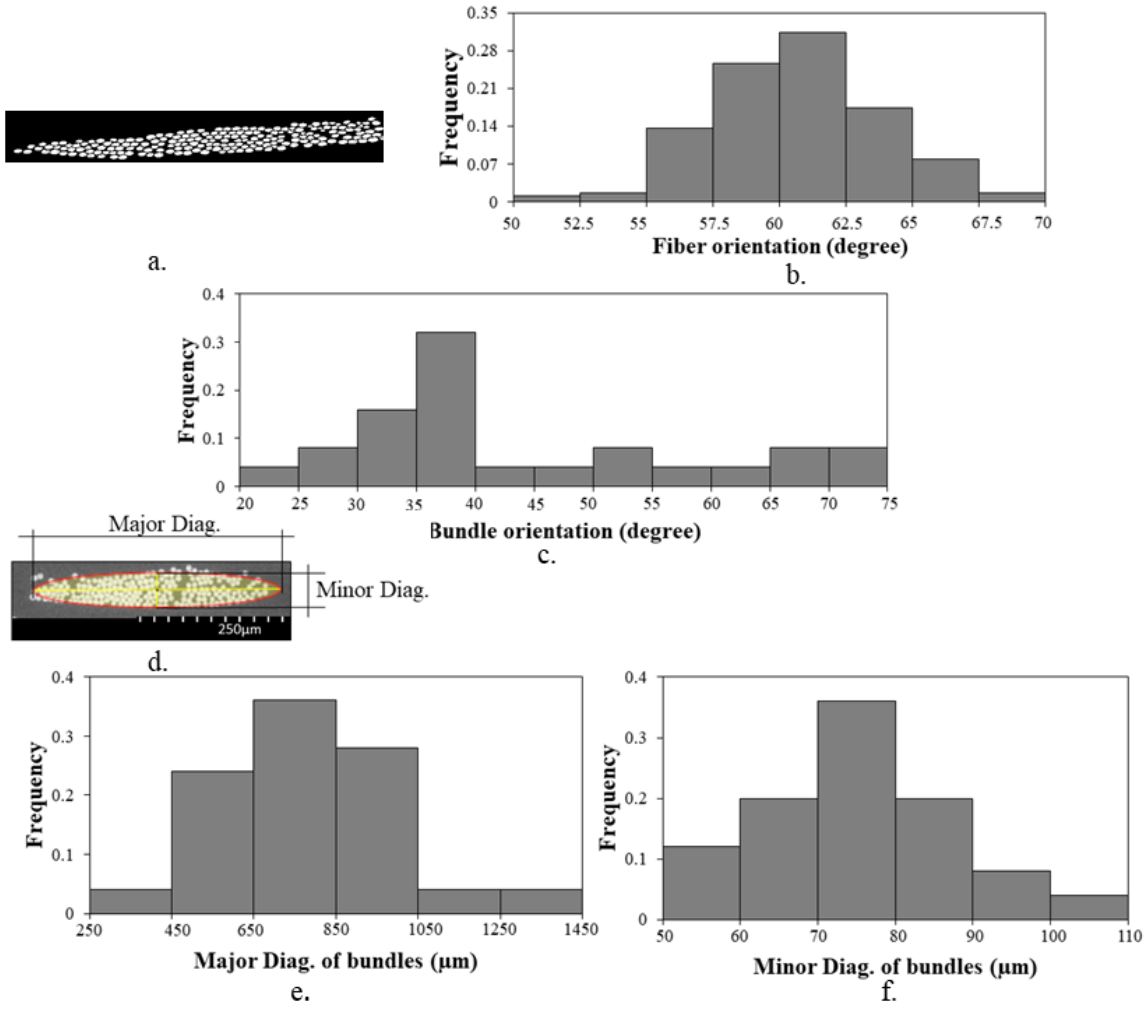

Figure 19 (a) Cropped binary image of the identified bundle (b) Distribution of fiber orientations in a selected bundle (c) Distribution of bundle orientations (d) A schematic of ellipse fitting on a bundle (e) Distribution of the bundle major diagonals (f) Distribution of the bundle minor diagonals

Table 4 Measured micro- and mesostructural characteristics of organosheet

Property	*Value*
Global FVF	0.34
FVF in bundles (Ave.±Std Dev.)	0.68±0.03
Bundle volume fraction	0.55
a_{11} (Ave.±Std Dev.)	0.54±0.03
a_{22} (Ave.±Std Dev.)	0.46±0.03
a_{12} (Ave.±Std Dev.)	0.39±0.01
Major diagonal of bundles (Ave.±Std Dev.)	786±228μm
Minor diagonal of bundles (Ave.±Std Dev.)	76±12μm

Based on the measured micro- and meso-scale parameters of the organosheet, the following morphologies of the virtual organosheet models were generated with the a_{11} of 0.54, 0.58, and 0.62 to study the effect of the bundle orientation on the mechanical properties of the material. Since the finite element voxel thickness was 40 μm, it resulted on average between 2-3 elements through the thickness of each bundle. To further estimate the average bundle thickness generated in the organosheet, the cross-section of the simulated morphology (Figure 4-a) was used to measure the average and standard deviation of the bundle thickness, which was found to be $89 \pm 20\mu m$ and close to the average of the measured minor diagonal of the bundles in organosheet. For every global bundle alignment, three different sample configurations were generated and analyzed using tensile and three-point bending simulations. Table 5 shows the calculated effective material properties of the bundles based on the measured 68% FVF in the bundles (Table 4). The corresponding principal moduli and strengths were calculated using micro-mechanical model (see Appendix A) using the elasto-plastic matrix behavior. The calculated homogenized properties of the bundles were used to represent the organosheet on the meso-scale.

Table 5 Homogenized stiffness and strength properties for bundles

Material property	Numerical value
Longitudinal modulus, $\boldsymbol{E_{11}(MPa)}$	59234
Transverse modulus, $\boldsymbol{E_{22}}$, $\boldsymbol{E_{33}(MPa)}$	9571
Shear modulus, $\boldsymbol{G_{12}}$, $\boldsymbol{G_{13}(MPa)}$	3002
Shear modulus, $\boldsymbol{G_{23}(MPa)}$	3300
Poisson's ratios,$\boldsymbol{\nu_{12}}$, $\boldsymbol{\nu_{13}}$	0.29
Poisson's ratios,$\boldsymbol{\nu_{23}}$	0.45
Longitudinal tensile strength,$\boldsymbol{F_{11}^{t}(MPa)}$	1967
Longitudinal compressive strength,$\boldsymbol{F_{11}^{c}(MPa)}$	800
Transverse tensile strength,$\boldsymbol{F_{22}^{t}(MPa)}$	145
Transverse compressive strength,$\boldsymbol{F_{22}^{c}}$($\boldsymbol{(MPa)}$	145
Peel strength,$\boldsymbol{F_{3z}(MPa)}$	145
Transverse shear strength,$\boldsymbol{F_{Sz}}$ $\boldsymbol{(MPa)}$	146

5 EFFECT OF THE FIBER BUNDLE ORIENTATION AND SPECIMEN SIZE ON THE MECHANICAL BEHAVIOR OF LDFC

Modeling of the organosheet at the meso-scale level allows simulating the effective mechanical response and failure behavior of the material. The effect of the bundle degree of alignment in the organosheet on the tensile and flexural strength and modulus of the material were studied. Furthermore, the impact of the span length on the flexural response and failure behavior were analyzed.

5.1 Comparison of experimental and numerical modeling prediction

The effective tensile and flexural modulus and strength of the organosheet were measured through the experiments and compared with the simulation results. Figure 20 shows the comparison between the stress-strain response from the tensile and three-point bending tests with the simulation results. The initial linear global response of the stress-strain behavior in the RVE-based tensile and three-point bending simulations agreed closely with the experimental results. The progressive failure, non-linear, behavior in tensile simulation did not have the same brittle-like behavior observed in the experiments, while the strength value was in the experimentally observed range. The flexural simulation and experimental results showed similar gradual decrease once maximum stress was reached.

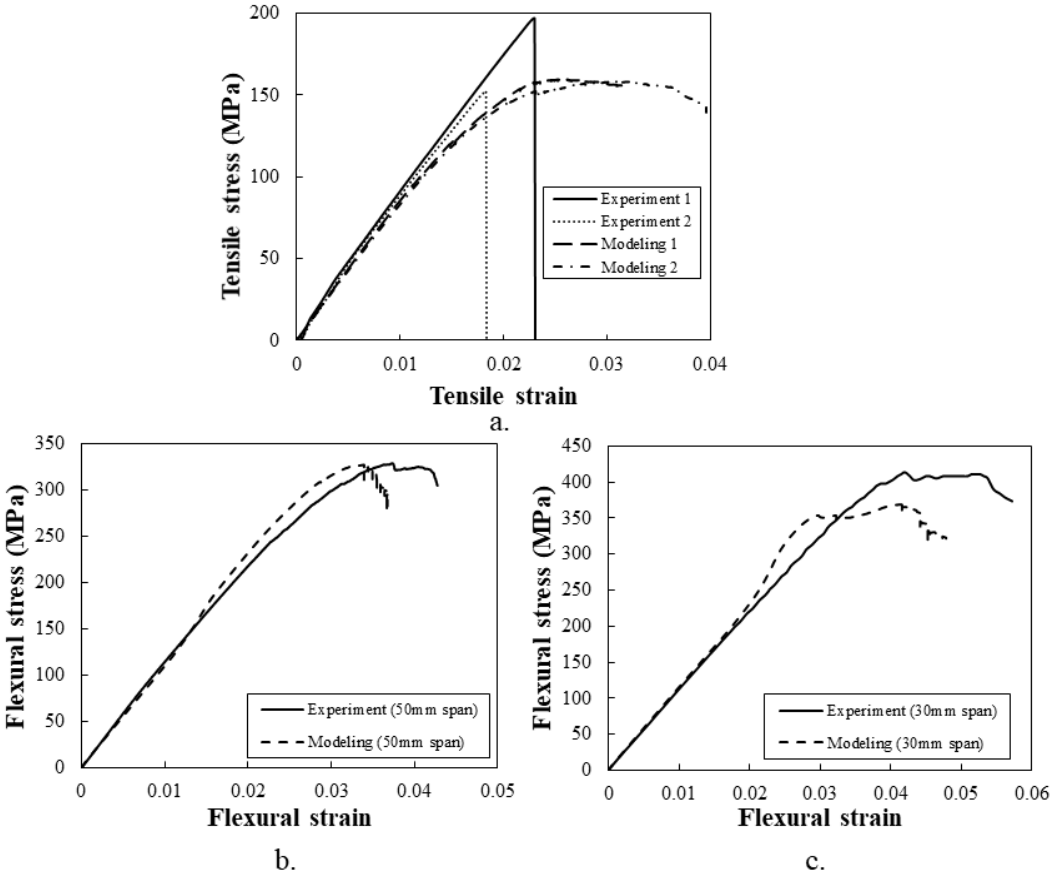

Figure 20 (a) Tensile stress strain behavior of the experiment and RVE modeling (b) Flexural stress strain behavior of the experiment and modeling with 50mm span, and (c) 30mm span

Figure 21 a and b show the range of the modulus and strength from experiments compared with RVE simulation results for tensile loading. The variation of the effective tensile modulus and strength results from the variability of the local structural orientation of the bundles due to the discontinuous fiber reinforcement morphology. The tensile modulus and strength from RVE modeling agreed closely with experiment results. The average tensile modulus and strength from the simulations for the morphology with the average a_{11} of 0.54 was 8.9±0.65GPa and 158.4±0.3MPa, respectively. With increased alignment, the average tensile modulus and strength improved from 9.1±0.15GPa to 9.9±0.11GPa and from 157.3±12.5 MPa to 167.7±3.4 MPa,

respectively, for the increased a_{11} from 0.58 to 0.62. Figure 21-c and d show the flexural modulus and strength variation with respect to span-to-thickness ratio from experiment and modeling results. The flexural modulus from modeling results for the morphology with the average a_{11} of 0.54 and 0.58 agreed with the test results of three-point bending with a span ratio of 11 to 26. The modeling results show that the increased a_{11} from 0.58 to 0.62 leads to improvement of 12% and 14% of the overall flexural modulus and strength, respectively. The initial increase of the average flexural modulus by increasing the span ratio can be related to the effect of shear deformation in anisotropic long fiber composites in case of the shorter beam. The experimental results demonstrated a more pronounced effect in the increase of the flexural modulus with span, than in the simulation. This initial increase of the modulus with span is similar to the behavior observed in continuous fiber composites, which is governed by the diminishing role of the intralaminar shear deformation in the laminates [107]. A similar effect develops in the composites as span increased up to the double nominal fiber length (about 2" span for 1" nominal fiber length). With the span-to-thickness ratio increasing above 25, the modulus showed the gradual decrease to a plateau-like behavior. The drop in the flexural modulus is explained by the discontinuous fiber morphology governed by the fiber orientation state, which is described with orientation tensor.

The average flexural strength showed a gradual decrease and plateau like behavior from 408MPa to 389MPa (from experiments) by increasing the span ratio from 8 to 11, following the decline to 202 MPa by increasing the span ratio to 26. The flexural strength from the modeling predictions was in the range of the experimental values for the aspect ratio of 8 to 18 and followed a moderate decline to reach a plateau-like behavior at the span ratio exceeding 18, which was not as pronounced as in the experimental results. The decline of flexural strength is explained in the next section by the combination of the various damage modes present in the organosheet.

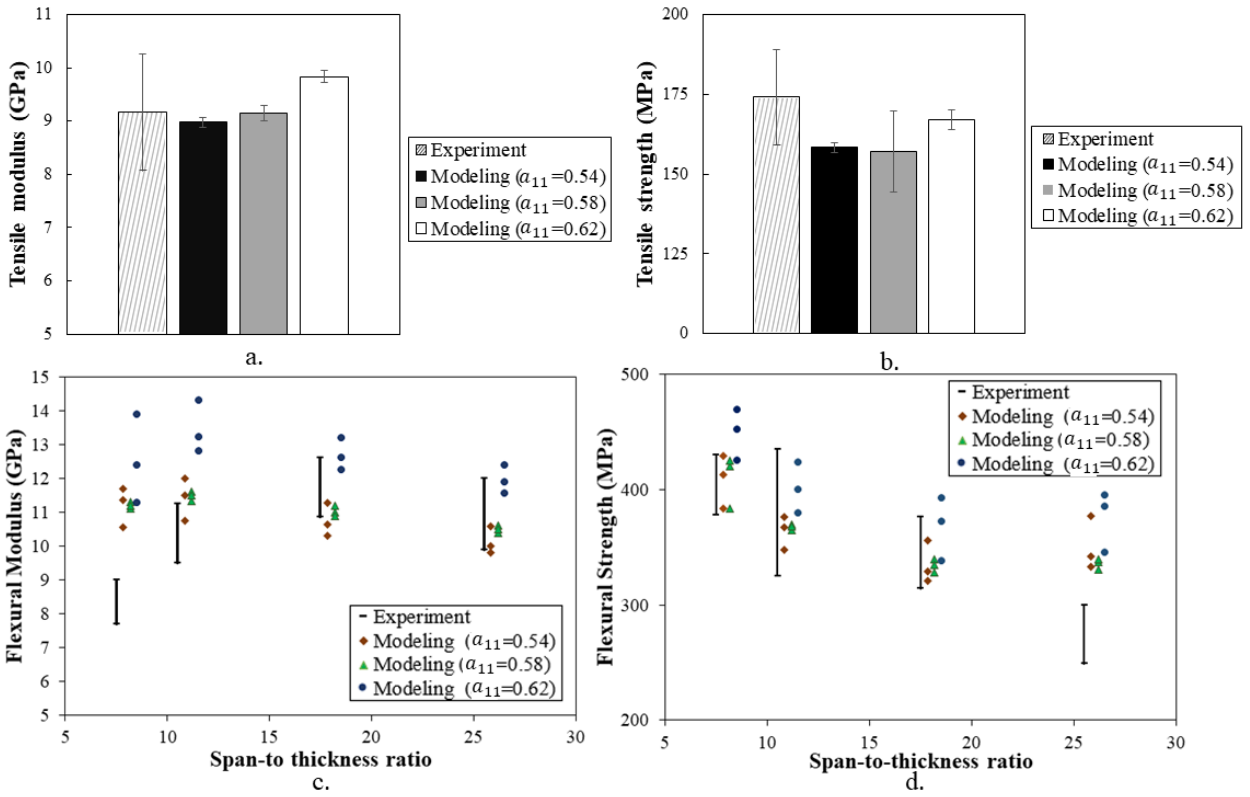

Figure 21 Comparison of experiment and modeling results of (a) tensile modulus and (b) tensile strength (c) flexural modulus and (d) flexural strength

5.2 Analysis of damage states in organosheet under tensile and three-point loading

Failure in the organosheet is the result of the evolution and interactions of the various damage events including fiber/matrix failure, bundle delamination, matrix failure and cracking in PA6 pockets (Figure 22). Consequently, the damage behavior in organosheet is dispersed throughout the volume of composite and is characterized by the simultaneous damage onset and propagation at various locations. This behavior is due to complex hierarchical mesostructure, which promotes multiple origins of failure due intrinsic structural redundancy and ability for load redistribution within the material once one of the failure modes develops. To predict the evolution

of the complex damage behavior in organosheet the continuum damage mechanics was employed as discussed in 2.1.

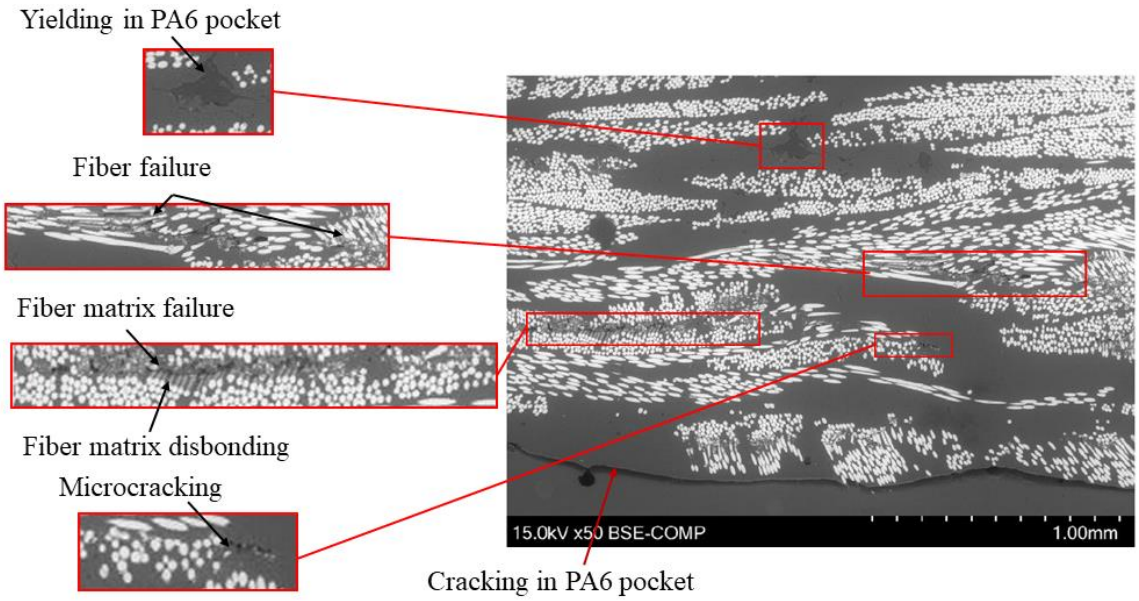

Figure 22 Characteristics of the fractured organosheet under three-point loading

Figure 23-26 shows the cumulative relative frequency of the damage variables. The patterns of the damage index in the fiber direction, transverse to the fiber direction, and through the thickness of the bundles are shown at the maximum stress for RVE-based tensile and three-point bending simulations with varying span lengths. For 3-point bending simulations, the cumulative relative frequency of damage variables (Figure 23) was calculated in damage process zone (DMZ) by considering the damaged elements as a fraction of total number of the elements. The damage was confined to the region of 7.5 mm around the top roller for all simulations, which was identified as the DPZ (Figure 23). To determine the cumulative relative frequency of damage modes in RVE-based tensile simulation (Figure 24) the entire volume of RVE was used. Therefore,

the cumulative distribution provides a measurement of the damaged elements volume fraction and was used to compare the different failure modes in tensile and 3-point bending simulations.

The cumulative relative frequency of fiber damage variable in tensile simulation showed higher volume fraction (2.9%) compared to the 3-point bending modeling (in the range of 0.5% and 0.65%). Under tensile loading, the damage variable transverse to the fiber direction occurred in a larger zone compared with the fiber damage. Increasing the span from 20mm to 70mm lead to an increase in the matrix damage variable in bundles from 13% to 27%, while the RVE-based tensile modeling showed the higher value (81%). Taken together, these results indicate that the predicted decrease in 3-point bending strength with the span-to-thickness ratio from 8 to 25, including lower values for tensile strength, followed the trend of increased matrix damage, as the average strength decreased from 450 MPa to 375MPa in 3-point bending for the morphology with the a_{11} of 0.62.

The cumulative relative frequency of the damage variable through the thickness (Figure 25) corresponds to the bundle delamination also shows the higher volume fraction in RVE tensile simulation (6.1%) compared to the 3-point bending simulations (in the range of 0.5% and 1%).

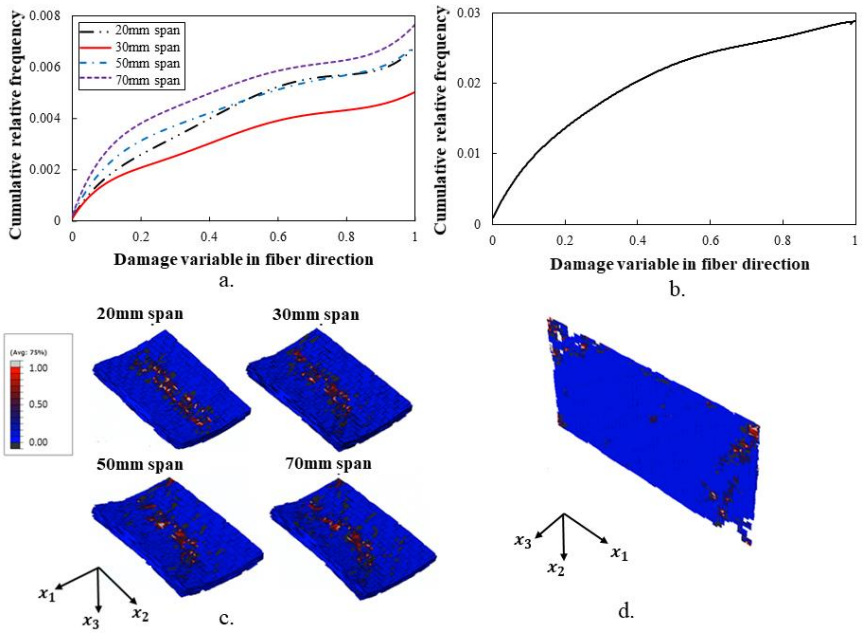

Figure 23 Cumulative frequency of the damage variable in the fiber direction in three-point bending at DPZ and (b) RVE tensile simulations (c) Pattern of the damage variable in three-point bending at DPZ and (d) RVE tensile simulations

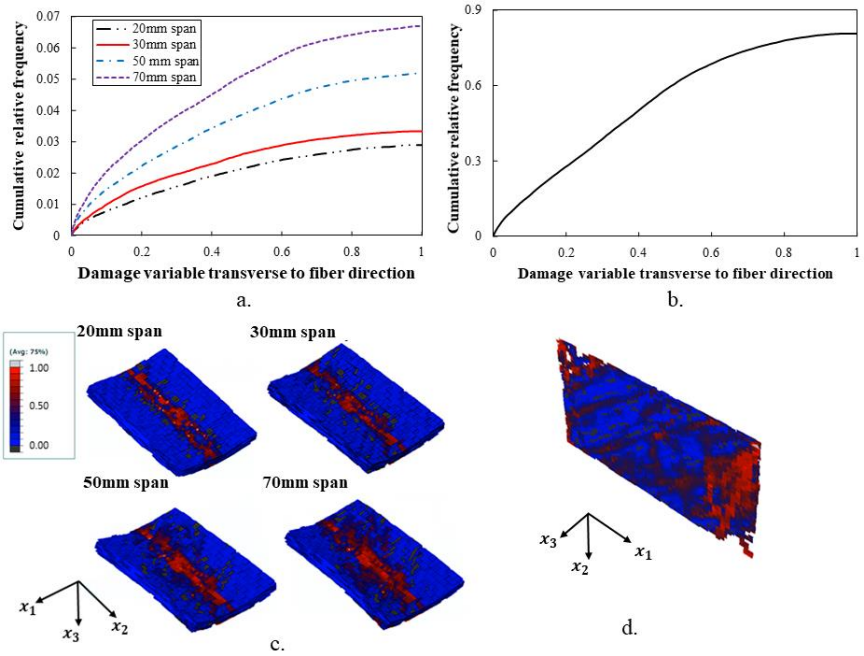

Figure 24 (a) Cumulative frequency of the damage variable transverse to the fiber direction in three-point bending at DPZ and (b) RVE tensile simulations (c) Pattern of the damage variable in three-point bending at DPZ and (d) RVE tensile simulations

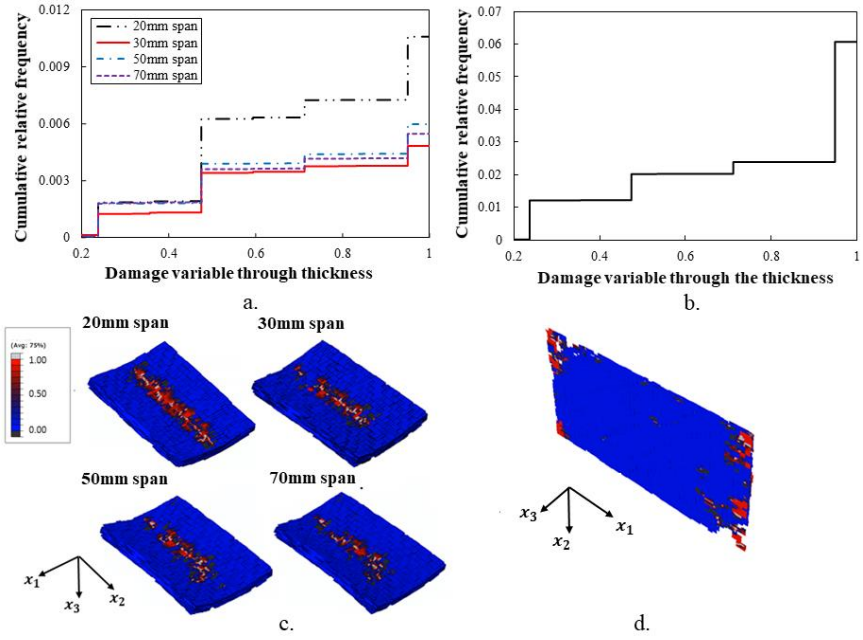

Figure 25 (a) Cumulative frequency of the damage variable through the thickness in three-point bending at DPZ and (b) RVE tensile simulations (c) Pattern of the damage variable in three-point bending at DPZ and (d) RVE simulations

Figure 26-28 show the cumulative relative frequency and the pattern of the damage variable and plasticity in the PA6 pockets at the maximum stress for flexural simulations and RVE tensile modeling. Increasing the span from 20mm to 70mm lead to an increase in the volume fraction of damaged elements in the PA6 pockets from 13% to 27%. The maximum cumulative relative frequency of PA6 pocket damage in RVE tensile simulation was 27%, close to that of 3-point bending with the longer span (70mm). Figure 26 shows the cumulative relative frequency of equivalent plastic strain in PA6 pockets. The volume fraction of elements with developed plastic strain increased from 5.2% to 12.4% by increasing the span length from 20mm to 70mm, as well as the magnitude of the maximum equivalent plastic strain increased from 0.25 to 0.55, respectively. The RVE tensile simulation shows the higher volume fraction of elements with developed equivalent plastic strain in PA6 pockets (44.9%) compared with the 3-point bending

modeling, while the magnitude of maximum equivalent plastic strain is about 0.4. It is important to point out that the level of plastic strain above 0.20 was found to associate with failure in PA6, as shown by the elastic-plastic damage modeling of PA6 (see Figure 18).

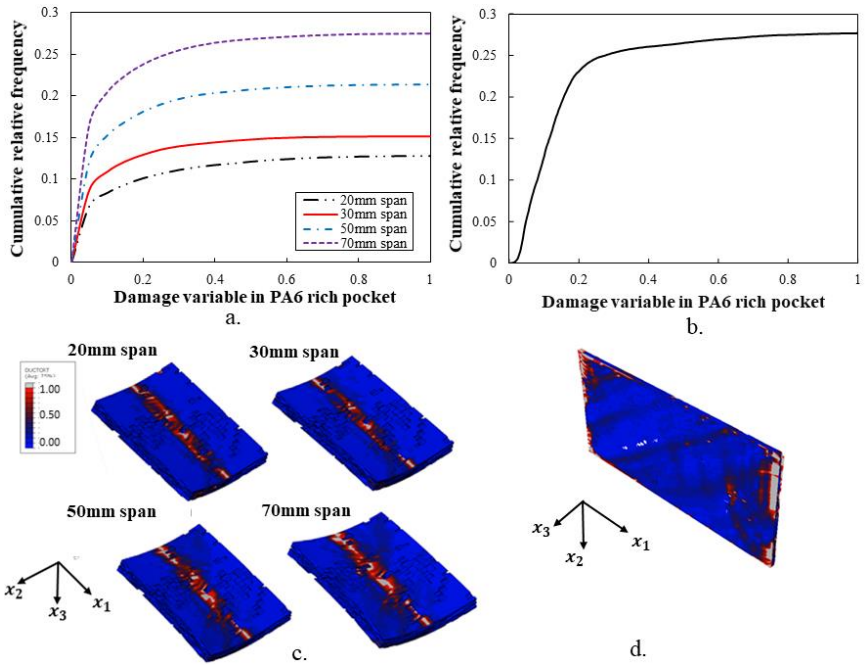

Figure 26 (a) Cumulative frequency of the damage variable in PA6 pockets in three-point bending at DPZ and (b) RVE tensile simulations (c) Pattern of the damage variable in three-point bending at DPZ and (d) RVE tensile simulations

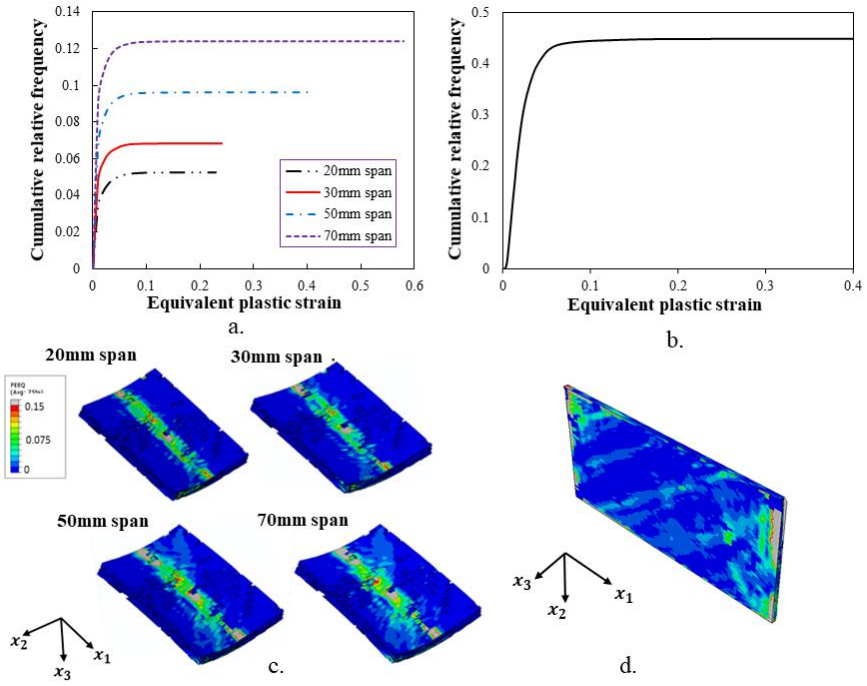

Figure 27 (a) Cumulative frequency of the plastic strain in PA6 pockets in three-point bending at DPZ and (b) RVE tensile simulations (c) Pattern of the plastic strain distribution in three-point bending at DPZ and (d) RVE tensile simulations

6 EFFECT OF NOTCH SENSITIVITY IN LDFC

6.1 Comparison of experiment and modeling prediction

The notched strength of the organosheet were measured through the experiments and compared with the simulation results. Figure 28-a shows a comparison between the stress-strain curves from the tensile tests and the simulation results. The initial linear-elastic response of the stress-strain behavior in the simulations agreed with the experimental results following with the non-linear progressive failure. Figure 28-b shows the range of the notched tensile strength from experiments compared with simulation data. The variation of the notched tensile strength results from the local damage propagation around the notch, reflecting the loss of stress carrying capacity. The average notched tensile strength and corresponding standard deviation of specimens with 2mm hole diameter is 180±13 MPa and in the range of unnotched coupons (172±9 MPa). Heterogeneous mesostructure of organosheet may provide for more critical stress concentration compared to the geometric stress concentration from the notch of 2mm diameter. Therefore, the smaller notch (2mm hole diameter) does not appear to influence the strength. Increasing the notch diameter to 4mm and 6mm leads to a decrease in the average strength to 157±11 MPa and 132±10 MPa, respectively, due to the increased geometric stress concentration that scales with the hole size. The interesting behavior was observed in terms of plateau response of the OHT samples. While unnotched sample exhibited very brittle behavior, it was OHT sample that showed significant amounts of the plastic deformation prior to reaching complete failure. This behavior was observed for all of the hole diameters, and was captured in the modeling of OHT coupons, even though it was more pronounced in the experiments. Such behavior, especially for OHT is desired from the design point of view, as it allows for a more damage tolerant response, by

avoiding the brittle catastrophic failure. The role of plasticity in resin rich pockets was used to explain this behavior, as will be discussed in the results section using PFA simulation results.

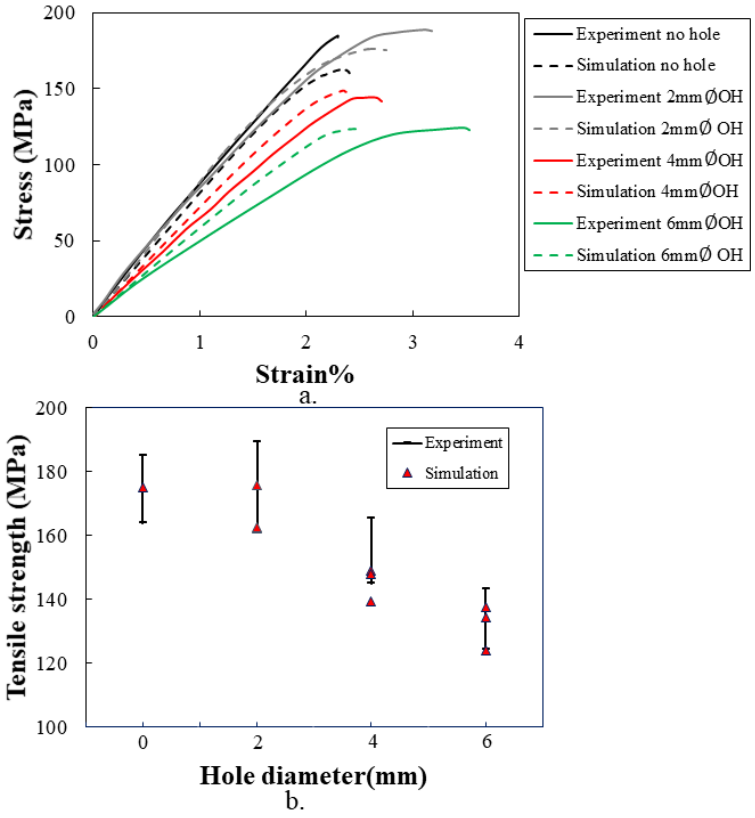

Figure 28 (a) Notched tensile stress strain behavior of the experiments and simulations (b) Comparison of notched strength measured from experiments and simulations

6.2 Analysis of damage behavior in OHT LDFC using experimental and virtual test results

Failure in the organosheet is the result of the propagation and interactions of the complex damage variables including fiber/matrix failure, bundle through thickness failure (e.g. delamination), matrix failure and cracking in PA6 pockets. Failure of the notched specimens was associated with the separation in two pieces by a macro-crack near the hole. Figure 29 shows the

failure mode of fiber failure and PA6 pockets cracking observed around the hole of the failed specimens. Figure 30-a shows the patterns of the in-plane and through thickness damage variables within the bundles and the propagated damage in the PA6 pocket at the maximum stress of OHT simulations. The simulation results showed that the dominant failure modes were the transverse failure in the bundles and the failure in PA6 pockets. Figure 30-b shows the strain distribution pattern on the surface of OHT coupons at the failure captured by the DIC system. The damage sites in organosheet with 2mm OH diameter is dispersed throughout the volume of coupons with localized damage around the notch and alternative damage sites at various locations, which form due to variation in fiber orientation distribution (FOD). The localized strain distribution pattern in loading direction (x_1) was attributed to the damage propagation zone, which shows competing regions of damage process around and away from the notch. The heterogenous morphology of the organosheet promotes the redistribution of stresses over the undamaged regions until the material gradually accumulates enough critical damage to lose the load carrying capacity. As a result of the sample strength with 2mm diameter notches in organosheet did not result in the reduced strength. It is interesting to note, that even though this effect did not result in uncontrolled location of the failure surface: the failure still occurred through the hole of the sample. This result is interesting and was attributed to well controlled FOD throughout the composite and due to small bundle dimensions (about 790µm in width and 76µm in thickness). Furthermore, nylon plasticity is believed to play an important role in this notch insensitive behavior and it will be discussed in the subsequent section based on the simulation results. Increasing the notch diameter to 4mm and 6mm provided for increased geometric stress concentration, which leads to the damage zone located in the vicinity of notch. With increase in the hole diameter (from 2mm to 4 mm and 6mm), the higher local strains are occurring around the region of the hole (Figure 30). The PFA results in Figure 30

illustrate the localization of the damage to the region around the notch as the hole diameter increases.

Figure 31 and 32 shows the strain distribution around the 4mm and 6mm OHT simulation at the linear elastic region and the strain plot on the hole circumference and away of the hole for in-situ and virtual tensile testing. The modeling results follow the similar trend observed experimentally, where the strain concentration reaches maximum values at 0^o and 180^o locations on the hole circumference, and the strain concentration rapidly declines away from the hole.

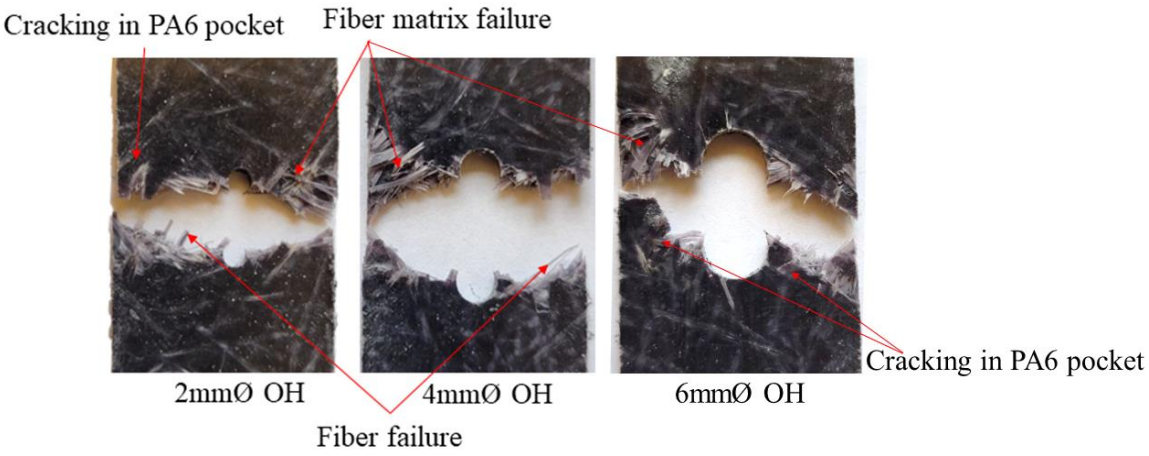

Figure 29 Failed tensile notched coupons

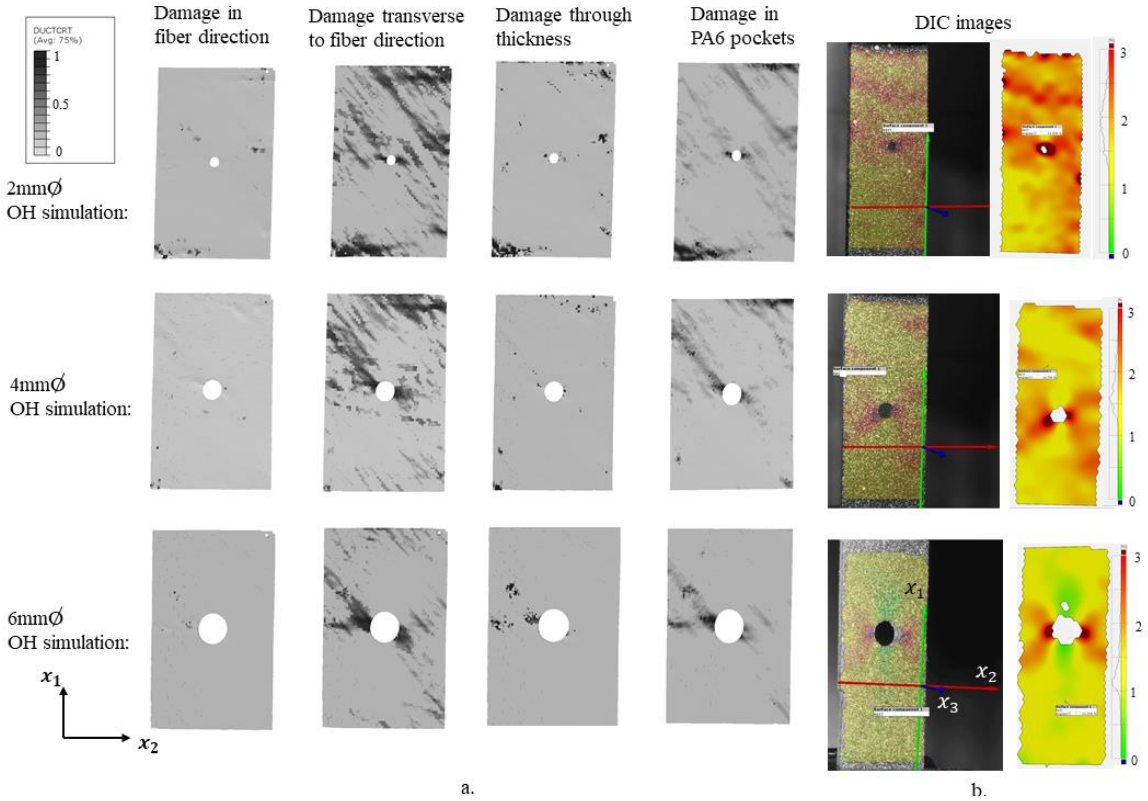

Figure 30 (a) Pattern of the damage variables in OHT simulations (b) Strain distribution pattern of the notched coupons at failure

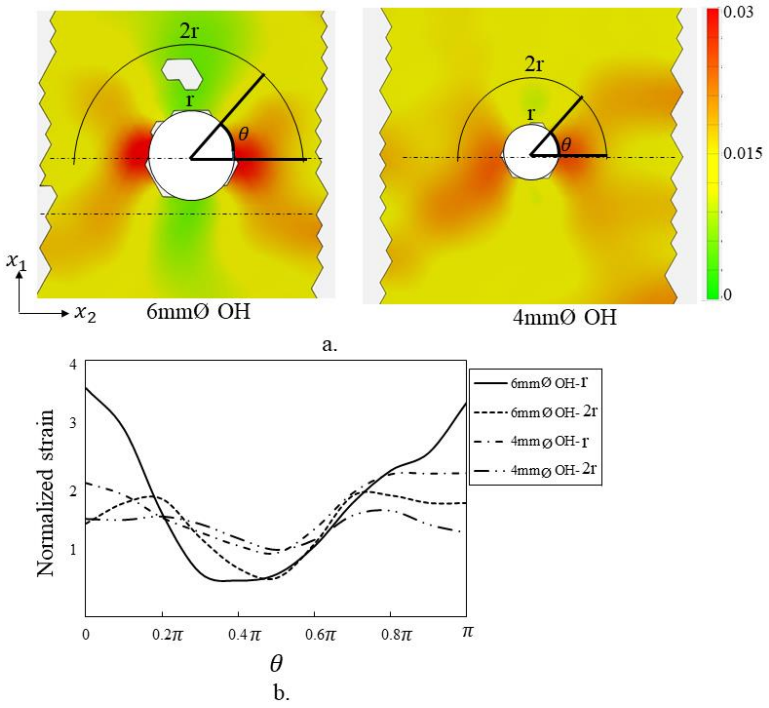

Figure 31 (a) Strain distribution and (b) strain plot along the hole circumference at elastic region for OHT testing

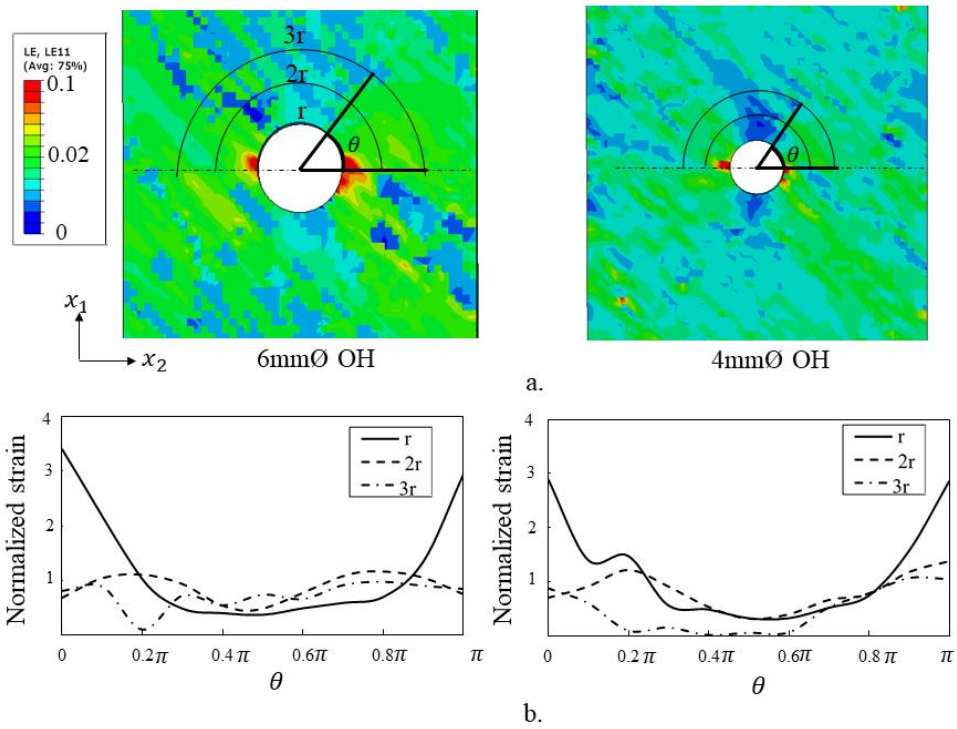

Figure 32 (a) Strain distribution and (b) strain plot along the hole circumference at elastic region for OHT testing

To better understand the completing failure modes, Figure 33 shows the cumulative relative frequency of the damage variables at the maximum stress for OHT simulations. Furthermore, Figure 34 shows the maximum fraction of the damage elements at the failure for the OHT simulations. The cumulative relative frequency of damage variables was calculated through the entire volume of virtual specimen by considering the damaged elements as a fraction of total number of the elements. Therefore, the cumulative distribution provides a measurement of the damaged elements volume fraction and was used to determine what failure modes were most present volumetrically during the virtual test. The maximum cumulative relative frequency of damage variable for 1mm and 2mm hole diameter was at the same level of 95% for PA6 pocket and 42% for transverse to fiber direction damage as the dominant damage modes. Increasing the

notch size from 2mm to 10mm lead to a decrease in the volume fraction of damaged elements of 59% for PA6 pocket and 11% for transverse to fiber direction. OHT simulation with smaller holes shows the higher fraction of the accumulated damage variables (Figure 33 and Figure 34). This implies more arrested damage evolution and redistribution of load paths to undamaged elements during loading of coupons with smaller notches.

Figure 35 show the cumulative relative frequency and the distribution of equivalent plastic strain in the PA6 pockets at the maximum stress for OHT modeling. The volume fraction of elements with developed plastic strain was decreased from 37% to 24% by increasing the hole diameter from 1mm to 10mm, while the maximum equivalent plastic strain was increased from 0.45 to 0.7. Figure 36 shows the fraction of fully damaged elements ($d_i = 1$) with respect to the strain value in 2mm and 6 mm OHT simulations. Increasing the fraction of the damaged elements from the strain of 1.5% to the failure specifically with the higher damage fraction of PA6 can be attributed to the plastic behavior of the material observed in the stress strain curves (Figure 28-a). The simulation results confirm the hypothesis that plasticity was a contributing factor to the notch insensitivity below 2mm hole size, which was observed experimentally, as well as the increased ductility in OHT stress-strain response.

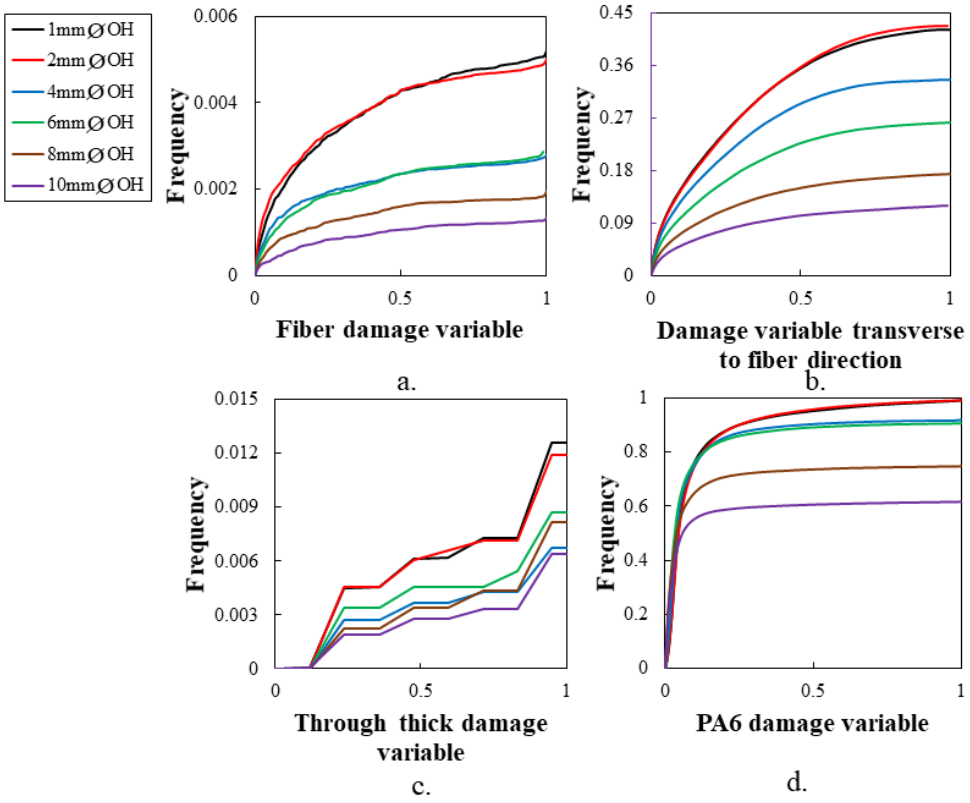

Figure 33 Cumulative frequency of the damage variable (a) in the fiber direction (b) transverse to the fiber direction (c) through the thickness, and (d) in PA6 pockets in OHT simulations

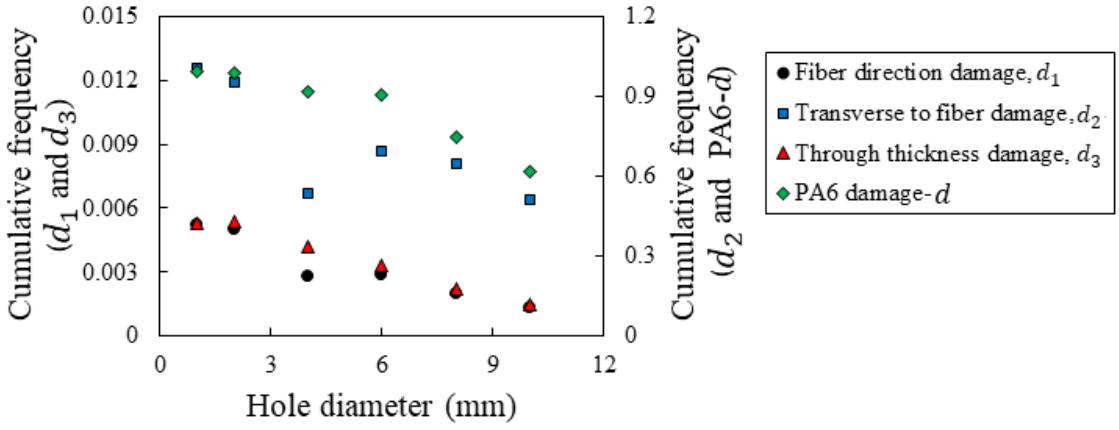

Figure 34 Fraction of the damaged elements at failure

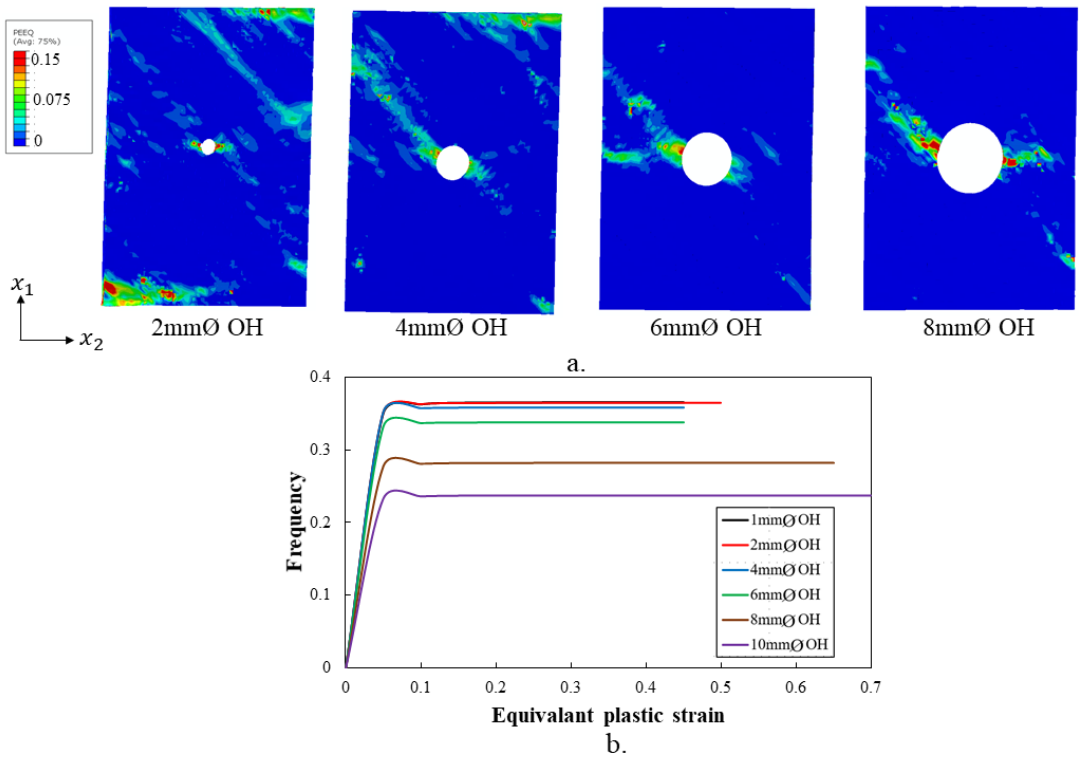

Figure 35 (a) Distribution of the plastic strain in OHT simulations (b) Cumulative frequency of the plastic strain in PA6 pockets OHT simulations

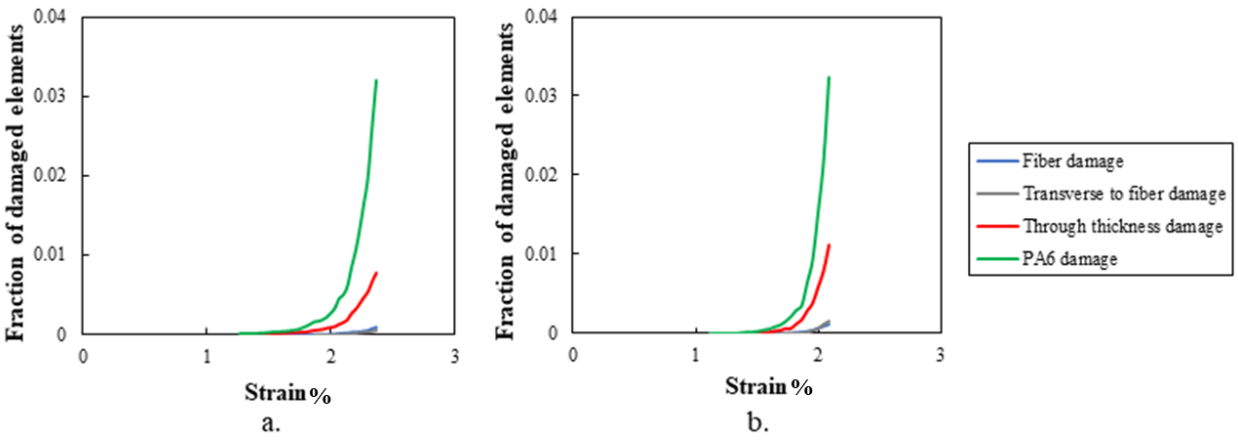

Figure 36 Fraction of the damaged elements with respect to the strain in 2mm (a) and 6mm (b) OHT simulation

6.3 Evaluation of OHT strength using analytical stress based models

To determine the OHT material response, which is independent of the sample width, the notched strength measured from experiments and predicted from PFA simulations were used for the analytical PSC and MPSC models. The finite size correction factor was applied to the strength results using (Equation 46). The correcting factor is defined as the ratio between the stress concentration factor of a finite, K, and the infinite plate, K_∞, which were calculated by (Equation 44), respectively, and are listed in Table 6. The parameter λ was derived from (Equation 42) using Newton-Raphson's method.

shows the corrected notched strength data and corresponding λ values driven through the experiment and simulation results. Parameter *m* and *C* were calculated through the least square method by plotting $-log\ (\frac{1}{\lambda} - 1)$ vs. *log R* according to (Equation 45) (Figure 37-a). Figure 37-b shows the theoretical curve of σ_N/σ_0 based on PSC and MPSC method calibrated through the experiment and simulation results as a function of hole dimeter. The predicted MPSC curves calibrated through the experiment and simulation results were in close agreement and fitted within the range of the OHT strength. This implies that the notched strength for any hole size can be predicted using these analytical models calibrated through the PFA results based on generated virtual digital twin morphologies of OHT organosheet. The results show that σ_N/σ_0 is lower than 0.95 for the specimen with the hole diameter less than 2mm which means the tensile strength is nearly insensitive to this hole size diameter.

Table 6 Stress concentration factor for the finite and the infinite plate of organosheet

Property	**Value**
$\boldsymbol{K_\infty}$	3.49
***K*(*w*/*d*=0.09)**	3.52
***K*(*w*/*d*=0.17)**	3.61
***K*(*w*/*d*=0.27)**	3.80

Table 7 Average unnotched and corrected-notched strength data and the corresponding parameter λ

***R*(mm)**	**Ave. $\boldsymbol{\sigma_N(MPa)}$ (Experiment)**	**$\boldsymbol{\lambda}$ (Experiment)**	**Ave. $\boldsymbol{\sigma_N(MPa)}$ (Simulation)**	**$\boldsymbol{\lambda}$ (Simulation)**
0	168.6 ± 6.4 (σ_0)	-	162.3 (σ_0)	-
1	179.1 ± 11.7	0.13	169.1 ± 9.4	0.13
2	163 ± 11.4	0.24	145.5 ± 5.4	0.34
3	143.5 ± 11.1	0.45	131.9 ± 7.1	0.42
4	-	-	114.8	0.53
5	-	-	98.8	0.60

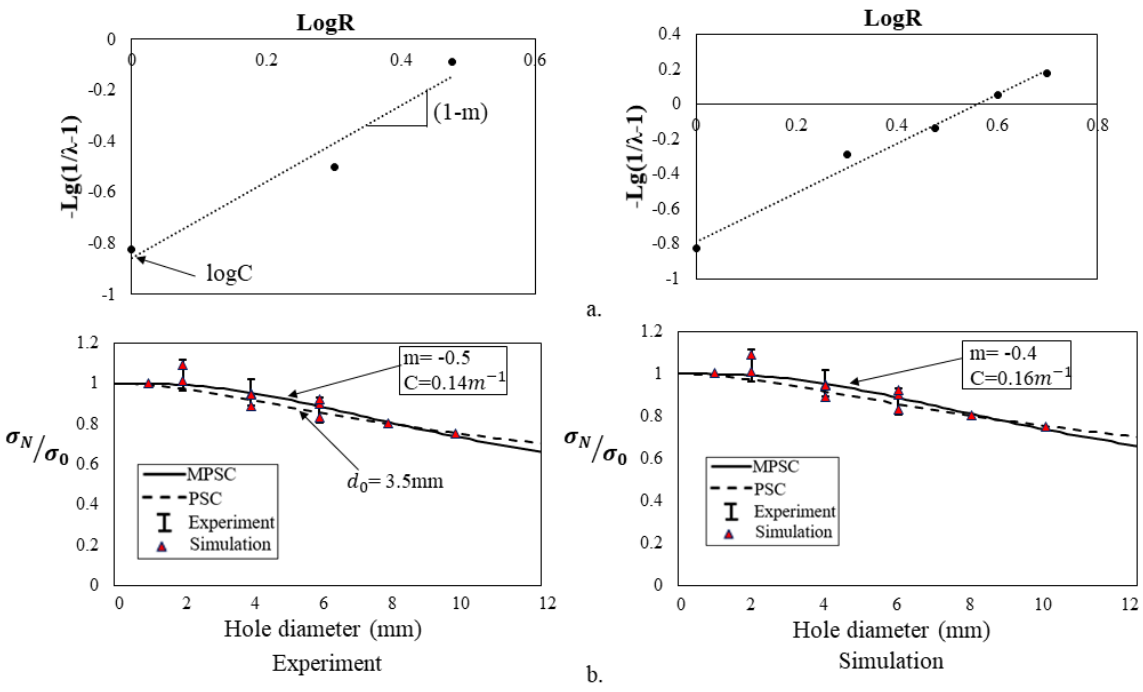

Figure 37 (a) Determination of the parameters m and C (b) MPS and PSC models calibrated through simulation and experimental results compared to the OHT strengths

7 EFFECT OF MOLD FLOW ON THE MECHANICAL PROPERTIES OF LDFC

Figure 38 shows the effect of the mold coverage on the bundle alignment (a_{11}). Fiber bundle orientation was measured through the image microscopy analysis and image processing of the cross-section micrograph of the organosheet. The measured a_{11} for full coverage molded organosheet shows the average of 0.59. Decreasing the mold coverage to 50% results in more aligned bundles ($a_{11} = 0.66$), while 40% mold coverage shows a more random bundle orientation ($a_{11} = 0.58$). This reduced bundle alignment for 40% mold coverage is due to the material overflow for the lower mold coverage. Figure 39 shows the cross-section micrographs of the sample processed through 40% mold coverage at the center of the specimen and away from the center. The center location of 40% mold coverage of the organosheet shows more alignment of the bundles, while the alignment decreases as moving away from the center. The reduced alignment

of the bundles at the edge of the specimen is due to the higher interaction between the flow and mold boundary.

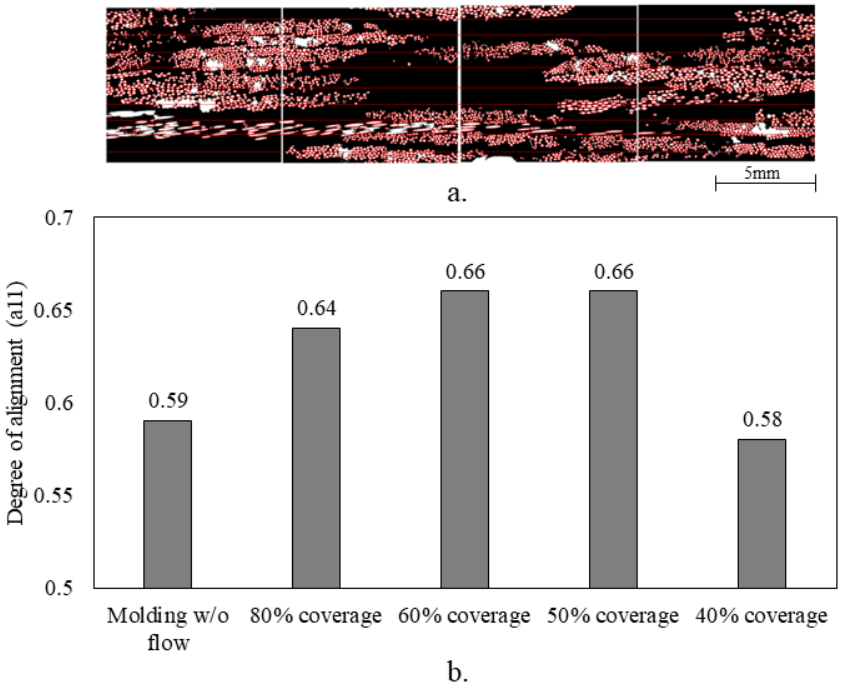

Figure 38 (a) Image analysis for fiber bundle orientation state (b) flow effect on fiber alignment

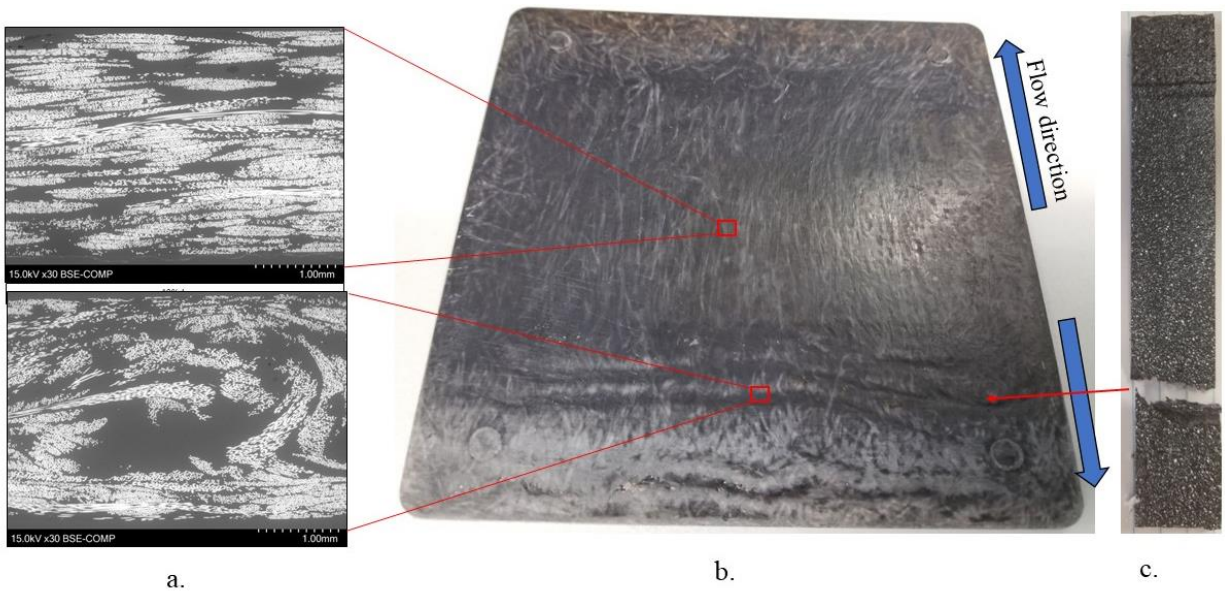

Figure 39 (a) Cross-section micrograph of organosheet and (b) Molded organosheet (40% coverage) (c) failed specimen

Figure 40 shows the effect of the mold coverage on the bundle thickness. Bundle thickness was measured through the image optical microscopy and ellipse fitting method on the bundles of the cross-section micrograph of the organosheet (Figure 40). The average bundle thickness of the full coverage molded organosheet is 73µm and decreasing the mold coverage to 40% results in the reduced bundle thickness of 0.0063 µm. The flow in a partially mold coverage leads to the elongation of the fiber bundles during molding and reduced thickness of the bundles. Figure 41 shows the measured tensile modulus and strength from the specimen processed by full and partial mold coverage. The average tensile modules gradually increase from 9.6GPa to 14.9GPa for the specimens by full mold coverage and 50% coverage mold, respectively, followed by a gentle decrease to 13.9GPa for the 40% mold coverage. The average tensile strength shows an increasing trend from 162MPa to 254MPa for the full and 60% mold coverage, followed by a moderate decrease to 210 MPa for 50% mold coverage and a sharp drop to 70MPa for 40% mold coverage. Increasing the modulus and strength for the partial coverage of mold to 60% is due to the increased

global fiber bundle alignment in the direction of the flow as well as the reduced bundle aspect ratio (bundle length to thickness) because of the fiber bundle elongation. Increased tensile strength and modulus for the partial coverage molded organosheet can also result from the orientation development that occurred in Nylon 6 phase due to the flow effect during molding. The drawing of Nylon 6 under the elevated temperature improves the mechanical properties due to the reduction of amorphous fraction in the material and the increased crystallinity [108].

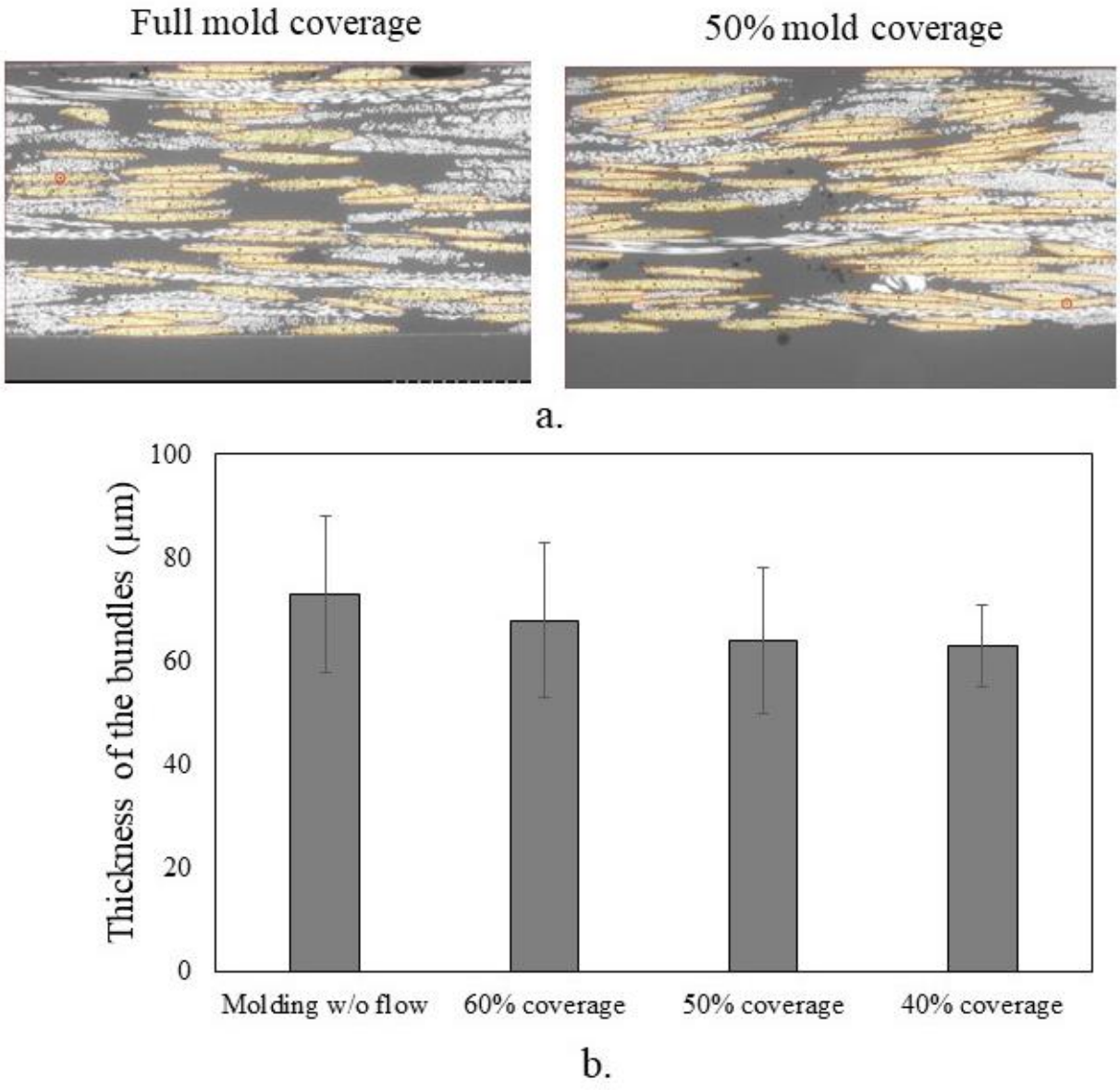

Figure 40 (a) Image analysis to measure bundle thickness (b) Mold flow effect on bundle thickness

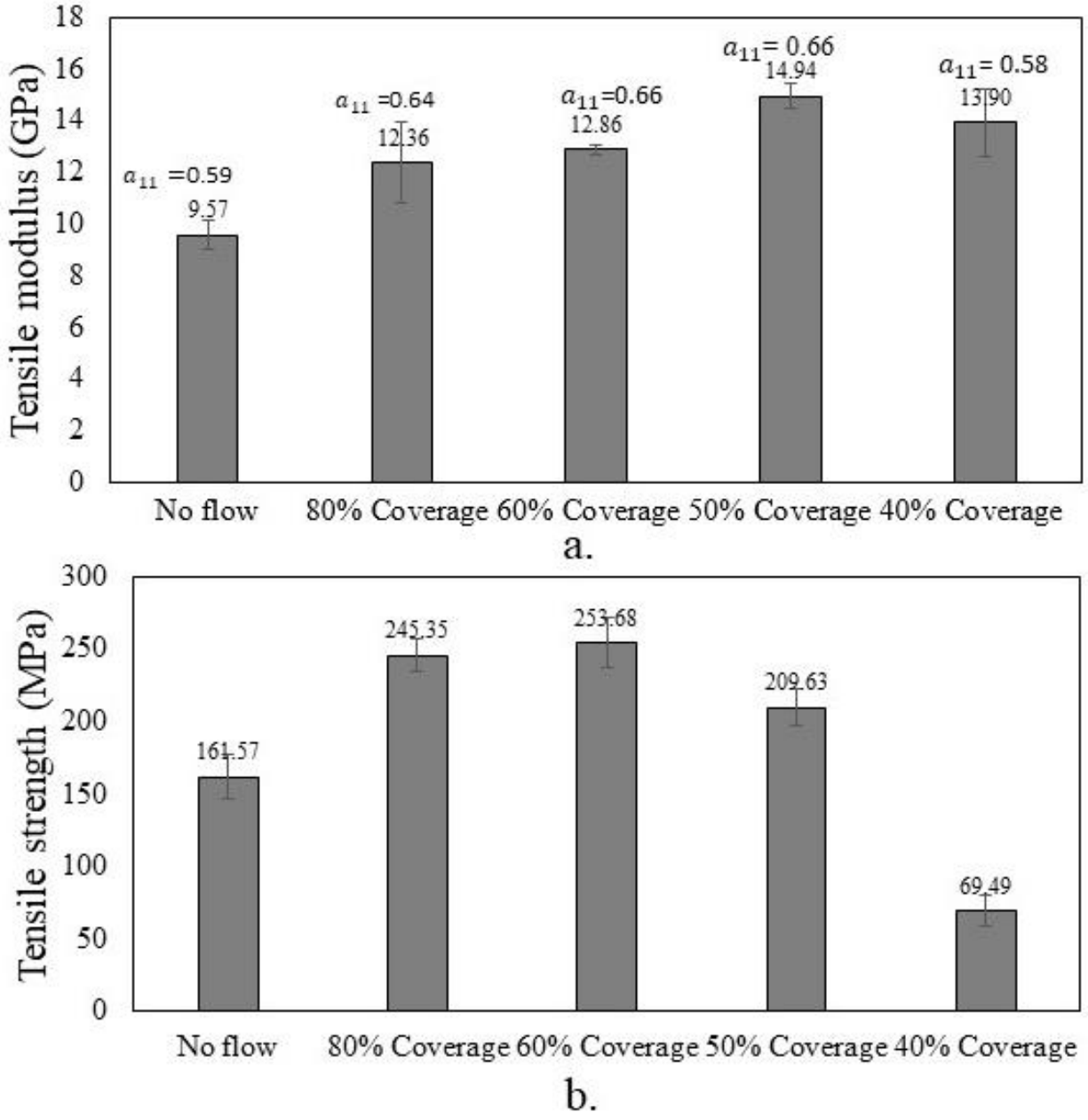

Figure 41 Comparison of tensile modulus and strength of organosheet processed through full and partial mold coverage

8 EFFECT OF PLATELET SIZE ON FLEXURAL BEHAVIOR OF LDFC

8.1 Comparison of experimental and modeling prediction

The effective flexural modulus and strength of the PPMCs were measured through the experiments and compared with the simulation results. Figure 42 shows an example of predicted macroscopic stress–strain curves related to the virtual coupons with prepreg length of 1”, ½”, and ¼” compared to the stress-strain response from the three-point bending tests. The initial linear flexural stress-strain response is followed by initiation of damage and progressive degradation, resulting in non-linear stress-strain behavior before the ultimate strength was reached. A similar gradual decrease of stress was observed in both simulations and experiments after reaching the maximum stress.

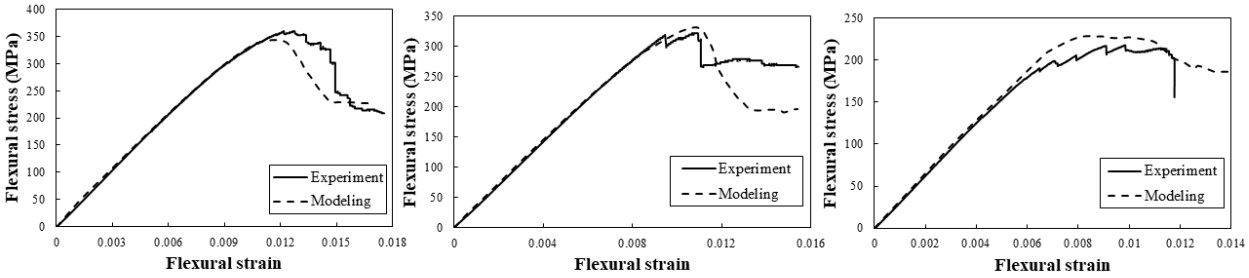

Figure 42 Flexural stress strain behavior of the experiment and modeling of the PPMCs with (a) 1” (b) ½”, and (c) ¼” prepreg platelet length

Platelet length is a key parameter in PPMCs to affect the mechanical properties of the material. Figure 42 summarizes the results of predicted effective flexural modulus and strength of PPMCs with platelet length of 1”, 1/2”, and 1/4" compared with the experiments. As discussed previously, two approaches were considered to generate the virtual PPMC coupons with the 2D

random orientation. Approach 1 generated individual coupons with the full size of specimen, while Approach 2 generated a virtual 5”×5” plaque that was then used to create 5 coupons by partitioning them from the plate (Figure 7). In each approach the assigned global fiber orientation distribution was 2D random. The goal of using two approaches was to understand if the accurate representation of the PPMC mechanical variability is affected by the finite dimensions of the plaque and the sample, when considering the platelet size. Validation of results of two simulation approaches was performed by comparing the experimental and simulation mechanical property distributions by the two-sample *t*-test, wherein the null hypothesis stated that there is no difference between the distributions. The two-sample test is used to determine if the two samples population means are equal at the certain significance level. The difference between the sample distribution is statistically significant if the probability of the phenomenon (*p*-value) is less than 5% [109].

The variation of the flexural modulus and strength, shown in Figure 43, results from the variability of the local structural platelet orientation and the non-symmetric distribution of local material properties. The results indicate that PPMCs with longer platelet length (1”) shows similar flexural strength and modulus compared with PPMCs of ½” prepreg platelet length. Experimental flexural strength and modulus was even marginally higher by 9.5% and 16% respectively, when comparing 1” PPMC and ½” PPMC samples. Fewer number of platelets in a 1” PPMC specimen leads to a more non-uniform local platelet orientation when compared to ½” PPMC that results in the same level of effective flexural modulus and strength, even through the aspect ratio is doubled in 1” PPMC samples. The analysis of FOD variation is presented in the following section. Further reducing the platelet length from 1/2” to ¼” in PPMCs results in significantly decreasing the flexural modulus and strength by 38% and 23%, respectively, due to the reduced stress sharing between platelets. This result shows that both platelet aspect ratio (ratio between length and

thickness) and non-uniformity in fiber orientation distribution (FOD) are affecting the effective flexural mechanical behavior. The simulation results agreed with the test results and showed a decreasing trend of average flexural strength and modulus with reducing the platelet length from 1” to ¼”.

A statistical analysis was performed to analyze the effect of modeling approach to generate virtual PPMC morphology (Approach 1 and 2 as introduced previously). The *p*-value of the two-sample *t*-test between the predicted flexural strength and modulus obtained from simulations and the flexural strength and modulus measured from the experiments are greater than 0.05. Therefore, the null hypothesis was not rejected, and two sample distributions are not significantly different at 95% confidence interval, implying that the simulation results for both approaches can be considered reliable. This result indicates that to predict flexural behavior of thin 2D random PPMCs plates (2-3 mm plate thickness and 15-20 platelets through the thickness) it is possible to generate individual coupons, as well as use random distribution to create individual PPMC samples.

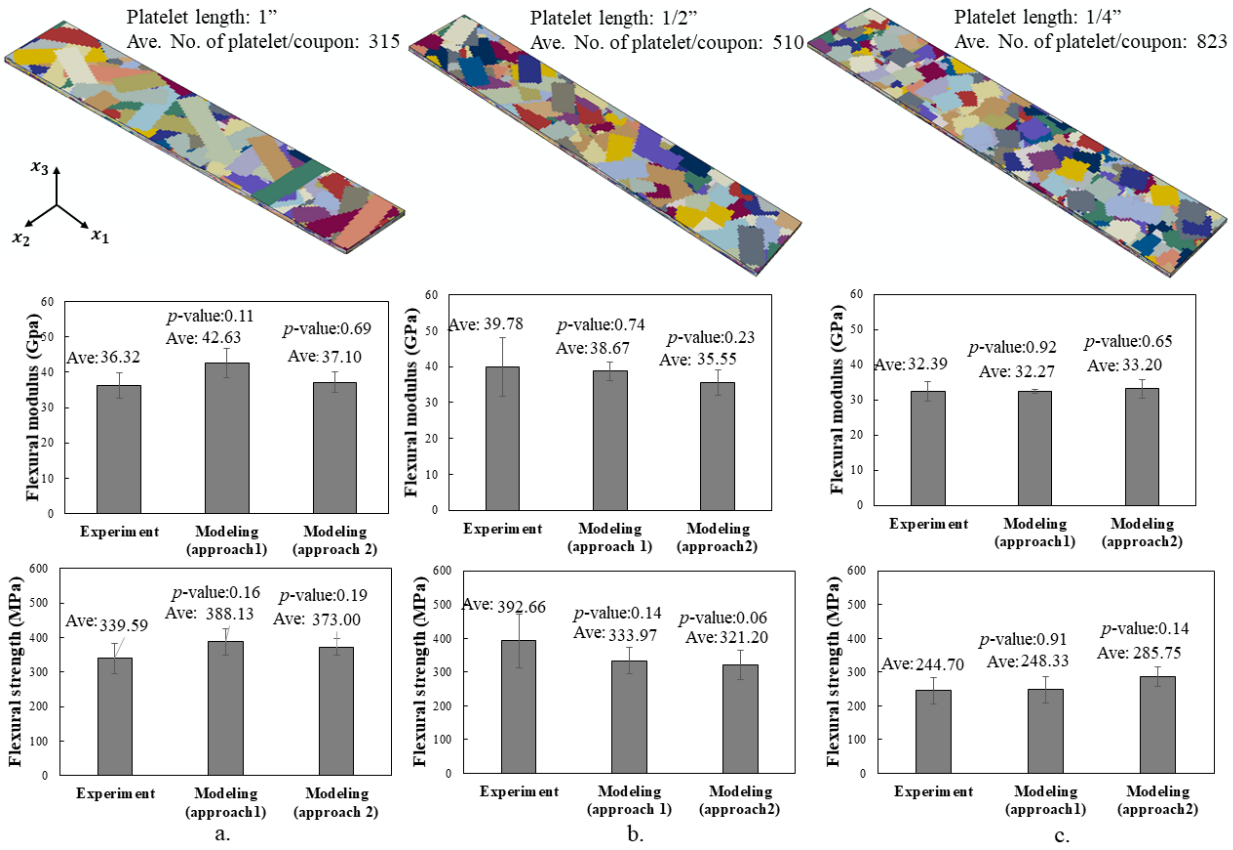

Figure 43 Variability of effective flexural modulus and strength in a stochastic PPMC made of (a) 1”, (b) ½”, and (c) ¼” platelet length in simulations and experiments

8.2 Analysis of damage states in PPMC

The heterogenous mesostructure of PPMC with random orientation of platelets form multiple simultaneous damage sites and provide alternative damage progression paths during the three-point bending test. A primary damage path under three-point bending was observed away from the bending line, indicating the role of non-uniform FOD on damage initiation and propagation along the different locations. The location of damage site varied from one sample to another and was affected by platelet length. Figure 44-a shows a strain field on the surface of 1” and ½” PPMC specimens at the failure with localized strain away from the center location. The strain concentration in x_1 direction is due to the damage propagation. It can be observed that 1”

sample had a more concentrated damage localization, whereas ½" sample showed more spread out damage. Figure 44-c shows the complex pattern of failure modes at the ultimate strength of virtual three-point bending tests at DPZ confined to the region of 40mm around the middle roller. The local dissimilar FOD state in a stochastic mesostructure lead to the localized material softening and the damage propagation before ultimate strength was reached. The distribution of the damage variables in DPZ shows multiple local failures in the matrix direction and through the thickness attributed to the debonding of the platelets.

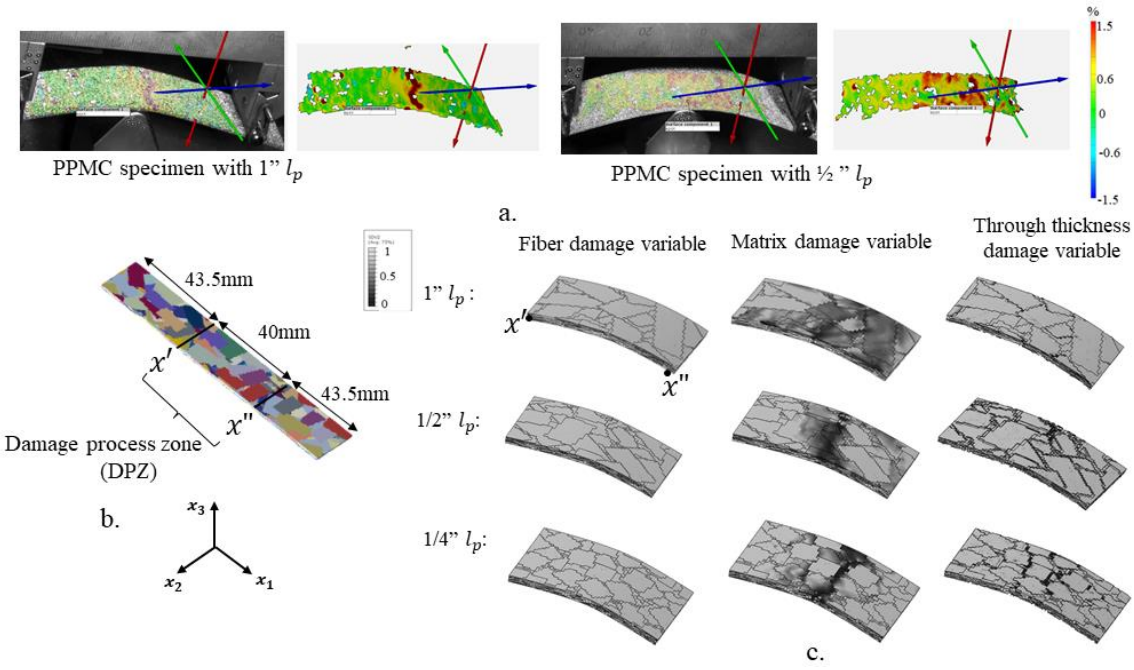

Figure 44 (a) DIC image of PPMC three point bending test at maximum stress (b) Identified DPZ (c) Distribution of the damage variables in three-point bending simulations of PPMCs with 1", ½", and ¼" prepreg platelet length

Figure 45 compares the cumulative relative frequency of the damage variables in DPZ at the maximum stress for the weakest and strongest virtual coupons in every group of PPMC

samples. The cumulative relative frequency of damage variables was calculated by considering the damaged elements as a fraction of total number of elements. Stronger samples with the prescribed platelet length show higher accumulated damage variable compared to the weaker ones. Fiber damage in coupons with ¼" l_p shows the lower accumulated variable in fiber direction due to the shorter platelet length, while the transverse and through thickness damage variables were about the same level for all specimens with prescribed l_p.

Figure 45-b shows the average degree of alignment of a_{11} and the coefficient of variance (CV) of virtual PPMC in DPZ with respect to the predicted strength value. A linear regression fit was used to see the correlation between the average a_{11}, $\bar{a}_{11}$, and the strength. The results show that the higher $\bar{a}_{11}$ leads to the improved strength of material. The higher difference between CV of $\bar{a}_{11}$ for the PPMC coupons with longer platelets (1") implies less uniform orientation of platelets and higher statistical dissimilarities between the mesostructure of the coupons. Strength values vary from one coupon to another due to inherent morphological dissimilarities.

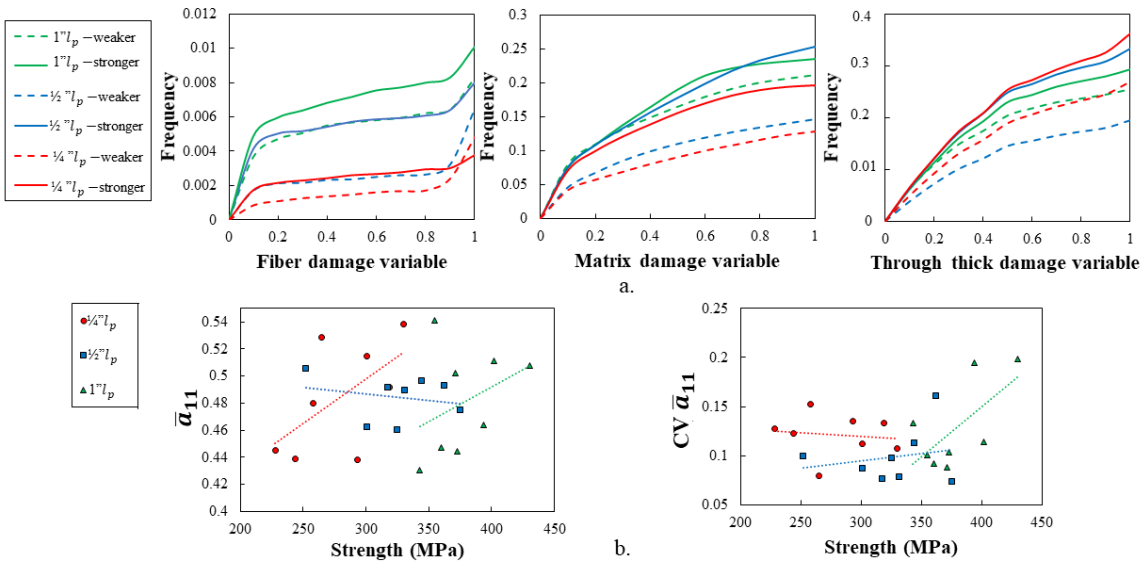

Figure 45 (a) Cumulative frequency of the damage variables at DPZ in three-point bending simulations of PPMCs (b) Variability of $\bar{a}_{11}$ of virtual PPMC coupons with respect to the predicted strength

8.3 Characterization of local platelet orientation and stiffness

The increased platelet length in the same size coupon with stochastic meso-morphology decreases the platelet count and provides for enhanced local dissimilarity in platelet orientation and loss of heterogeneity along the length of an individual coupon. This implies how the platelet size changes the orientation state and morphology of the entire system. Fewer platelets in a stochastic system implies fewer possible orientation states, which increases the probability of very different local orientation states to occur, both within a coupon and between several different coupons. Figure 46-a shows three cross-sectional images captured at a random location of polished samples fabricated with 1", ½", and ¼"l_p. The local platelet orientation state of PPMCs were measured for polished specimens. a_{11} , shown in Figure 46, is representative the platelet degree of alignments for each cross-sectional image. PPMC with smaller platelet length shows more random 2D local platelet orientation ($a_{11} = 0.48$) compared with PPMCs with longer platelet

length. Figure 46-b shows the a_{11} distribution over the virtual PPMC specimens with prescribed platelet length, calculated from the fiber orientation vectors in each voxel stack through the plate thickness. This represents the variability of local through-thickness a_{11} within a virtual coupon. The local through-thickness a_{11} was calculated along the A-A line (shown in Figure 46-b) for virtual specimen with 1" and ¼" l_p and shows a more uniform distribution for the virtual specimen with smaller l_p (1/4") (Figure 46-c).

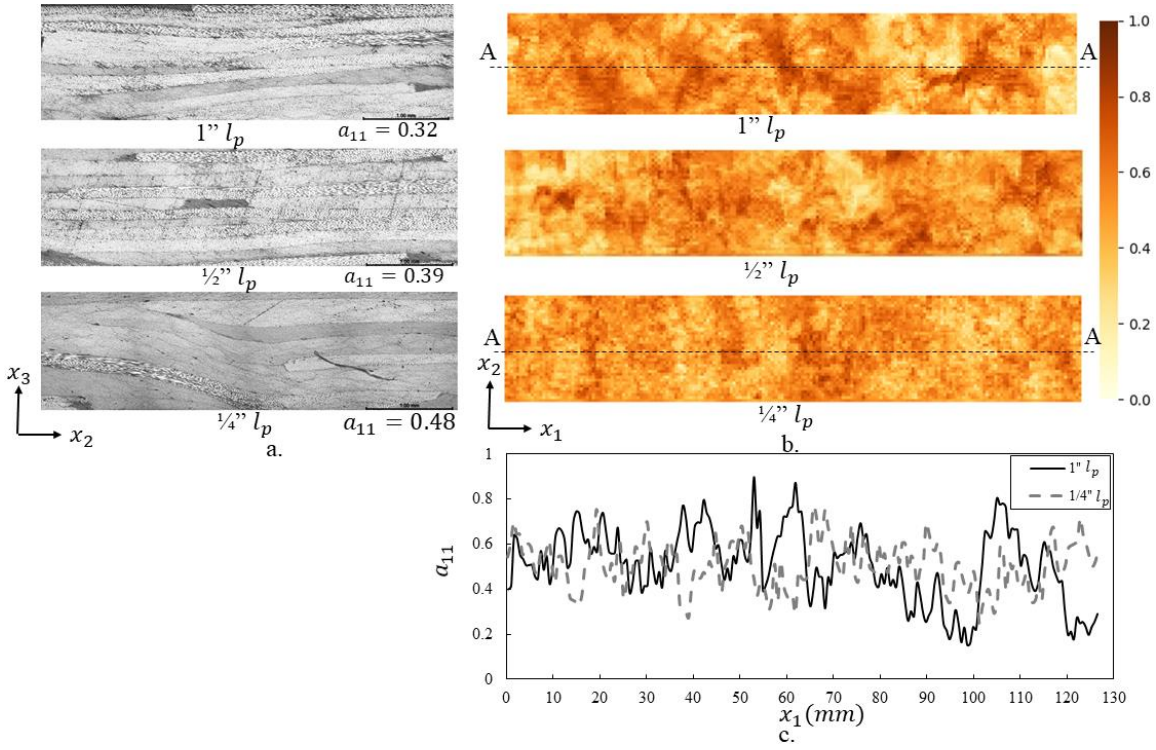

Figure 46 (a) Cross-section micrographs of PPMCs (b) distribution of the through thickness a_{11} within the virtual coupons with prescribed platelet length (c) a_{11}distribution through the thickness along the A-A line

Figure 47 shows the variability of a_{11} (degree of alignment) and B_{11} (1st component of stiffness B matrix) within the stronger and weaker virtual coupons with a prescribed platelet length

along the DPZ with the distribution of the matrix damage variable at the ultimate strength. The scattered pattern of damage with the higher cumulative variable in stronger coupons (Figure 47) implies the more arrested damage propagation and redistribution of load path during loading due to the PPMC redundancy structural system resulting in the delay in ultimate failure. a_{11} shows more uniform state within the specimen with smaller platelet length (1/4" and ½") compared with longer platelets (1"). The variability of B_{11} along the DPZ shown in Figure 47 indicated the sensitivity of the local stiffness to the stochastic platelet orientation and geometry.

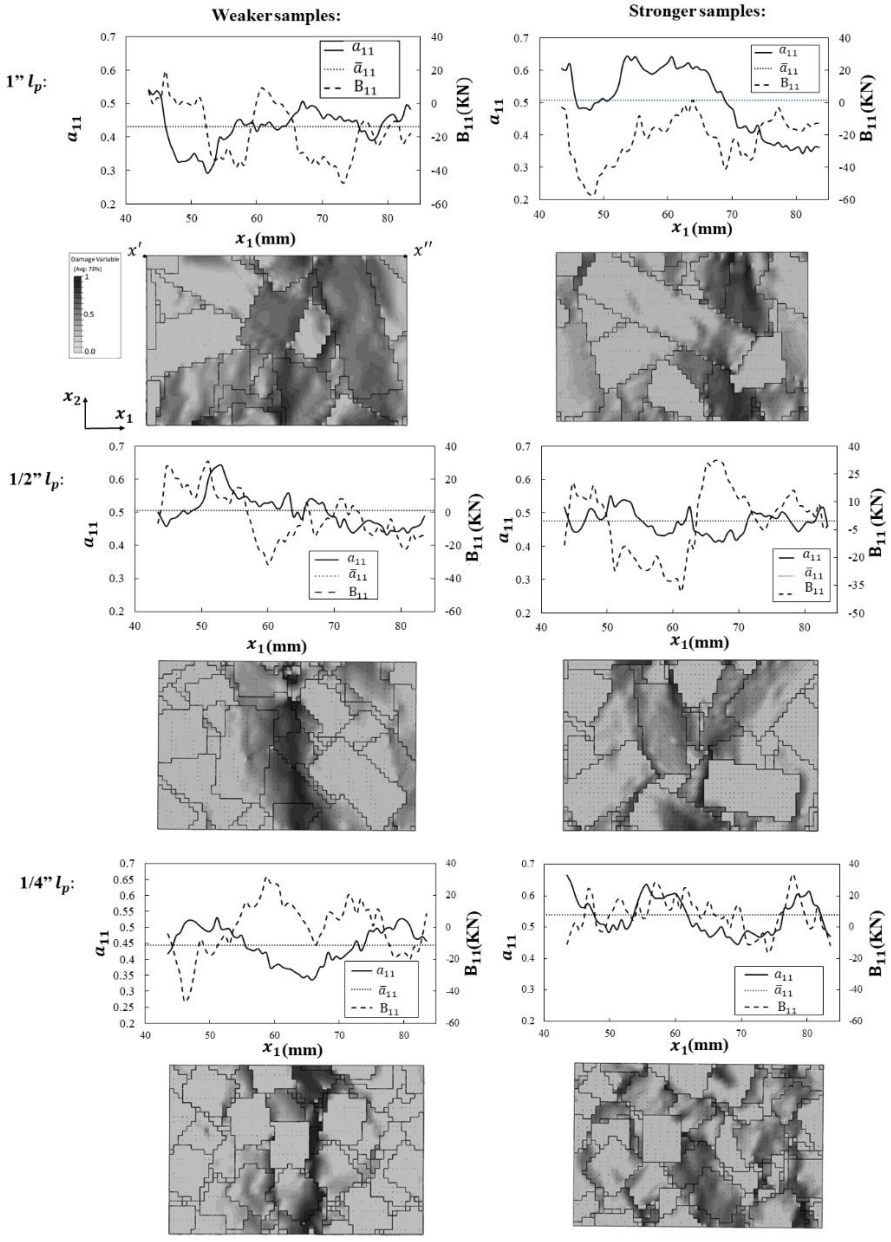

Figure 47 Variation of a_{11} and B_{11} and the distribution of matrix damage variable within the virtual PPMC specimens at DPZ

9 ROLE OF THE MORPHOLOGY IN FREEZE-CASTED CERAMIC ON THE COMPRESSIVE BEHAVIOR

9.1 Effect of off-axis compressive loading on the mechanical properties

The deformation of on samples' surface was calculated using DIC. The strain field was computed based on the corresponding displacement in the facets [110], the size of the facets was set to 19-pixels. The average value of the strain was calculated inside of the area between the compression platens and used to plot the stress-strain profile under compressive loading. Figure 48 shows the surface pattern of strain on the samples before the failure and at the propagation of failure for longitudinal, transverse and 15^{o} off-axis compressive loading. Specifically, during the longitudinal loading (0^{o} sample) the strain localization takes place in the narrow strips of the material that begin to develop in the elastic regime. These strain localization patterns can be attributed to the internal load paths that originate inside of the material due to the porosity and voids at the intersection of the lamellar crystals and porous grains, as well as the intrinsic misalignment of the lamellar walls. Other sources for strain localization can include material defects, such as pores, or variations in local relative density. Once the strain localization originates in the material it results in the stress concentration, which leads to local material failure. The average orientation of these load paths was found to be 2.8° relative to the loading axis in four compressive tests under 0° angle. Figure 48-a shows the orientation of this load path for 0^{o} experiment. This indicates the effective misalignment angle of the lamellar ice-templated alumina for the 0^{o} sample configuration. For a 15° off-axis loading, the strain localization occurs along the line oriented at 17° relative to the loading axis (Figure 48-c). Consequently, the effective misalignment angle increases the overall off-axis loading angle by about 2°. The average of effective misalignment angle for 15° off-axis loading tests was 2.6^{o}. The mechanical response of

sample for 15° off-axis loading is characterized by substantial amount of the shear deformation, which results in progressive failure of the sample during the increased loading. Figure 48-e shows the strain in loading direction localization pattern relative to the direction perpendicular to the loading axis in a 90º loading test. The effective misalignment angle for this transverse sample configuration was equal to 1.8°. The transverse loading (90º sample) was characterized by extensive progressive crushing that occurs near the platens. The stress-strain curves corresponding to compressive loading of 0º, 15º and 90º ice-templated samples are shown in Figure 49 with corresponding principal strain distribution obtained by DIC analysis. In addition, the stress-strain diagram shows the strain distribution field at the initiation of failure and during the failure propagation. The mechanical behavior for the samples is governed by linear response followed by progressive crushing, as evident from the stress-strain curve. Once crushing initiated and propagated DIC could not track the strain evolution, so applied crosshead displacement was used to calculate the strain in the sample. The modulus and strength of longitudinal compressive test (0º sample) was significantly higher than 15º and 90º samples, and the strength and modulus in transverse loading (90º sample) was significantly lower, as one would expect based on the transverse orientation of the ice growth with respect to the loading direction. It should be pointed out, that interpretation of stress-strain measurements beyond the onset of failure in the material is complicated, due to the inability of the DIC software to track the large regions. At the same time, the present DIC analysis shows that the progressive crushing of the material was taking place over the increased homogenized stress levels, while the local values of strain in the material remained relatively small. Once crushing occurred during the plateau regime, DIC could not be used to track the strain evolution due to the loss of spackle pattern. Therefore, strain in plateau regime for all the samples was calculated based on the crosshead displacement. The present experimental results

were used to establish the correlation between micro-mechanical deformation of lamellar walls, predicted from the computational micromechanics, and the homogenized bulk response of the material.

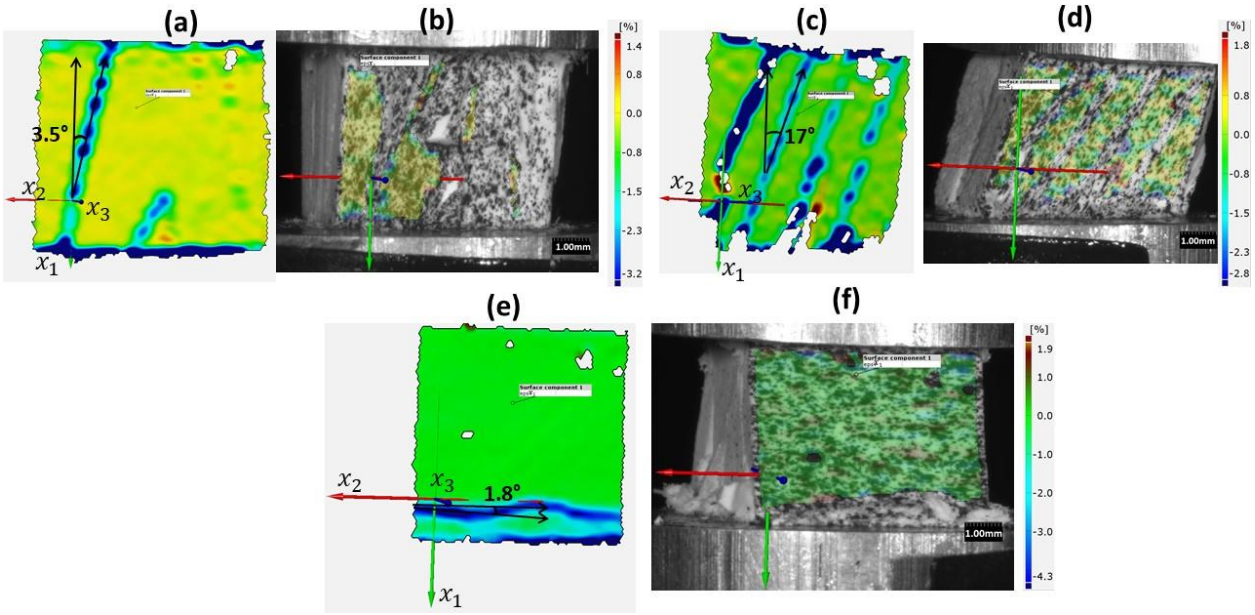

Figure 48 (a) DIC images for 0° loading at 0.7% strain (b) DIC image for 0° loading at failure propagation (c) DIC images for 15° loading at 0.4% strain (d) DIC image for 15° loading at failure propagation (e) DIC images for 15° loading at 0.2% strain (f) DIC image

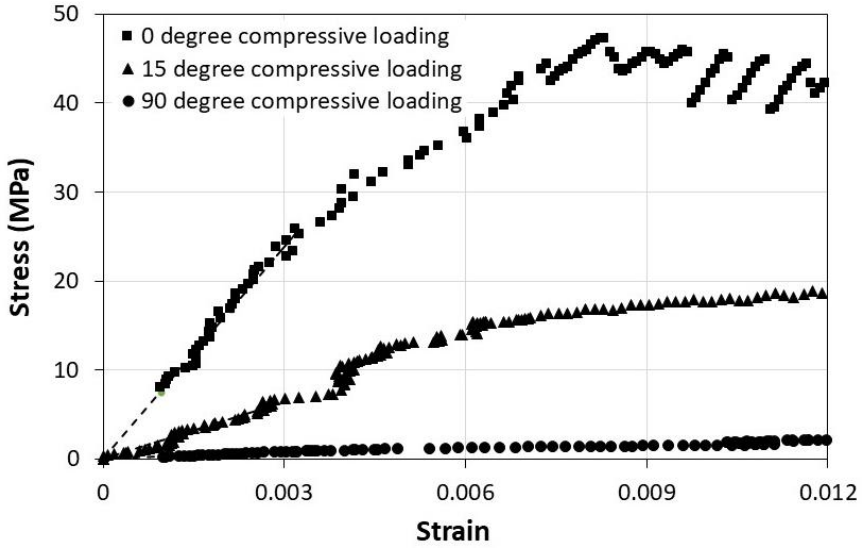

Figure 49 Stress strain curve for 0º, 15º and 90º compressive loading tests

9.2 Effective stress-strain curves from micromechanical analysis

In order to quantify the compressive stiffness and strength response of ice-templated alumina under off-axis loading, the micromechanical RVE analysis with smeared cracking approach, described in the previous section, was used. Different compressive loading cases were considered with material compressive strengths of 250MPa, 500MPa and 1GPa, as explained in Section 2.3. The homogenized compressive stress and strain response were calculated using Equations 6 and 7. Figure 50 shows the effect of the bulk strength on the compressive strength of the porous alumina with different loading angles, namely, 0°, 5°, 12 and 90°, using 250 MPa compressive bulk strength. The parametric study considered material compressive strength of 250 MPa, 500 MPa and 1 GPa. These values were selected from the consideration of the flexural strength of macroscopic alumina [76] and the strength of a single crystal [77]. From the of micro-mechanical analysis, it is evident that 250 MPa provides more reasonable predictions of strength compared with experimental results. The use of lower strength for the lamellar walls can be

explained by the polycrystalline nature of the lamellar walls in ice-templated ceramic. The parametric analysis shows a steep decline of compressive strength with increasing loading angle from 0° to 90°. As the bulk strength increases the role of wall misalignment or off-axis loading causes more significant reduction in strength of ice-templated material.

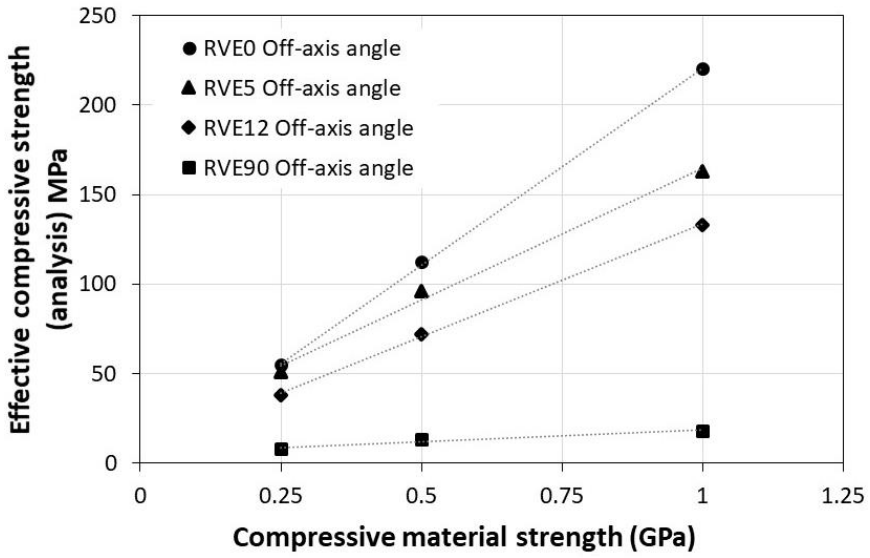

Figure 50 Effective compressive strength response of ice-templated alumina computed for RVE analysis under different off-axes loading

Figure 51 shows the stress-strain curve for the 0^o and 5° compressive loading analysis using 250 MPa compressive strength and compared with the compression testing in ice crystal growth direction, with 4.5° measured misaligned angle. The initial elastic deformation of the model involves axial compression of the lamellar walls, and the slope for the linear part of the stress-strain. The compressive strength for the experimental test under longitudinal compressive loading (44 MPa) agreed relatively close with the 5° RVE analysis, as well.

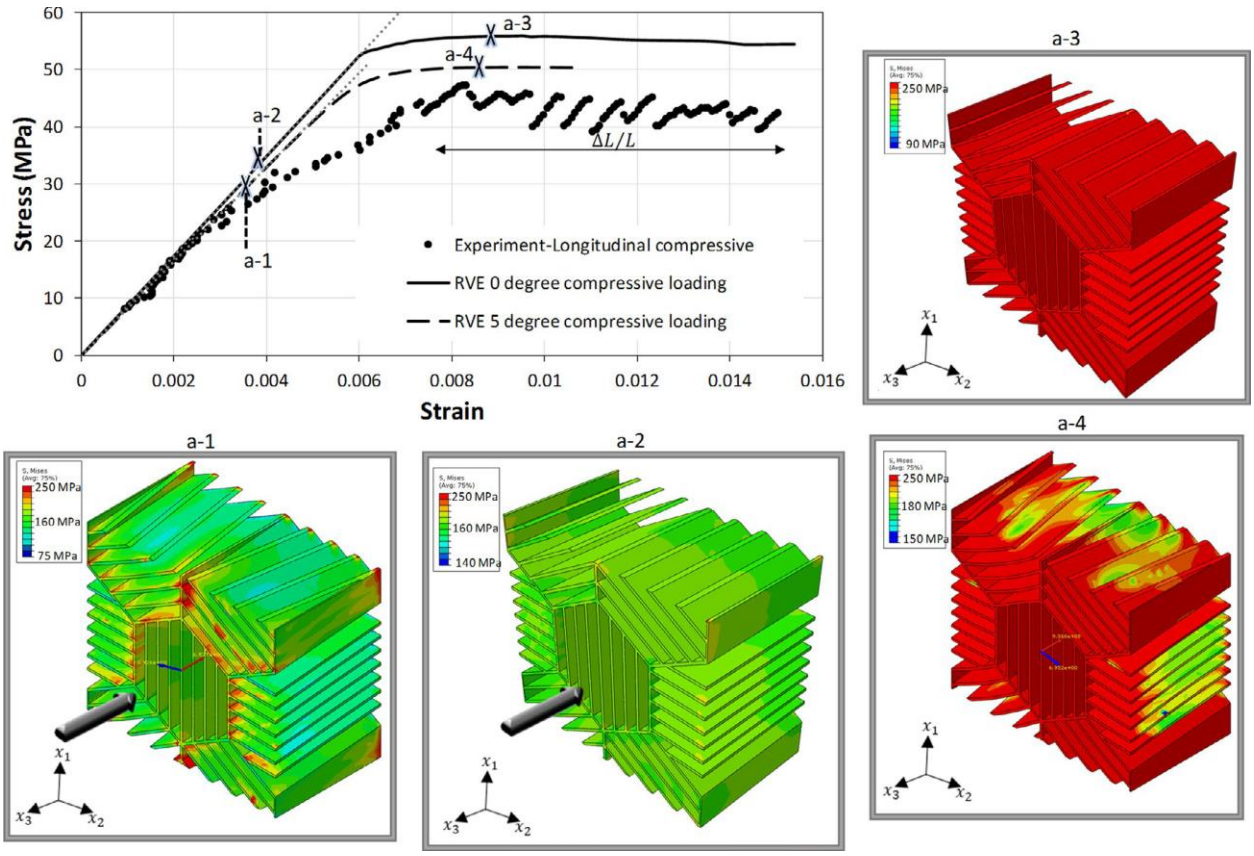

Figure 51 Stress strain curve for 0º and 5º off-axis compressive loading analysis used 250 MPa compressive strength of material, and for the longitudinal off-axis compressive loading test a-1) RVE elastic state for 0° compressive loading a-2) a-2) RVE elastic state for 55° off-axis compressive loading a-3) RVE deformed state for 0° off-axis compressive loading a-4) RVE deformed state for 5° off-axis compressive loading

9.3 Off-axis modulus and strength prediction with effective misalignment angle

To characterize the modulus of ice-templated alumina subjected to off-axis loading, orthotropic material model was used. (Equation 54) provided the relation for the off-axis modulus of orthotropic material using engineering moduli in principal material directions of the material [111].

$$\frac{\mathbf{1}}{\boldsymbol{E_{x_1}}} = \frac{\boldsymbol{\cos^2\theta}}{\boldsymbol{E_1}}(\boldsymbol{\cos^2\theta - n^2\nu_{12}}) + \frac{\boldsymbol{\sin^2\theta}}{\boldsymbol{E_2}}(\boldsymbol{\sin^2\theta - m^2\nu_{21}}) + \frac{\boldsymbol{\cos^2\theta \sin^2\theta}}{\boldsymbol{G_{12}}} \quad \text{(Equation 54)}$$

E_{x_1} is the off-axis modulus, E_1 and E_2 are the elastic longitudinal and transverse moduli, 8.7GPa and 1GPa, respectively, computed from the 0º and 90º RVE analysis; $G_{12} = 0.7$ GPa is the shear moduli in 1-2 plane calculated from shear loading RVE model, subjected to the shear loading; $\nu_{12} = 0.21$ is the Poisson ratio associated with loading in principal direction 1 and strain in principal direction 2 , ν_{21} is the Poisson ratio associated with loading in principal direction 2 and strain in direction 1, and θ is the off-axis loading angle. The ratio of the lateral strain to the axial strain for longitudinal compressive load analysis in linear elastic part represented ν_{12} and υ_{21} is calculated by (Equation 55).

$$\boldsymbol{\upsilon_{21} = \frac{E_2}{E_1}\upsilon_{12}} \quad \text{(Equation 55)}$$

The off-axis modulus was calculated from the discrete RVE analyses with 5°,12°, 15°, as well as using (Equation 9). Calculation of modulus using RVE analysis and with using orthotropic constitutive relationship shows that orthotropic model provides a good match indicating appropriate anisotropic homogenization model for the material.

Figure 52 shows the comparison between the off-axis experimental modulus and modulus values calculated using present RVE modeling. To account for the intrinsic misalignment angles of the lamellar walls developed during the freeze casting, the results of the DIC analysis during compressive testing were used. Specifically, the strain localization load paths were used to include the misalignment angle, which was discussed in the previous section. The variation of the off-axis modulus taking into account the measured effective misalignment angle for longitudinal,

transverse and 15º off-axis compressive loading tests are shown in Figure 52 and compared closely with the predicted off-axis modulus from RVE analysis.

The experimental and modeling prediction data are following the steep decline of the off-axis modulus at around 15º. The modeling prediction of 0º, taking into account the effective misalignment angles in the range of 1.5° and 4.5° determined from DIC, showed higher values than the experimental data. This effect can be attributed to the material defects and distribution of the actual misalignment angles in the physical sample, as opposed to the micro-mechanical model used herein, which used a single off-axis angle. The RVE analysis for 90° loading also showed good agreement with the transverse compressive tests, which had the average of 88.8° of the effective off-axis angle.

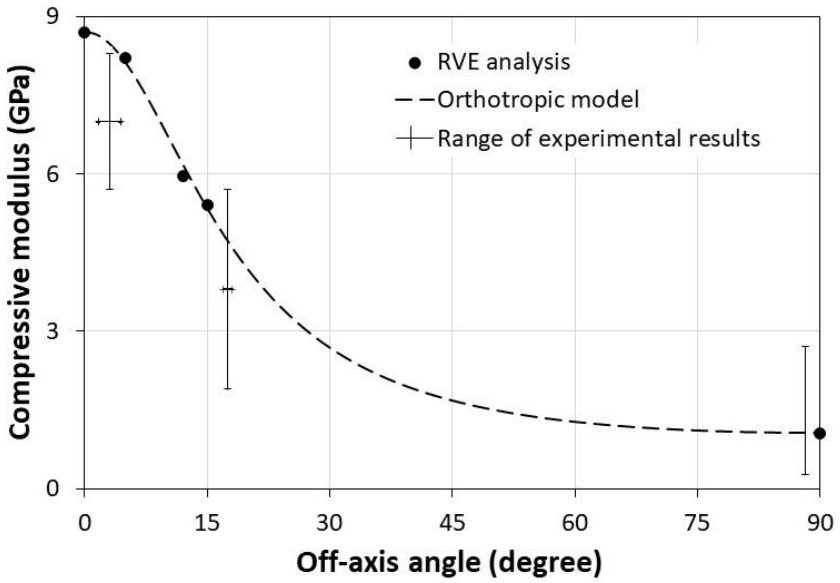

Figure 52 Effective compressive modulus of ice-templated alumina computed for RVE analysis, orthotropic model and experiment with respect to the off-axis angle

Figure 53 shows a comparison between the strength from RVE analysis, using 250 MPa compressive bulk strength, and off-axis compressive tests with respect to the effective off-axis

angle. The effective off-axis angle was determined using the measured misalignment angle captured by DIC. The theoretical curve was calculated based on Tsai-Hill homogenized failure theory assuming 2D state of stress and using results of RVE analysis for compressive strength in 0^o and 90^o, as well as shear strength of 8.5 MPa. (Equation **56**) shows the modified Tsai-Hill criterion, where the coefficients f_{ii} are fourth order strength tensors calculated by (Equation 57) [58]. The uniaxial compressive strength (0^o), σ_{1u}, compressive transverse (90^o) strength, σ_{2u}, and in-plane shear loading, τ_{6u}, define the failure surface given by (Equation 11). The comparison between the average experimental results and modeling predictions reveals that for 0^o loading (55 MPa and 37.5 MPa for RVE analysis and experimental average, respectively) is the highest, while is the most accurate for the transverse compressive loading (8 MPa and 7.5 MPa for RVE analysis and experimental average, respectively). This result can be explained by the presence of the material defects, such as pores, and local misalignment in the physical samples that results in larger discrepancy for 0^o sample. Furthermore, the compressive strength for effective off-axis loading angle in the range of 2° and 4.5° is between 30 MPa and 47 MPa, agreed with the strength from the RVE analysis for 5^o (51 MPa) off-axis loading.

$$\boldsymbol{f_{11}\sigma_1^2 + f_{22}\sigma_2^2 + f_{66}\tau_6^2 - f_{11}\sigma_1\sigma_2 = 1} \quad \text{(Equation 56)}$$

$$\boldsymbol{f_{11} = \frac{1}{\sigma_{1u}^2}} \quad \text{(Equation 57)}$$

$$\boldsymbol{f_{22} = \frac{1}{\sigma_{2u}^2}} \quad \text{(Equation 58)}$$

$$\boldsymbol{f_{66} = \frac{1}{\tau_{6u}^2}} \quad \text{(Equation 59)}$$

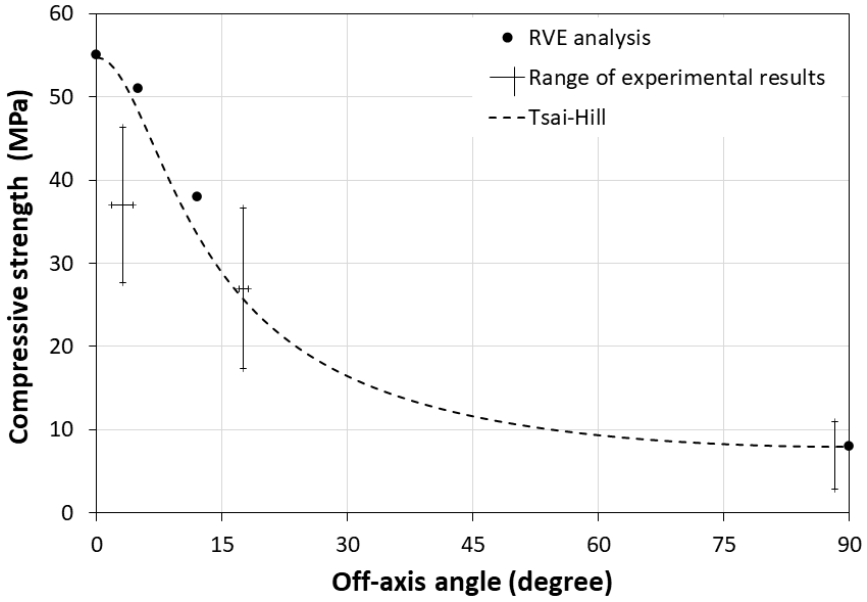

Figure 53 Compressive strength of ice-templated alumina computed from RVE analysis and compression experiments considering effective off-axis angle

9.4 Role of local orientation of the lamellar structure on the mechanical properties and the failure behavior

Figure 54 shows the lamellar structure's local orientation in a freeze-casted ceramics micrograph. The local orientation of lamellar structure results in the local changes in stiffness. The distribution of the local orientation in lamellar structure was measured through microscopy analysis and image processing using ImageJ software. The measured standard deviation of local orientation in lamellar structure was ±3.3º (Figure 54). A normal distribution defines a spatially varying field over elements with the two parameters of mean and standard deviation. The mean of the normal distribution was considered as the compressive loading angle. In this study, three cases of compressive loading angle were considered, 0º, 15º, and 90º. Figure 55 shows a comparison between the stress-strain curves from the compressive tests and the simulation results with the initial linear-elastic response of the stress-strain behavior, followed by the non-linear progressive failure. Figure 57 shows the range of the compressive strength and modulus from experiments compared with simulation data. The variation of the compressive strength and modulus results

from the local structural orientation within the morphology of the material. The compressive modulus and strength from homogenized modeling agreed with the experiment results. The average compressive modulus and strength from the simulations for the 0 degree compressive loading were 8±0.3GPa and 37±3MPa, respectively. With increased compressive loading angle to 90º, the average compressive modulus and strength dropped to 1.1±0.01GPa and 6.9±0.01 MPa, respectively.

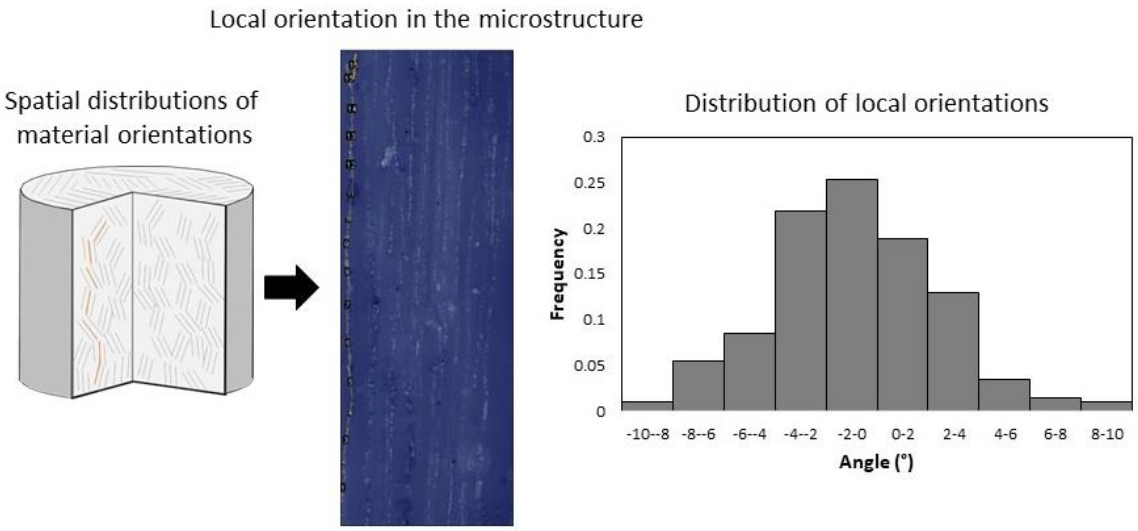

Figure 54 Distribution of local orientation of the lamellar structure

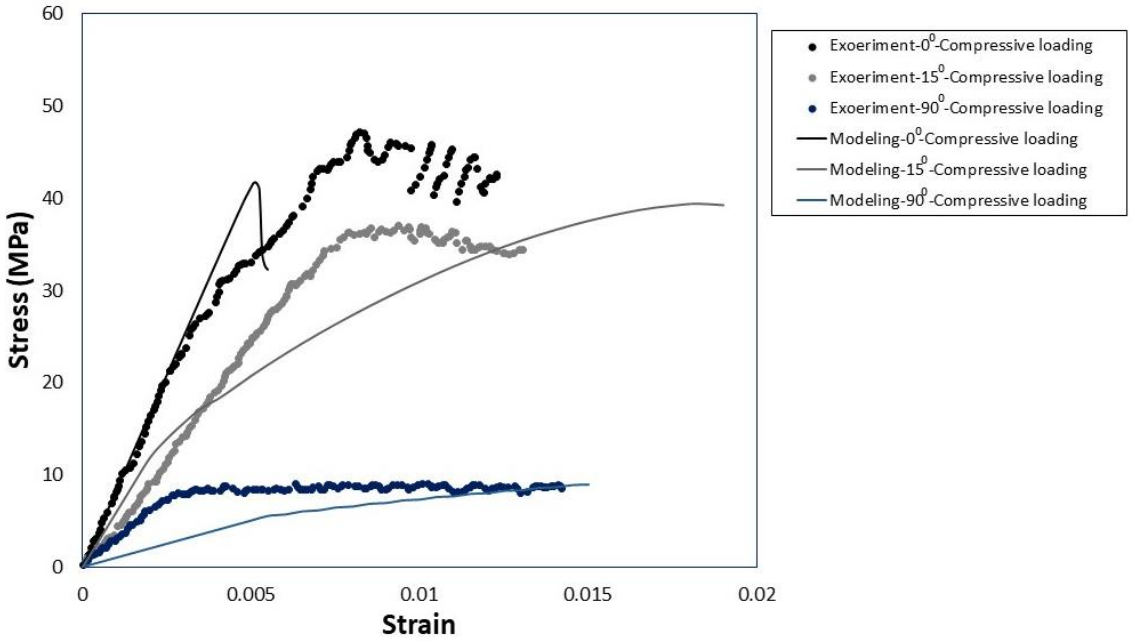

Figure 55 Comparison between stress strain curve for 0º, 15º and 90 º compressive loading of homogenized model and experiments

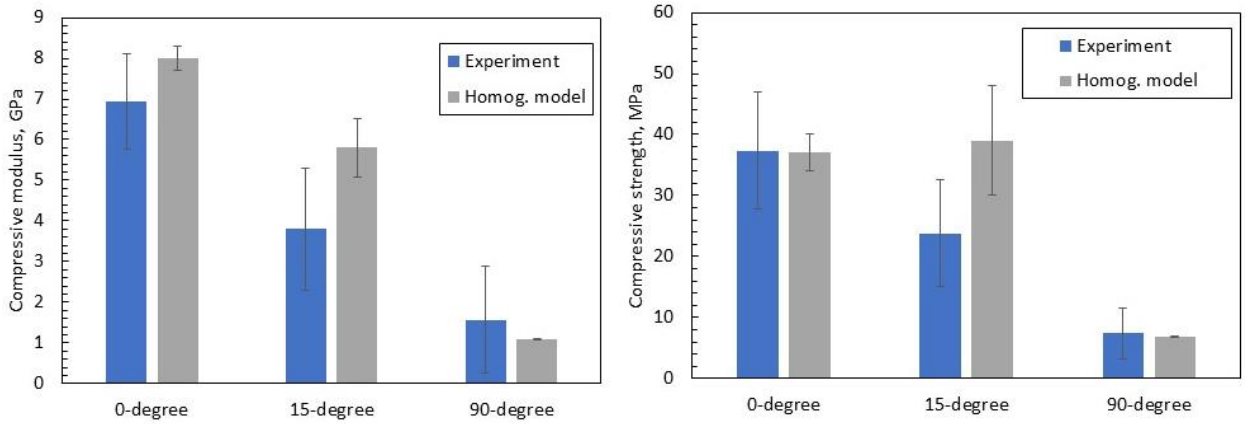

Figure 56 Compressive modulus and strength calculated from the homogenized model and measured from the experiments

Figure 57 shows the patterns of the longitudinal and transverse damage variables within the material at the maximum stress of simulations and the failed specimens under off-axis loading. The simulation results showed that the dominant failure modes were the longitudinal failure, while

increasing the compressive loading to 90º resulted in the shifted failure mode to the transverse failure. The shear deformation due to the 15º compressive loading was observed in both simulation and experiment.

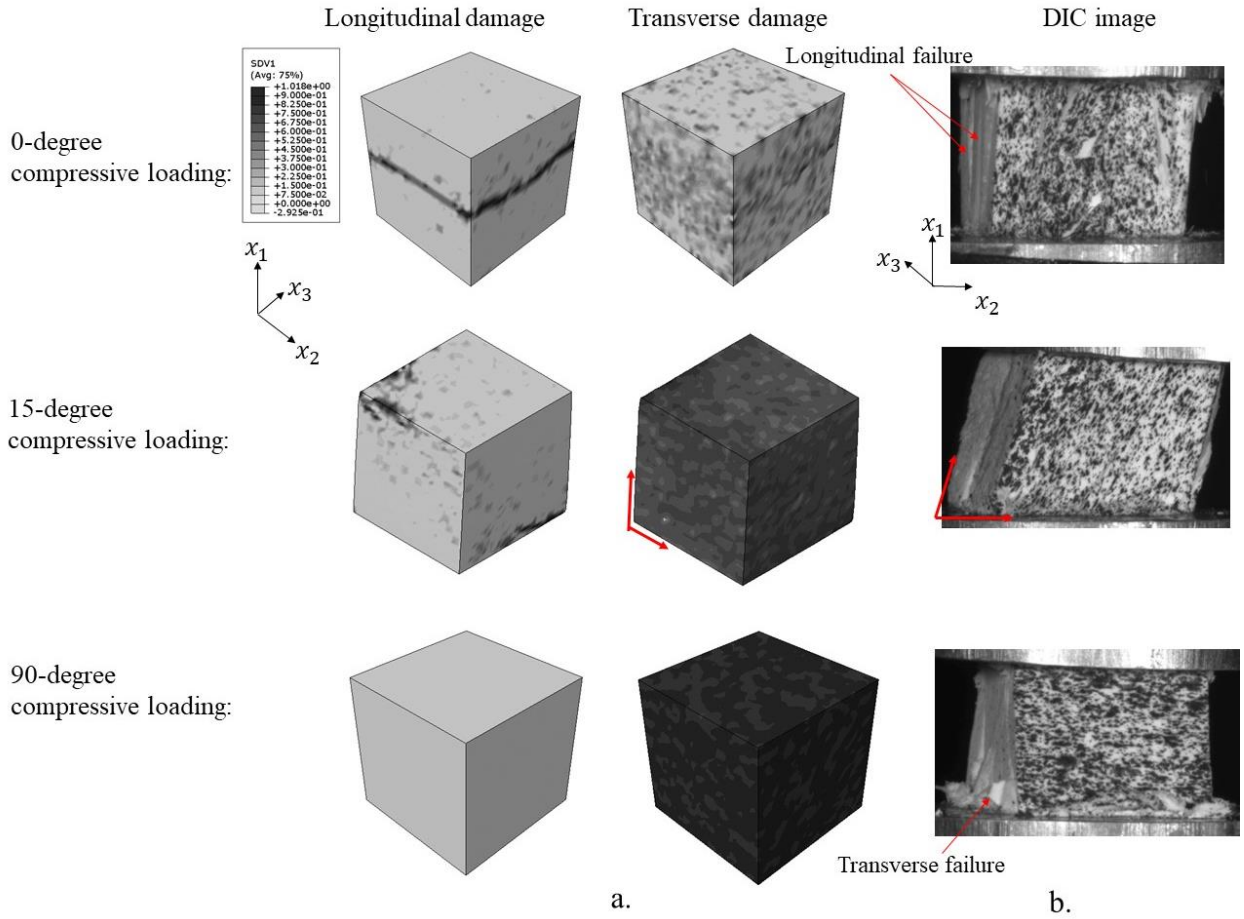

Figure 57 (a) Pattern of the damage variables in homogenized model (b) failed specimens under off-axis compressive loading

Figure 58 and Figure 59 show the longitudinal and transverse strain distribution on the surface of the virtual and in-situ specimen at the linear elastic region and the failure, respectively. The strain field in longitudinal and transverse directions for both simulation and experiments have gradients due to local changes in the orientation of the material structure. The strain localization

observed as the narrow strips at the failure specifically for the 0-degree compressive loading can be attributed to the internal load paths that originate inside of the material due to the porosity at the intersection of the lamellar structure and porous grains, as well as the intrinsic local and global orientation of the lamellar structure. This unique behavior was observed in the simulation specifically for the longitudinal strain of 0-degree compressive loading.

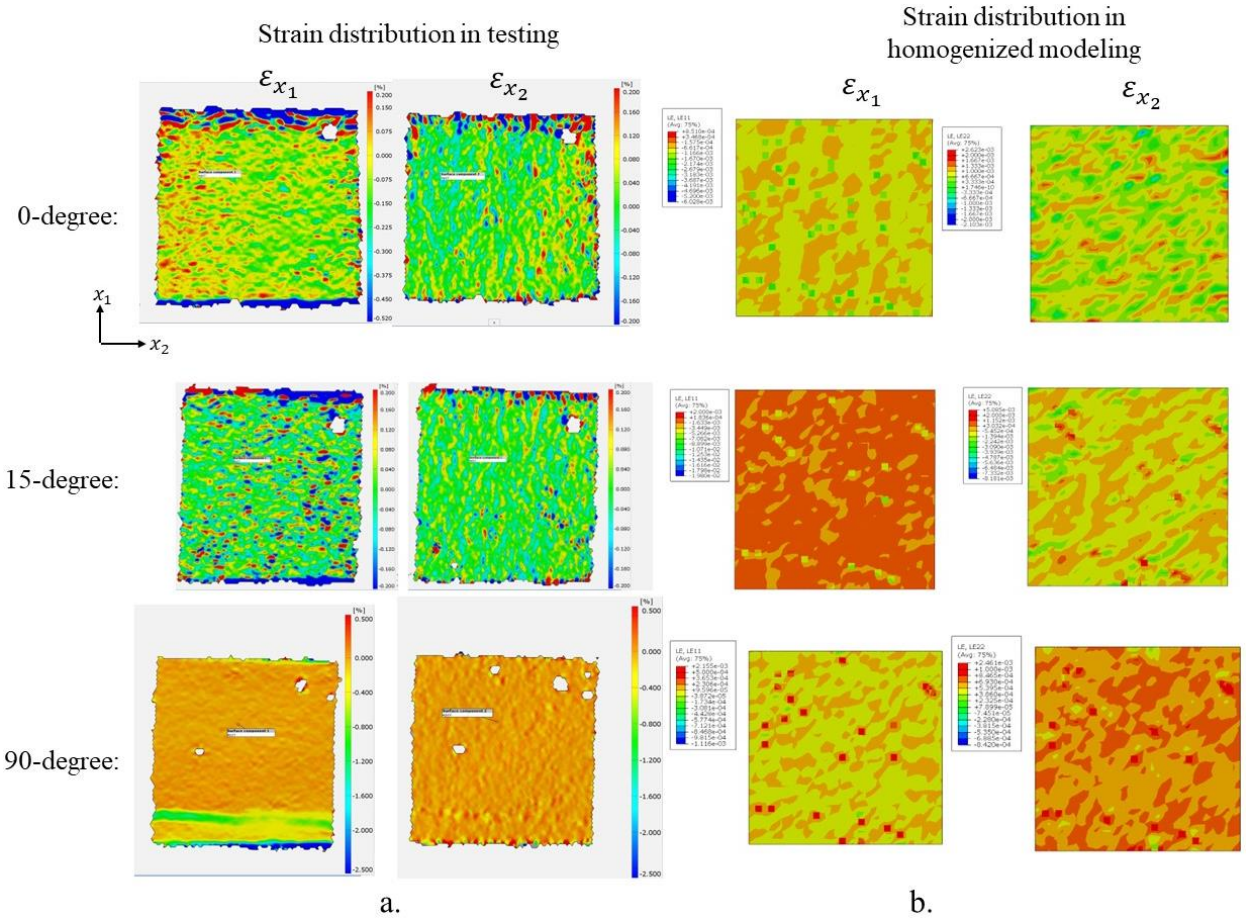

Figure 58 Strain distribution and on the surface of the sample at elastic region for (a) in-situ and (b) virtual testing

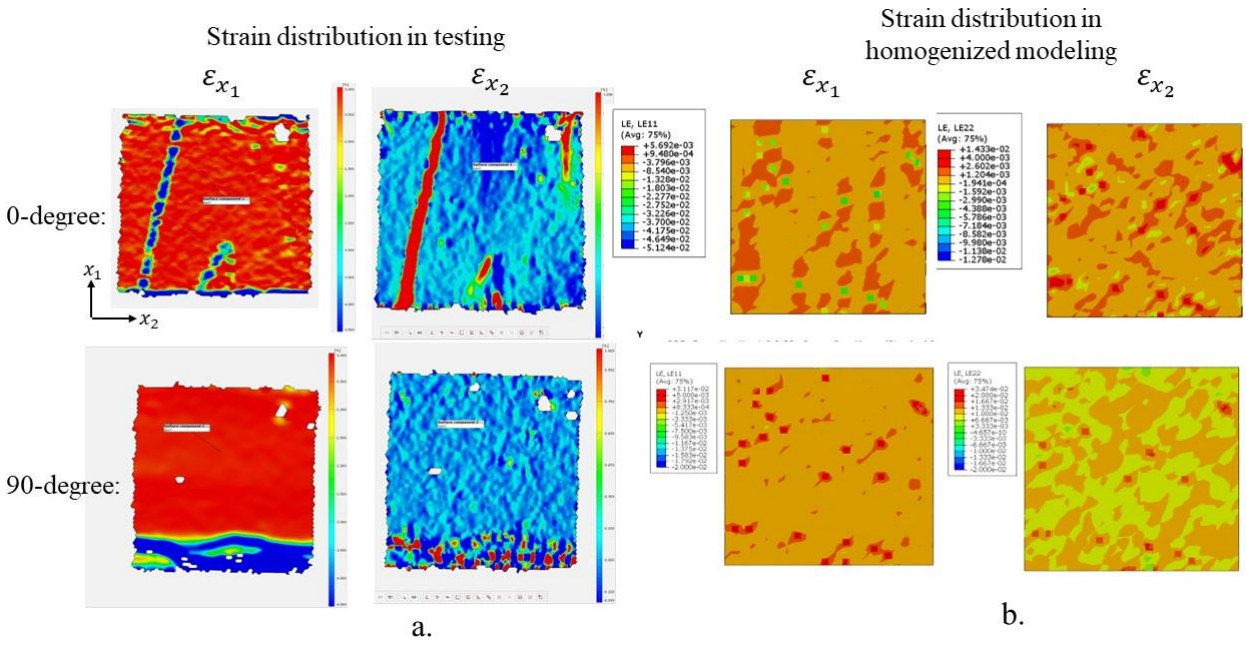

Figure 59 Strain distribution and on the surface of the sample at failure region for (a) in-situ and (b) virtual testing

Figure 60 shows the fraction of damaged elements (d_i> 0) in the longitudinal and transverse direction with respect to the strain value in 0º, 15º, and 90º compressive loading simulations. The damage initiated from the strain of 0.5%, where the non-linear behavior of the material was observed in the stress-strain curves. The fraction of the damage elements in either longitudinal or transverse direction reached one immediately after damage initiation. This implies the progressive local damage before reaching the ultimate strength, and the cumulative damage evolves to the macrocracks.

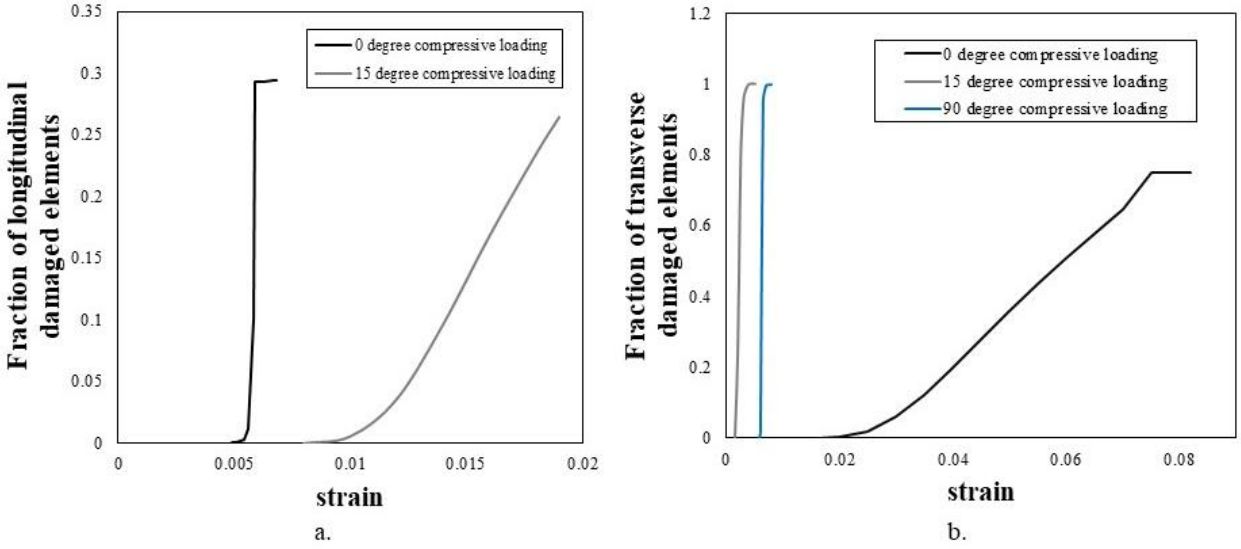

Figure 60 Fraction of damaged elements in (a) longitudinal and (b) transverse direction with respect to the strain in simulation

10 CONCLUSION

Various computational models were developed to study the effect of the morphology in hierarchical material, including two types of LDFCs, PPMC and organosheet, and freeze-casted alumina ceramic, on the mechanical properties and failure behavior. The computational modeling was established based on the independent material characterizations and micro-mechanical homogenization. The developed models for LDFCs included the geometrical arrangement of bundle/platelets. Statistical microscopy analysis was performed to characterize the fiber and bundle orientation and volume fraction and used to generate stochastic morphology. The computational models for freeze-casted ceramics were developed through the 3-D micro-mechanical RVE model based on the honeycomb analogy and the macroscale homogenized model consisting of the distribution of the local lamellar orientation. Damage mechanisms were used to model damage's evolution in the structure of the materials. The modeling predictions for the mechanical properties of the material were in good agreement with the experimental results.

1. The simulation results of the organosheet provided a quantitative measure of the improvement in the mechanical properties for the increased bundle alignment when a_{11} varied from 0.58 to 0.62. The variability in modulus and strength for tensile and flexural loading was correlated with the stochastic bundle distribution in the organosheet. The experiment and modeling results reveal high dependency of the effective flexural modulus and strength on the span length. The simulation results for both flexural and tensile modeling showed that the dominant failure modes were failure in PA6 pockets and the transverse failure in the bundles.
2. The notched strength of organosheet with the diameter of 2mm was at the range of the unnotched coupons (175 MPa), while increasing the hole diameter from

2mm to 6mm resulted in a decrease from 178 MPa to 132 MPa. The notch insensitivity of the 2mm OHT specimens was attributed to the increased plasticity in the matrix and more homogeneous FOD in organosheet. The results showed that increasing the hole diameter leads to lower accumulated damage variables in OHT simulation along with the intensive local damage in the vicinity of the hole. The notched strength predicted from PFA simulations and measured from experiments were used to calibrate the analytical PSC and MPSC models to predict the notch sensitivity of the organosheet. The analytical curves fitted through the simulation and experiment results were nearly identical. The results show that the strength of OHT specimen with hole diameter lower than 2mm is not sensitive to the notch discontinuity.

3. Experimental studies showed improved average flexural strength and modulus for the PPMCs with ½" platelet length compared with the PPMCs with 1" and ¼" platelet length. The variability of effective flexural properties caused by the variability of stochastic mesostructure was demonstrated by experiment and simulation results. The simulation results showed that the dominant failure modes were the debonding between the platelets and the transverse failure in the platelets. The failure mechanism varied from one coupon to another due to the local morphological dissimilarities.
4. Compressive strength and modulus from compressive tests showed a decreasing trend with increasing effective off-axis angle, which was captured by the RVE and homogenized modeling prediction. Overall, the comparison of mechanical responses in the computational models and compressive tests show that the

proposed homogenized and RVE model can predict the mechanical properties of freeze-casted porous ceramic subjected to off-axis loading.

The developed multi-scale progressive failure modeling for the hierarchical materials can be used for predicting mechanical behavior and associated uncertainty in material response as a function of the material morphology and constituent mechanical properties. From an academic point of view, there is a lot of value in developing a multi-scale progressive failure model in order to predict the mechanical behavior and associated uncertainty. From an industrial point of view, there is a lot of value related to product development and technology development. The model will suggest the optimal material's morphology to maximize properties and performance.

11 FUTURE WORK

The constitutive damage modeling can simulate the fatigue and impact characterization of LDFC. Such a model can be useful in predicting the variability of the damage propagation in DCB samples. Future work can be focused on studying the mechanical properties and failure behavior in woven fabric polymer composites. Woven composite has a deterministic microstructure, but the pattern and orientation of the fibers play a vital role in the material's mechanical response. The notch sensitivity can be studied in the polymer composite with woven architecture. Such work is necessary to understand the size and location of the notch in woven composite on the material's failure behavior. Another essential subject to study can be constitutive modeling of the flow-oriented LDFC under tension, calibrated with current experimental results. The proposed subjects for future work are itemized in the following:

1. Develop the morphology of woven fabric polymer composites to analyze the effect of the reinforcement architecture on the mechanical behavior of the material.
2. Notch sensitivity analysis on the woven fabric polymer composites.
3. Study the impact and compression after impact (CAI) characterization in long discontinuous fiber polymer composite.
4. Develop a progressive failure modeling to analyze the impact and fatigue behavior of long discontinuous fiber reinforced polymer composites.
5. Develop a progressive failure modeling of flow-oriented long discontinuous fiber polymer composite to study the role of processing on the mechanical response of material.

REFERENCES

[1] M. Douglas, “A priestly hierarchy,” Apr. 2001, doi: 10.1093/acprof:oso/9780199245413.003.0003.

[2] S. G. Kravchenko, “Failure analysis in platelet molded composite systems,” PhD Thesis, Purdue University, 2017.

[3] S. G. Kravchenko *et al.*, “Tensile properties of a stochastic prepreg platelet molded composite,” *Compos. Part Appl. Sci. Manuf.*, vol. 124, p. 105507, Sep. 2019, doi: 10.1016/j.compositesa.2019.105507.

[4] S. Deville, “Ice-templating, freeze casting: Beyond materials processing,” *J. Mater. Res.*, vol. 28, no. 17, pp. 2202–2219, Sep. 2013, doi: 10.1557/jmr.2013.105.

[5] S. Deville, E. Saiz, R. K. Nalla, and A. P. Tomsia, “Freezing as a path to build complex composites,” *Science*, vol. 311, no. 5760, pp. 515–518, Jan. 2006, doi: 10.1126/science.1120937.

[6] S. Ko, J. Davey, S. Douglass, J. Yang, M. E. Tuttle, and M. Salviato, “Effect of the thickness on the fracturing behavior of discontinuous fiber composite structures,” *Compos. Part Appl. Sci. Manuf.*, vol. 125, p. 105520, Oct. 2019, doi: 10.1016/j.compositesa.2019.105520.

[7] S. Mortazavian and A. Fatemi, “Effects of fiber orientation and anisotropy on tensile strength and elastic modulus of short fiber reinforced polymer composites,” *Compos. Part B Eng.*, vol. 72, pp. 116–129, Apr. 2015, doi: 10.1016/j.compositesb.2014.11.041.

[8] J. Wulfsberg, A. Herrmann, G. Ziegmann, G. Lonsdorfer, N. Stöß, and M. Fette, “Combination of carbon fibre sheet moulding compound and prepreg compression moulding in aerospace industry,” *Procedia Eng.*, vol. 81, pp. 1601–1607, Jan. 2014, doi: 10.1016/j.proeng.2014.10.197.

[9] “Sheet molding compounds - Orgéas - - Major reference works - Wiley Online Library.” https://onlinelibrary.wiley.com/doi/abs/10.1002/9781118097298.weoc222.

[10] N. Heer *et al.*, “Versatility of long fiber AP nylon CR-6 organosheet to overcome intrinsic short comings of Long Fiber Thermoplastics,” 2020.

[11] J. Aubry, “HexMC — bridging the gap between prepreg and SMC,” *Reinf. Plast.*, vol. 45, no. 6, pp. 38–40, Jun. 2001, doi: 10.1016/S0034-3617(01)80207-1.

[12] S. G. Kravchenko, D. E. Sommer, B. R. Denos, W. B. Avery, and R. B. Pipes, “Structure-property relationship for a prepreg platelet molded composite with engineered meso-morphology,” *Compos. Struct.*, vol. 210, pp. 430–445, Feb. 2019, doi: 10.1016/j.compstruct.2018.11.058.

[13] S. G. Kravchenko *et al.*, “Tensile properties of a stochastic prepreg platelet molded composite,” *Compos. Part Appl. Sci. Manuf.*, vol. 124, p. 105507, Sep. 2019, doi: 10.1016/j.compositesa.2019.105507.

[14] P. Feraboli, E. Peitso, F. Deleo, T. Cleveland, and P. B. Stickler, “Characterization of prepreg-based discontinuous carbon fiber/epoxy systems,” *J. Reinf. Plast. Compos.*, vol. 28, no. 10, pp. 1191–1214, May 2009, doi: 10.1177/0731684408088883.

[15] I. Taketa, T. Okabe, H. Matsutani, and A. Kitano, “Flowability of unidirectionally arrayed chopped strands in compression molding,” *Compos. Part B Eng.*, vol. 42, no. 6, pp. 1764–1769, Sep. 2011, doi: 10.1016/j.compositesb.2011.01.021.

[16] B. R. Denos, S. G. Kravchenko, and R. B. Pipes, “Simulations of mechanical properties for discontinuous prepreg composites,” 2018.

[17] S. Sattar, B. Beltran Laredo, R. Larson, S. Kravchenko, and O. G. Kravchenko, “Effect of platelet length and stochastic morphology on flexural behavior of prepreg molded composite,” presented at the SPE ACCE 2021, Novi, MI.

[18] R. Lakes, “Materials with structural hierarchy,” *Nature*, vol. 361, no. 6412, Art. no. 6412, Feb. 1993, doi: 10.1038/361511a0.

[19] S. G. Kravchenko, D. E. Sommer, and R. B. Pipes, “Uniaxial strength of a composite array of overlaid and aligned prepreg platelets,” *Compos. Part Appl. Sci. Manuf.*, vol. 109, pp. 31–47, Jun. 2018, doi: 10.1016/j.compositesa.2018.02.032.

[20] S. G. Kravchenko, D. E. Sommer, B. R. Denos, W. B. Avery, and R. B. Pipes, “Structure-property relationship for a prepreg platelet molded composite with engineered meso-morphology,” *Compos. Struct.*, vol. 210, pp. 430–445, Feb. 2019, doi: 10.1016/j.compstruct.2018.11.058.

[21] T. H. Courtney, “Fundamental structure-property relationships in engineering materials,” Jan. 1997, doi: 10.31399/asm.hb.v20.a0002460.

[22] H.-C. Tseng, R.-Y. Chang, and C.-H. Hsu, “Improved fiber orientation predictions for injection molded fiber composites,” *Compos. Part Appl. Sci. Manuf.*, vol. 99, pp. 65–75, Aug. 2017, doi: 10.1016/j.compositesa.2017.04.004.

[23] S. G. Kravchenko, D. E. Sommer, and R. B. Pipes, “Uniaxial strength of a composite array of overlaid and aligned prepreg platelets,” *Compos. Part Appl. Sci. Manuf.*, vol. 109, pp. 31–47, Jun. 2018, doi: 10.1016/j.compositesa.2018.02.032.

[24] S. B. Visweswaraiah, M. Selezneva, L. Lessard, and P. Hubert, “Mechanical characterisation and modelling of randomly oriented strand architecture and their hybrids – A general review,” *J. Reinf. Plast. Compos.*, vol. 37, no. 8, pp. 548–580, Apr. 2018, doi: 10.1177/0731684418754360.

[25] S. Ko, J. Yang, M. E. Tuttle, and M. Salviato, “Fracturing behavior and size effect of discontinuous fiber composite structures with different platelet sizes,” *ArXiv181208312 Phys.*, Dec. 2018, Accessed: Mar. 31, 2022. [Online]. Available: http://arxiv.org/abs/1812.08312

[26] P. Feraboli, E. Peitso, F. Deleo, T. Cleveland, and P. B. Stickler, “Characterization of Prepreg-Based Discontinuous Carbon Fiber/Epoxy Systems,” *J. Reinf. Plast. Compos.*, vol. 28, no. 10, pp. 1191–1214, May 2009, doi: 10.1177/0731684408088883.

[27] N. Eguemann, L. Giger, M. Roux, C. Dransfeld, F. Thiebaud, and D. Perreux, “Compression moulding of complex parts for the aerospace with discontinuous novel and recycled thermoplastic composite materials,” in *19th International Conference on Composite Materials*, France, Jan. 2013, pp. 1–11. Accessed: Dec. 04, 2021. [Online]. Available: https://hal.archives-ouvertes.fr/hal-00983314

[28] C. Rose, C. Dávila, and F. Leone, *Analysis methods for progressive damage of composite structures*. 2013.

[29] M. Herráez *et al.*, “Computational micromechanics evaluation of the effect of fibre shape on the transverse strength of unidirectional composites: An approach to virtual materials design,” *Compos. Part Appl. Sci. Manuf.*, vol. 91, pp. 484–492, Dec. 2016, doi: 10.1016/j.compositesa.2016.02.026.

[30] M. Selezneva, “Experimental and Theoretical Investigations of Mechanical Properties of Randomly-Oriented Strand (ROS) Composites,” Ph.D., McGill University (Canada), Canada. Accessed: Dec. 04, 2021. [Online]. Available: https://www.proquest.com/docview/2516947427/abstract/CB5BA93940F04E77PQ/1

[31] P. Feraboli, T. Cleveland, P. Stickler, and J. Halpin, “Stochastic laminate analogy for simulating the variability in modulus of discontinuous composite materials,” *Compos. Part Appl. Sci. Manuf.*, vol. 41, no. 4, pp. 557–570, Apr. 2010, doi: 10.1016/j.compositesa.2010.01.003.

[32] “3D geometric modelling of discontinuous fibre composites using a force-directed algorithm - LT Harper, CC Qian, R Luchoo, NA Warrior, 2017.” https://journals.sagepub.com/doi/10.1177/0021998316672722 (accessed Apr. 03, 2022).

[33] S. Kravchenko, B. Denos, D. Sommer, A. Favaloro, W. Avery, and B. Pipes, *Analysis of open hole tensile strength in a prepreg platelet molded composite with stochastic morphology*. 2018. doi: 10.12783/asc33/26057.

[34] S. Deville, “Freeze-casting of porous ceramics: A review of current achievements and issues,” *Adv. Eng. Mater.*, vol. 10, no. 3, pp. 155–169, 2008, doi: 10.1002/adem.200700270.

[35] S. W. Sofie and F. Dogan, “Freeze casting of aqueous alumina slurries with glycerol,” *J. Am. Ceram. Soc.*, vol. 84, no. 7, pp. 1459–1464, Dec. 2004, doi: 10.1111/j.1151-2916.2001.tb00860.x.

[36] S. Deville, E. Saiz, and A. P. Tomsia, “Ice-templated porous alumina structures,” *Acta Mater.*, vol. 55, no. 6, pp. 1965–1974, Apr. 2007, doi: 10.1016/j.actamat.2006.11.003.

[37] S. Deville *et al.*, “Influence of particle size on ice nucleation and growth during the ice-templating process,” *J. Am. Ceram. Soc.*, vol. 93, no. 9, pp. 2507–2510, 2010, doi: 10.1111/j.1551-2916.2010.03840.x.

[38] D. Ghosh, N. Dhavale, M. Banda, and H. Kang, “A comparison of microstructure and uniaxial compressive response of ice-templated alumina scaffolds fabricated from two different particle sizes,” *Ceram. Int.*, vol. 42, no. 14, pp. 16138–16147, Nov. 2016, doi: 10.1016/j.ceramint.2016.07.131.

[39] J. S. Weaver, S. R. Kalidindi, and U. G. K. Wegst, “Structure-processing correlations and mechanical properties in freeze-cast Ti-6Al-4V with highly aligned porosity and a lightweight Ti-6Al-4V-PMMA composite with excellent energy absorption capability,” *Acta Mater.*, vol. 132, pp. 182–192, Jun. 2017, doi: 10.1016/j.actamat.2017.02.031.

[40] P. Šajgalik, J. Dusza, and M. J. Hoffmann, “Relationship between microstructure, toughening mechanisms, and fracture toughness of reinforced silicon nitride ceramics,” *J. Am. Ceram. Soc.*, vol. 78, no. 10, pp. 2619–2624, 1995, doi: 10.1111/j.1151-2916.1995.tb08031.x.

[41] E. W. Andrews, L. J. Gibson, and M. F. Ashby, “The creep of cellular solids,” *Acta Mater.*, vol. 47, no. 10, pp. 2853–2863, Aug. 1999, doi: 10.1016/S1359-6454(99)00150-0.

[42] L. J. Gibson, M. F. Ashby, J. Zhang, and T. C. Triantafillou, “Failure surfaces for cellular materials under multiaxial loads—I.Modelling,” *Int. J. Mech. Sci.*, vol. 31, no. 9, pp. 635–663, Jan. 1989, doi: 10.1016/S0020-7403(89)80001-3.

[43] J. Seuba, S. Deville, C. Guizard, and A. J. Stevenson, “Mechanical properties and failure behavior of unidirectional porous ceramics,” *Sci. Rep.*, vol. 6, p. 24326, Apr. 2016, doi: 10.1038/srep24326.

[44] L. J. Gibson and M. F. Ashbey, *Cellular solids: Structure and properties*, 2nd ed. Cambridge University Press, 1979.

[45] S. Deville, C. Viazzi, and C. Guizard, “Ice-structuring mechanism for zirconium acetate,” *Langmuir*, vol. 28, no. 42, pp. 14892–14898, Oct. 2012, doi: 10.1021/la302275d.

[46] J. Zhang and M. F. Ashby, “The out-of-plane properties of honeycombs,” *Int. J. Mech. Sci.*, vol. 34, no. 6, pp. 475–489, Jun. 1992, doi: 10.1016/0020-7403(92)90013-7.

[47] I. Nelson *et al.*, “Helical and bouligand porous scaffolds fabricated by dynamic low strength magnetic field freeze casting,” *JOM*, vol. 72, no. 4, pp. 1498–1508, Apr. 2020, doi: 10.1007/s11837-019-04002-9.
[48] H. L. Ferrand and F. Bouville, “Processing of dense bioinspired ceramics with deliberate microstructure,” *J. Am. Ceram. Soc.*, vol. 102, no. 12, pp. 7253–7263, 2019, doi: 10.1111/jace.16656.
[49] C. Minas, D. Carnelli, E. Tervoort, and A. R. Studart, “3D printing of emulsions and foams into hierarchical porous ceramics,” *Adv. Mater.*, vol. 28, no. 45, pp. 9993–9999, 2016, doi: 10.1002/adma.201603390.
[50] L. Zhang *et al.*, “Modeling the mechanical properties of optimally processed cordierite–mullite–alumina ceramic foams by X-ray computed tomography and finite element analysis,” *Acta Mater.*, vol. 60, no. 10, pp. 4235–4246, Jun. 2012, doi: 10.1016/j.actamat.2012.04.025.
[51] “The effect of wall thickness distribution on mechanical reliability and strength in unidirectional porous ceramics: Science and technology of advanced materials: Vol 17, No 1.” https://www.tandfonline.com/doi/full/10.1080/14686996.2016.1140309.
[52] K. L. Scotti *et al.*, “The effect of solidification direction with respect to gravity on ice-templated TiO2 microstructures,” *J. Eur. Ceram. Soc.*, vol. 39, no. 10, pp. 3180–3193, Aug. 2019, doi: 10.1016/j.jeurceramsoc.2019.04.007.
[53] “Multiphase imaging of freezing particle suspensions by confocal microscopy | Elsevier Enhanced Reader.” https://reader.elsevier.com/reader/sd/pii/S0955221918300669?token=39DF9CE1264BAA5BA788A4C5B77C8BCE0605AF5D316B9D30580CB433D72D364A7BB6778C0FA35DE3134C0C24EB1D432C (accessed Jun. 10, 2019).
[54] “Time-lapse, three-dimensional in situ imaging of ice crystal growth in a colloidal silica suspension | Elsevier Enhanced Reader.” https://reader.elsevier.com/reader/sd/pii/S1359645412008853?token=421438F7871443C681EBDB6C115253DCF3EB89EFCC2FD42EAFF32600B4EAFFE18B7D5F8C40915C2056A105A8A88267D3 (accessed Jun. 10, 2019).
[55] H. Ahmadian, M. Yang, A. Nagarajan, and S. Soghrati, “Effects of shape and misalignment of fibers on the failure response of carbon fiber reinforced polymers,” *Comput. Mech.*, vol. 63, no. 5, pp. 999–1017, May 2019, doi: 10.1007/s00466-018-1634-1.
[56] F. Bouville *et al.*, “Templated grain growth in macroporous materials,” *J. Am. Ceram. Soc.*, vol. 97, no. 6, pp. 1736–1742, 2014, doi: 10.1111/jace.12976.
[57] “Digimat user’s manual. Version 2017.” e-Xstream Engineering. MSC.
[58] S. G. Kravchenko and R. B. Pipes, “Progressive failure analysis in discontinuous Composite system of prepreg platelets with stochastic meso-morphology,” p. 14.
[59] “Constitutive modeling of engineering materials / PDF4PRO,” *PDF4PRO*, Sep. 12, 2018. https://pdf4pro.com/view/constitutive-modeling-of-engineering-materials-2e15e3.html.
[60] S. G. Advani and C. L. Tucker, “The use of tensors to describe and predict fiber orientation in short fiber composites,” *J. Rheol.*, vol. 31, no. 8, pp. 751–784, Nov. 1987, doi: 10.1122/1.549945.
[61] “Effect of matrix plasticity on ultimate strength of composite laminates - Zheng-Ming Huang, 2001.” https://journals.sagepub.com/doi/abs/10.1177/073168401772678760.

[62] Z.-M. Huang, “A bridging model prediction of the ultimate strength of composite laminates subjected to biaxial loads,” *Compos. Sci. Technol.*, vol. 64, no. 3, pp. 395–448, Mar. 2004, doi: 10.1016/S0266-3538(03)00220-3.
[63] Z. M. Huang, “Micromechanical strength formulae of unidirectional composites,” *Mater. Lett.*, vol. 40, no. 4, pp. 164–169, Aug. 1999, doi: 10.1016/S0167-577X(99)00069-5.
[64] “Progressive failure analysis of composites - T.E. Tay, G. Liu, V.B.C. Tan, X.S. Sun, D.C. Pham, 2008.” https://journals.sagepub.com/doi/10.1177/0021998308093912.
[65] “ABAQUS/CAE User’s Manual (v6.6).” https://classes.engineering.wustl.edu/2009/spring/mase5513/abaqus/docs/v6.6/books/usi/default.htm?startat=pt03ch12s08s03.html.
[66] Y. C. Zhang, T. Mabrouki, D. Nelias, and Y. D. Gong, “Chip formation in orthogonal cutting considering interface limiting shear stress and damage evolution based on fracture energy approach,” *Finite Elem. Anal. Des.*, vol. 47, no. 7, pp. 850–863, Jul. 2011, doi: 10.1016/j.finel.2011.02.016.
[67] “Hexcel | Composite Materials and Structures.” https://www.hexcel.com/ (accessed Aug. 15, 2022).
[68] “Abaqus Analysis User’s Guide (6.14).” http://130.149.89.49:2080/v6.14/books/usb/default.htm?startat=pt05ch23s06abm37.html (accessed Oct. 28, 2019).
[69] “Abaqus 2016 Documentation.” http://130.149.89.49:2080/v2016/index.html.
[70] P. Camanho and C. G. Davila, “Mixed-mode decohesion finite elements for the simulation of delamination in composite materials.” 2002.
[71] J. D. Whitcomb, *Analysis of instability-related growth of a through-width delamination*. National Aeronautics and Space Administration, Langley Research Center, 1984.
[72] T. N. Sti, T. T. Strength, T. K. Oõbrien, and R. Krueger, “Analysis of ninety degree flexure tests for characterization of composite U.S. Army Research Laboratory vehicle technology Directorate NASA Langley Research Center.” 2001.
[73] “Hexcel | Composite materials and structures.” https://www.hexcel.com/.
[74] “Measuring fibre orientation and predicting elastic properties of discontinuous long fibre thermoplastic composites - Réjean Belliveau, Éric Léger, Benoit Landry, Gabriel LaPlante, 2021.” https://journals.sagepub.com/doi/full/10.1177/0021998320949635.
[75] T. Ziegler, A. Neubrand, and R. Piat, “Multiscale homogenization models for the elastic behaviour of metal/ceramic composites with lamellar domains,” *Compos. Sci. Technol.*, vol. 70, no. 4, pp. 664–670, Apr. 2010, doi: 10.1016/j.compscitech.2009.12.022.
[76] E. Feilden *et al.*, “Micromechanical strength of individual Al2O3 platelets,” *Scr. Mater.*, vol. 131, pp. 55–58, Apr. 2017, doi: 10.1016/j.scriptamat.2017.01.008.
[77] E. J. Haney and G. Subhash, “Static and dynamic indentation response of basal and prism plane sapphire,” *J. Eur. Ceram. Soc.*, vol. 31, no. 9, pp. 1713–1721, Aug. 2011, doi: 10.1016/j.jeurceramsoc.2011.03.006.
[78] S. V. Chaudhari and M. A. Chakrabarti, “Modeling of concrete for nonlinear analysis Using Finite Element Code ABAQUS,” *Int. J. Comput. Appl.*, vol. 44, Apr. 2012.
[79] O. G. Kravchenko, G. Gedler, S. G. Kravchenko, D. L. Feke, and I. Manas-Zloczower, “Modeling compressive behavior of open-cell polymerized high internal phase emulsions: effects of density and morphology,” *Soft Matter*, vol. 14, no. 9, pp. 1637–1646, Feb. 2018, doi: 10.1039/C7SM02043K.

[80] S. Mojumdar, M. Sain, R. Prasad, L. Sun, and J. Venart, “Selected thermoanalytical methods and their applications from medicine to construction: Part I,” *J. Therm. Anal. Calorim.*, vol. 90, no. 3, pp. 653–662, Dec. 2007, doi: 10.1007/s10973-007-8518-5.

[81] X. Qiu, S. P. Tan, M. Dejam, and H. Adidharma, “Novel isochoric measurement of the onset of vapor–liquid phase transition using differential scanning calorimetry,” *Phys. Chem. Chem. Phys.*, vol. 20, no. 41, pp. 26241–26248, 2018, doi: 10.1039/C8CP05613G.

[82] L. Penel-Pierron, C. Depecker, R. Séguéla, and J.-M. Lefebvre, “Structural and mechanical behavior of nylon 6 films part I. Identification and stability of the crystalline phases,” *J. Polym. Sci. Part B Polym. Phys.*, vol. 39, no. 5, pp. 484–495, 2001, doi: https://doi.org/10.1002/1099-0488(20010301)39:5<484::AID-POLB1022>3.0.CO;2-R.

[83] L. Penel-Pierron *et al.*, “Structural and mechanical behavior of nylon-6 films. II. Uniaxial and biaxial drawing,” *J. Polym. Sci. Part B Polym. Phys.*, vol. 39, no. 11, pp. 1224–1236, 2001, doi: https://doi.org/10.1002/polb.1096.

[84] T. B. Nguyen Thi, M. Morioka, A. Yokoyama, S. Hamanaka, K. Yamashita, and C. Nonomura, “Measurement of fiber orientation distribution in injection-molded short-glass-fiber composites using X-ray computed tomography,” *J. Mater. Process. Technol.*, vol. 219, pp. 1–9, May 2015, doi: 10.1016/j.jmatprotec.2014.11.048.

[85] L. T. Harper, T. A. Turner, N. A. Warrior, and C. D. Rudd, “Characterisation of random carbon fibre composites from a directed fibre preforming process: The effect of tow filamentisation,” *Compos. Part Appl. Sci. Manuf.*, vol. 38, no. 3, pp. 755–770, Mar. 2007, doi: 10.1016/j.compositesa.2006.09.008.

[86] B. N. Sharma, D. Naragani, B. N. Nguyen, C. L. Tucker, and M. D. Sangid, “Uncertainty quantification of fiber orientation distribution measurements for long-fiber-reinforced thermoplastic composites,” *J. Compos. Mater.*, vol. 52, no. 13, pp. 1781–1797, Jun. 2018, doi: 10.1177/0021998317733533.

[87] *EllipseFit [Software]. https://www.frederickvollmer.com/ellipsefit/*.

[88] I. M. Daniel and O. Ishai, *Engineering mechanics of composite materials*, 2nd ed. New York: Oxford University Press, 2006.

[89] J. M. Whitney and R. J. Nuismer, “Stress fracture criteria for laminated composites containing stress concentrations,” *J. Compos. Mater.*, vol. 8, no. 3, pp. 253–265, Jul. 1974, doi: 10.1177/002199837400800303.

[90] “Uniaxial failure of composite laminates containing stress concentrations.” https://www.astm.org/stp34795s.html.

[91] L. A. Carlsson, D. F. Adams, and R. B. Pipes, *Experimental characterization of advanced composite materials, fourth edition*. CRC Press, 2014.

[92] H. J. Konish and J. M. Whitney, “Approximate stresses in an orthotropic plate containing a circular hole,” *J. Compos. Mater.*, vol. 9, no. 2, pp. 157–166, Apr. 1975, doi: 10.1177/002199837500900206.

[93] K. S. Ahmed, S. Vijayarangan, and A. C. B. Naidu, “Elastic properties, notched strength and fracture criterion in untreated woven jute–glass fabric reinforced polyester hybrid composites,” *Mater. Des.*, vol. 28, no. 8, pp. 2287–2294, Jan. 2007, doi: 10.1016/j.matdes.2006.08.002.

[94] W. A. Wooster, “Theory of elasticity of an anisotropic elastic body by S. G. Lekhnitskii,” *Acta Crystallogr.*, vol. 17, no. 6, Art. no. 6, Jun. 1964, doi: 10.1107/S0365110X64002171.

[95] R. B. Pipes, R. C. Wetherhold, and J. W. Gillespie, "Notched strength of composite materials," *J. Compos. Mater.*, vol. 13, no. 2, pp. 148–160, Apr. 1979, doi: 10.1177/002199837901300206.
[96] R. B. Pipes, J. W. Gillespie Jr., and R. C. Wetherhold, "Superposition of the notched strength of composite laminates," *Polym. Eng. Sci.*, vol. 19, no. 16, pp. 1151–1155, 1979, doi: 10.1002/pen.760191604.
[97] R. Byron Pipes, R. C. Wetherhold, and J. W. Gillespie, "Macroscopic fracture of fibrous composites," *Mater. Sci. Eng.*, vol. 45, no. 3, pp. 247–253, Oct. 1980, doi: 10.1016/0025-5416(80)90153-6.
[98] W. D. Pilkey, D. F. Pilkey, and Z. Bi, *Peterson's stress concentration factors*. John Wiley & Sons, 2020.
[99] J. W. Gillespie and L. A. Carlsson, "Influence of finite width on notched laminate strength predictions," *Compos. Sci. Technol.*, vol. 32, no. 1, pp. 15–30, Jan. 1988, doi: 10.1016/0266-3538(88)90027-9.
[100] R. S. Bay and C. L. Tucker, "Stereological measurement and error estimates for three-dimensional fiber orientation," *Polym. Eng. Sci.*, vol. 32, no. 4, pp. 240–253, 1992, doi: 10.1002/pen.760320404.
[101] R. K. Jujjavarapu, "Off axis compressive response of ice-templated ceramics," Old Dominion University, 2019.
[102] A. Lichtner, D. Roussel, D. Jauffrès, C. L. Martin, and R. K. Bordia, "Effect of macropore anisotropy on the mechanical response of hierarchically porous ceramics," *J. Am. Ceram. Soc.*, vol. 99, no. 3, pp. 979–987, Mar. 2016, doi: 10.1111/jace.14004.
[103] Y. Kong and J. N. Hay, "The measurement of the crystallinity of polymers by DSC," *Polymer*, vol. 43, no. 14, pp. 3873–3878, Jun. 2002, doi: 10.1016/S0032-3861(02)00235-5.
[104] C. Vicard, O. De Almeida, A. Cantarel, and G. Bernhart, "Experimental study of polymerization and crystallization kinetics of polyamide 6 obtained by anionic ring opening polymerization of ε-caprolactam," *Polymer*, vol. 132, pp. 88–97, Dec. 2017, doi: 10.1016/j.polymer.2017.10.039.
[105] L. Penel-Pierron, C. Depecker, R. Séguéla, and J.-M. Lefebvre, "Structural and mechanical behavior of nylon 6 films part I. Identification and stability of the crystalline phases," *J. Polym. Sci. Part B Polym. Phys.*, vol. 39, no. 5, pp. 484–495, 2001, doi: 10.1002/1099-0488(20010301)39:5<484::AID-POLB1022>3.0.CO;2-R.
[106] "Characteristics of plasticity in ductile metals." https://abaqus-docs.mit.edu/2017/English/SIMACAEGSARefMap/simagsa-c-matcharacteristics.htm.
[107] L. A. Carlsson, D. F. Adams, and R. B. Pipes, *Experimental characterization of advanced composite materials, fourth edition*. CRC Press, 2014.
[108] J. Gianchandani, J. E. Spruiell, and E. S. Clark, "Polymorphism and orientation development in melt spinning, drawing, and annealing of nylon-6 filaments," *J. Appl. Polym. Sci.*, vol. 27, no. 9, pp. 3527–3551, 1982, doi: 10.1002/app.1982.070270928.
[109] D. C. Montgomery, *Design and analysis of experiments*, Eighth edition. Hoboken, NJ: John Wiley & Sons, Inc, 2013.
[110] "Uniaxial compression analysis of glassy polymer networks using digital image correlation - ScienceDirect." https://www.sciencedirect.com/science/article/pii/S0142941810001248.
[111] I. M. Daniel and O. Ishai, *Engineering mechanics of composite material*, 2nd ed. New York: Oxford University Press, 2006.

APPENDICES

Appendix A Analytical Model for Strength Prediction

In the bridging micromechanical model, the ultimate strength of the composite was defined by the overall applied stress when one of the maximum normal stress of the constituent materials attained its ultimate value. The ultimate longitudinal, σ_{11}^{u}, and transverse tensile strength, σ_{22}^{u}, and in-plane shear strength, σ_{12}^{u}, were calculated by Equations A1, A2, and A3, respectively.

$$\boldsymbol{\sigma_{11}^{u} = \min\left\{\frac{\sigma_u^f - \left(\alpha_{e1}^f - \alpha_{p1}^f\right)\sigma_{11}^0}{\alpha_{p1}^f}, \frac{\sigma_u^m - \left(\alpha_{e1}^m - \alpha_{p1}^m\right)\sigma_{11}^0}{\alpha_{p1}^m}\right\}} \quad \text{(AI-1)}$$

$$\boldsymbol{\sigma_{11}^0 = \min\left\{\frac{\sigma_Y^m}{\alpha_{e1}^m}, \frac{\sigma_Y^f}{\alpha_{e1}^f}\right\}}$$

$$\boldsymbol{\sigma_{22}^{u} = \min\left\{\frac{\sigma_u^f - (\alpha_{e2}^f - \alpha_{p2}^f)\sigma_{22}^0}{\alpha_{p2}^f}, \frac{\sigma_u^m - (\alpha_{e2}^m - \alpha_{p2}^m)\sigma_{22}^0}{\alpha_{p2}^m}\right\}} \quad \text{(AI-2)}$$

$$\boldsymbol{\sigma_{22}^0 = \min\left\{\frac{\sigma_Y^m}{\alpha_{e2}^m}, \frac{\sigma_Y^f}{\alpha_{e2}^f}\right\}}$$

$$\boldsymbol{\sigma_{12}^{u} = \min\left\{\frac{\sigma_u^f - (\alpha_{e3}^f - \alpha_{p3}^f)\sigma_{12}^0}{\alpha_{p3}^f}, \frac{\sigma_u^m - (\alpha_{e3}^m - \alpha_{p3}^m)\sigma_{12}^0}{\alpha_{p2}^m}\right\}} \quad \text{(AI-3)}$$

$$\boldsymbol{\sigma_{12}^0 = \min\left\{\frac{\sigma_Y^m}{\sqrt{3}\alpha_{e3}^m}, \frac{\sigma_Y^f}{\alpha_{e3}^f}\right\}}$$

where σ_Y and σ_u denotes yield stress and ultimate tensile strength of the material (fiber or matrix), respectively. Suffix "m" and "f" refers to the matrix and fiber. In Equations A1, A2, and A3, α_{ei} and α_{pi} are calculated by Equations A4 – A15.

$$\alpha_{e1}^{f} = \frac{E^{f}}{V_f E^{f} + (1 - V_f) E^{m}} \quad \text{(AI-4)}$$

$$\alpha_{e1}^{m} = \frac{E^{m}}{V_f E^{f} + (1 - V_f) E^{m}} \quad \text{(AI-5)}$$

$$\alpha_{e2}^{f} = \frac{E^{f}}{V_f E^{f} + 0.5(1 - V_f)(E^{m} + E^{f})} \quad \text{(AI-6)}$$

$$\alpha_{e2}^{m} = \frac{0.5(E^{f} + E^{m})}{V_f E^{f} + 0.5(1 - V_f)(E^{m} + E^{f})} \quad \text{(AI-7)}$$

$$\alpha_{e3}^{f} = \frac{G^{f}}{V_f G^{f} + 0.5(1 - V_f)(G^{m} + G^{f})} \quad \text{(AI-8)}$$

$$\alpha_{e3}^{m} = \frac{0.5(G^{f} + G^{m})}{V_f G^{f} + 0.5(1 - V_f)(G^{f} + G^{m})} \quad \text{(AI-9)}$$

$$\alpha_{p1}^{f} = \frac{E^{f}}{V_f E^{f} + (1 - V_f) E_T^{m}} \quad \text{(AI-10)}$$

$$\alpha_{p1}^{m} = \frac{E^{m}}{V_f E^{f} + (1 - V_f) E_T^{m}} \quad \text{(AI-11)}$$

$$\alpha_{p2}^{f} = \frac{E^{f}}{V_f E^{f} + 0.5(1 - V_f)(E_T^{m} + E^{f})} \quad \text{(AI-12)}$$

$$\alpha_{p2}^{m} = \frac{0.5(E^{f} + E_T^{m})}{V_f E^{f} + 0.5(1 - V_f)(E_T^{m} + E^{f})} \quad \text{(AI-13)}$$

$$\alpha_{p3}^{f} = \frac{3G^{f}}{3V_f E^{f} + 0.5(1 - V_f)(E_T^{m} \pm 3G^{f})} \quad \text{(AI-14)}$$

$$\alpha_{p3}^{m} = \frac{0.5(3G^{f} + E_T^{m})}{3V_f G^{f} + 0.5(1 - V_f)(E_T^{m} + 3G^{f})} \quad \text{(AI-15)}$$

where, $E, G,$ and E_T are Young's modulus, shear modulus, and hardening modulus (slope of the uniaxial stress-strain curve in the plastic region) of the material, respectively. Equations A1, A2, and A3 were used to calculate the principal strength of the PA6/glass fiber bundles in organosheet.

The constitutive properties of E-glass fiber and PA6 used in the bridging model are shown in Table A1. The PA6 properties are measured through a uniaxial tensile test discussed in section 5-2. E^m, σ_Y^m, and σ_u^m was indicated in Table 3.

Table AI 1 Constituent properties

Property	**Value**
$\boldsymbol{E^f}$**(GPa)**	85
$\boldsymbol{G^f}$**(GPa)**	35
$\boldsymbol{G^m}$**(MPa)**	651
$\boldsymbol{\sigma_u^f}$**(GPa)**	3
$\boldsymbol{E_T^m}$**(MPa)**	100

Appendix B Material Constants of IM7/88552 Unidirectional Carbon-Epoxy Prepreg

Material property	Numerical value
Longitudinal modulus, $\boldsymbol{E_{11}(MPa)}$	165000
Transverse modulus, $\boldsymbol{E_{22}}$, $\boldsymbol{E_{33}(MPa)}$	8960
Shear modulus, $\boldsymbol{G_{12}}$, $\boldsymbol{G_{13}(MPa)}$	4690
Shear modulus, $\boldsymbol{G_{23}(MPa)}$	3400
Poisson's ratios,$\boldsymbol{\nu_{12}}$, $\boldsymbol{\nu_{13}}$	0.32
Poisson's ratios,$\boldsymbol{\nu_{23}}$	0.45
Longitudinal tensile strength,$\boldsymbol{F_{11}^{t}(MPa)}$	2705
Longitudinal compressive strength,$\boldsymbol{F_{11}^{c}(MPa)}$	1689
Transverse tensile strength,$\boldsymbol{F_{22}^{t}(MPa)}$	64
Transverse compressive strength,$\boldsymbol{F_{22}^{c}}$($\boldsymbol{(MPa)}$	288
Fracture energy, $\boldsymbol{G_1(kJ/m^2)}$	12
Fracture energy, $\boldsymbol{G_2}$ $\boldsymbol{(kJ/m^2)}$	1

VITA

Siavash Sattar was born in Esfahan, Iran. He received his bachelor's degree from Azad University, Iran, in 2012, and his master's degree from Tafresh University, Iran, in 2015. During his master's program, he worked on research projects, including computational modeling of the cold roll-forming manufacturing process, a three-dimensional moving boundary condition model of a paint cure oven used in the automobile industry, and design the power generation system for the residential area using the wind and solar hybrid method. In 2016, he joined the JondiShapour EPC Co., Iran, as the Quality Control and Quality Assurance Engineer and worked on the ABS and Rubber Plant construction project. In August 2018, he joined the Mechanical and Aerospace Engineering Department at Old Dominion University to pursue his Ph.D. in Mechanical Engineering. His doctoral research is on the analysis of the structure-property relationship for discontinuous fiber reinforced composites, with the focus on progressive damage modeling to provide the structural characteristics required in the automotive industry. He also worked on multiscale modeling of freeze-casted porous ceramics from micromechanical to homogenization to predict the effective mechanical properties. Siavash defended his doctoral thesis in Aug 2022.

Selected publications:

S. Sattar, B. Laredo, D. Pedrazzoli, M. Zhang, S. G. Kravchenko, O. G. Kravchenko “Mechanical behavior of long discontinuous glass fiber nylon composite produced by in-situ polymerization” Composites Part A: Applied Science and Manufacturing, Vol. 154, pp. 106779, March 2022.

S. Sattar, R. Mujadara, S. G. Kravchenko, O. G. Kravchenko “Micromechanical modeling of compressive behavior in freeze-casted ceramic” Journal of the American Ceramic Society, Vol.103, No.2, pp. 6543–6553, June 2020.